UNIVERSITY OF GENOA

Doctoral School in Science and Technologies of Chemistry and Materials

Curriculum: Chemical Science and Technologies

XXX CYCLE

Iron based magnetic nanoparticles: from synthesis to advanced applications

Silvia Villa

Tutor: Prof. Fabio Canepa

Ph.D. defense: 15th March 2018

List of abbreviations of chemical compounds

Alloc	allyloxycarbonyl
APTES	(3-aminoprpyl) triethoxysilane
BE	Benzylether
Boc	*tert*-butyloxycarbonyl
DCC	dicyclohexylcarbodiimide
DCM	dichloromethane
DIPEA	*N*,*N*-diisopropylethylamine
DMF	*N*,*N*-dimethylformamide
DMSO	dimethyl sulfoxide
EDTA	ethylenediaminetetraacetic acid
Et_3N	triethylamine
EtOH	ethanol
Fmoc	9-fluorenylmethoxycarbonyl
HATU	1-[Bis(dimethylamino)methylene]-1*H*-1,2,3-triazolo[4,5-*b*]pyridinium3-oxid hexafluorophosphate, *N*-[(Dimethylamino)-1*H*-1,2,3-triazolo-[4,5-*b*]pyridin-1-ylmethylene]-*N*-methylmethanaminium hexafluorophosphate *N*-oxide
HDD	1,2-hexadecanediol
HOBt	1-hydroxybenzotriazole
HOSu	N-hydroxysuccinimide
MB	methylene blue
MeOH	methanol
MPTMS	(3-mercaptopropyl) triethoxysilane
MTT	3-(4,5-Dimethylthiazolyl-2)-2,5-diphenyltetrazolium bromide
OA	oleic acid
OLA	oleylamine
PEG	polyethylene glycol
TFA	trifluoroacetic acid
THF	tetrahydrofuran
TRIS	tris(hydroxymethyl)aminomethane

Abstract

Nanoparticles have come and continue to be an extremely interesting research topic due to the variety of applications, deriving from the possibility to opportunely tailor their properties through different preparation methods. Among nanoparticles, magnetic nanostructures, due to their special characteristics, represent an interesting tool for advanced applications.

Focusing our research on the synthesis and characterization of magnetic nanoparticles, we developed materials for potential advanced applications. In the framework of my PhD research, I devoted myself on two main potential applications: in the biomedical field for magnetic drug delivery and in the environmental field for heavy metals capture and organic pollutant degradation.
The research has been always performed on magnetic nanosized structures, dealing with iron-based particles since they allow to obtain, in an easy and reliable way, a product with specific and well-defined properties.

The PhD research activity was mainly focused on the synthesis and characterization of magnetic nanoparticles, opportunely functionalized and engineered to be applied in biomedical and environmental fields.
The difference of the two applications required opportunely tailored materials, and thus proper synthetic methods have been adopted.
The work will be divided into two main parts separated for the specific application where synthetic protocols, characterizations and results are reported and extensively discussed.
In both applications, ferrite nanoparticles were opportunely synthesized and functionalized. Within the biomedical field, the main effort was done to synthetize the optimal nanoparticles based material to be conjugated with a fluorescent tripeptide and to evaluate the drug release activated through an enzyme recognition and cleavage process.
Instead within environmental field, opportune functionalized nanoparticles were employed in toxic metals capture and recovery from waters, performing static and dynamic procedures.
Experiments among photocatalysis were also performed; magnetite or ferrite nanoparticles were used as nucleation seeds in the synthesis of TiO_2 nanoparticles achieving excellent efficiency in degradation of Methylene Blue.

Index

Introduction

The current agreement in the research world is that the range 1 – 100 nm defines the size range of a nanoparticle. Since particles are three dimensional structures, these objects present at least one dimension between 1 – 100 nm, the same dimensional range of big organic molecules or viruses.[1]
Even if the given definition is quite clear, it does not really help to identify nanoparticles (NPs).
The term "nanoparticle" is a subject of controversy regarding the size range and the presence of a size-related property. Current usage emphasizes size and not properties in the definition; indeed, the length scale may be a hydrodynamic diameter or a geometric length appropriate to the intended use of the nanoparticle.
Talking about NPs, we can find multiple structures in term of composition, organization and shape. A significant example can be the comparison between spherical nanoparticles (3D), nanoplatelets (2D) and nanowires (1D); all of them fall inside the given definition even if the strongly different shape brings to strongly different application and synthesis procedures.
Since decreasing the size of a particle results in a larger share of the atoms on the surface, and thus enhances the influence of surface effects and changes the material properties, the past several decades have witnessed a booming research into studying different kinds of NPs and the interface between materials.

Among inorganic NPs, magnetic nanoparticles (MNPs) have gained great interest due to their capability to be functionalized in different ways and for multiple purposes.[2,3] Among them, magnetic single-domain NPs are distinguished because of their broad application fields.[4]
These nanometer-sized particles exhibit intrinsic and unique properties, such as high saturation magnetization, enhanced biocompatibility (for iron based materials), and less toxicity that involve them in the chemical, environmental and medical sectors. For example, superparamagnetic NPs have shown promising performance in pollutant removal or toxicity mitigation and some breakthroughs have been conducted in various fields, such as industrial, environmental, analytical, and biomedical[5].
In addition, in these fields, the control of the particle size is very important because the size strongly dominates the chemical and physical properties of the nanocrystals. For instance, when the particles are used in pharmaceutical and biomedical purposes, the magnetic particles should possess very small size, narrow size distribution and high magnetization values.
In particular, superparamagnetic NPs have attracted attention for biomedical applications because of their easy manipulation, biological compatibility, physicochemical properties, and extremely tunable magnetic properties. The properties of NPs depend on the synthesis methods, interaction among particles, particle size distribution, and particle size and shape; thus, a certain biomedical application requires a suitable synthesis method to attain specific performance.[6]

In the first part of the thesis, I report our research on nanoparticles for ***biomedical applications***. Magnetite NPs with superparamagnetic properties (high response to an external magnetic field and absence of remanence after its removal) have been synthesized. These particles represent an ideal candidate for magnetic drug delivery since they can be easily controlled by an external magnetic field and they present low toxicity for *in vivo* applications. In this framework, coprecipitation and high temperature decomposition processes were the most investigated.

Their high surface/volume ratio allow tunable functionalizations to attach molecules and, hence, nanoparticles become suitable nanocarriers.
The main research activity within biomedical applications has been the preparation of a magnetic nanocarrier able to conjugate and release drugs, assessing the enzyme promoted cleavage efficiency. For this purpose, amino-silane (APTES) modified magnetite NPs were synthesized through a hydrolysis and condensation process, and were conjugated to an organic system constituted by a fluorescent molecule, a tripeptide specifier and a spacer. The system can release the fluorescent molecule upon a selective enzymatic hydrolysis promoted by a lysine specific protease.
The tripeptide (D-Val-L-Leu-L-Lys) was thought to be recognized by plasmin; plasmin, a serine protease, is formed upon cleavage of plasminogen by urokinase-type plasminogen activator (u-PA), a protein associated with tumor invasion and metastasis.
In order to facilitate analysis of enzymatic cleavage and obtain the first proof of concept of an enzymatic release of a small organic molecule bound to a magnetic nanoparticle, we decided not to bind a real drug, but simply a fluorescent molecule, pyrenemethylamine.
The linker between APTES functionalized nanoparticles and pyrenylmethylamine can be schematically divided into two parts: a specifier peptide, which will act as the recognizing element for plasmin, and which will be bound to pyrenemethylamine, and a spacer between the specifier peptide and the nanoparticle.
The choice of the spacer was not trivial, since both the specifier peptide and the APTES functionalized nanoparticle ends with an amino group. We selected and used two possible ways to join these two amines: a) the transformation into a urea; b) the coupling with a dicarboxylic acid.
All the magnetite-based products have been extensively studied by means of different experimental techniques such as electron microscopy and fluorescence analyses while the organic compounds have been characterized through Nuclear Magnetic Resonance and Fourier Transform Infrared Spectroscopy.

Another research activity among nanocarriers was based on micelles and Solid Lipid Nanoparticles embedded with iron oxide NPs and Sorafenib (a drug for liver cancer). The samples and the *in vitro* experiments were performed by Dr. Nunzio Denora and Dr. Nicoletta Depalo, working at University of Bari and CNR of Bari. My contribution was mainly focused on the magnetic characterization of the two materials and the simulation of magnetic accumulation in flow through a dynamic glass capillary circuit, to simulate the potential accumulation in body blood flow.

Part of my work, focused on potential biomedical application of ferrite NPs, was carried out during the research period I spent at the Norwegian University of Science and Technology, NTNU (Trondheim, Norway), in the framework of a collaboration with Prof. D. Peddis and Dr. G. Singh.
We devoted our attention on the development of core-shell and multi-shell hard/soft ferrite NPs for preliminary hyperthermia studies.

In the second part of the thesis, my research on nanoparticles for ***environmental applications*** is reported. Opportunely functionalized magnetite NPs were investigated as adsorbent in the removal of toxic metal ions from artificially polluted waters. Furthermore, the recovery of metals adsorbed onto the NPs was evaluated, through complexation with etylenediaminetetraacetic acid (EDTA), in more than one cycle of capture/recovery.

Due to its high affinity to metal ions, thiol groups were chosen to be the interacting group between NPs surface and metals. Hence, thiol-silane functionalized magnetite NPs were employed in the capture and recovery of Pb (II), Cu (II), Cd (II) and Ag (I) from waters.
Different approaches were studied: a static mode, using a test tube as reactor, and a dynamic mode, using an appositely designed circuit. The static mode allowed to optimize the experimental conditions (concentrations of NPs and metal ions, time of capture, time and dynamics for recovery, etc.); the upgrade of the system was evaluated using a dynamic approach in which a glass capillary circuit was opportunely designed to treat up to 1 L of polluted water.

In the framework of environmental applications, another research topic dealt with the degradation of organic pollutants through photocatalysts based on magnetic NPs and titania.
In collaboration with group of Prof. Ferretti, we have studied the synthesis of titanium dioxide nanoparticles in the presence of magnetic nanoparticles acting as nucleation seeds. Different chemical composition, size and shape of magnetic ferrite nanoparticles as magnetite, cobalt ferrite, nickel ferrite and non-magnetic NPs as Lu_2O_3 nanoparticles, have been investigated. The photocatalytic performance has been evaluated in the framework of a standard ISO 10678:2010 protocol, *i.e.*, the degradation of a methylene blue (MB) solution of known concentration. The best material was also tested for the degradation of Ofloxacin (OFL), an important emerging water pollutant, belonging to the class of fluoroquinolone (FQ) antibiotics.

1 Applications of NPs

Interest in magnetic nanoparticles has grown recently and their applications have attracted the attention of both the research and industrial communities in the chemical, environmental and medical sectors.[7]

In this field, magnetic NPs gained particular influence extending their applications to magnetic separation, drug delivery, hyperthermia treatment and contrast agents for magnetic resonance imaging (MRI). The appealing of magnetic nanoparticles in biomedical applications is related to the unusual magnetic properties observed at the nanoscale (described in the next chapter).

The main activities carried out during my PhD research were carried out within the drug delivery and pollutant removal areas; thus, in this chapter, I will focus on these two main categories of applications.

1.1 Biomedical applications

Magnetic nanoparticles offer some attractive possibilities in biomedicine. Since NPs have controllable sizes ranging from a few nanometres up to hundreds of nanometres, which places them at dimensions comparable to those of a cell (10–100 µm), a virus (20–450 nm), a protein (5–50 nm) or a gene (2 nm wide and 10–100 nm long), they can 'get close' to a biological entity of interest.[8] Biomedical applications with MNPs are generally classified into *in vitro* (outside the body) and *in vivo* (inside the body). *In vitro* applications are mainly used in diagnostic processes, such as cell separation/selection, magnetic relaxometry, and magnetic resonance imaging (MRI). *In vivo* applications may include diagnostic processes, such as nuclear magnetic resonance imaging, as well as therapeutic applications such as drug delivery and magnetic hyperthermia.[9]

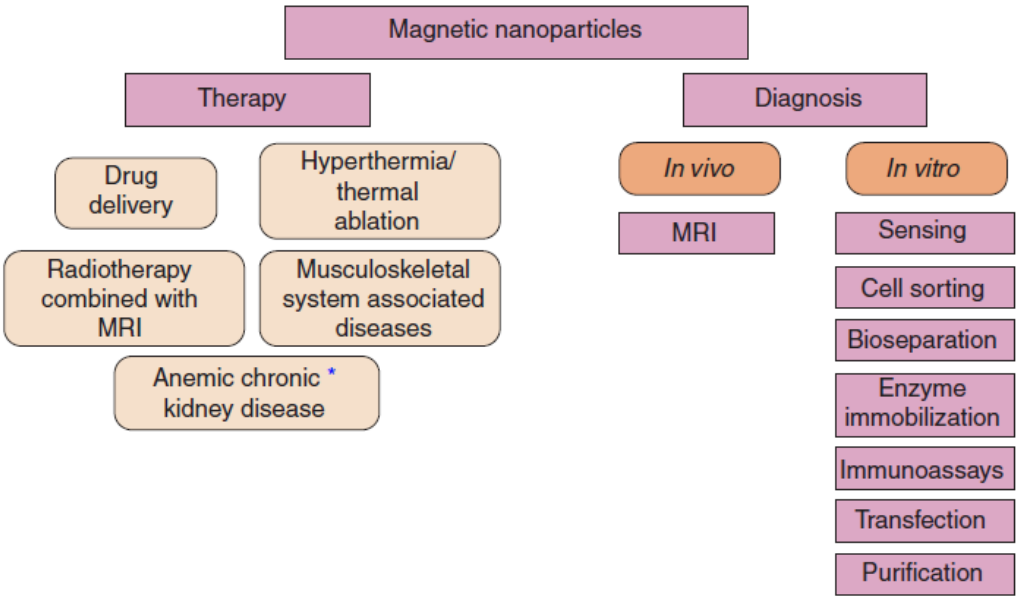

Figure 1. *In vitro* and *in vivo* biomedical applications of magnetic nanoparticles.[10]

Although many materials have been synthesized and extensively characterized, for the *in vivo* applications of the particles, there is still a big lack of knowledge due to two big problems. The first

problem occurs upon exposing the NPs to a physiological environment, which leads to serious agglomeration due to the interaction of the large surface area of NPs with plasma proteins. It has been demonstrated that proteins rapidly form a protective protein corona on the surface of the NPs which can significantly modify protein activity and structure and interfere with their natural fate. The absorption of protein can be tuned up modifying the surface of the starting NPs, *i.e.* functionalizing, for example, the surface with albumin or poly-ethylene glycol (PEG). This treatment is fundamental since it allows to vary the *interaction* NPs – body from innocuous elimination through the urine in minutes to strong and aggressive immune response.
The second problem is strictly connected with the first one. It is related to the nature of nanoparticles that can determine their fate into the biological medium. Interaction is mainly driven by the characteristics of NPs that define the surface properties: the material chemical composition, surface functionalization, shape, porosity and surface crystallinity, roughness, and hydrophobicity or hydrophilicity. Other quantifiable properties, such as effective surface charge (zeta potential), particles aggregation, stability/biodegradability, dissolution characteristics, hydration and valence of the surface layer, are determined by the characteristics of the suspending media, including the ionic strength, pH, temperature and the presence of large organic molecules. The internalization of particles in the cell through the biological membrane barrier as well as the mechanism of exit through the cell still represent two examples of questions without a clear answer.

1.1.1 Drug delivery

The major disadvantage of most of the chemotherapeutic approaches to cancer treatment is that they are non-specific. Therapeutic (generally cytotoxic) drugs are administered intravenously leading to general systemic distribution. The non-specific nature of this technique results in the well-known side-effects of chemotherapy as the cytotoxic drug attacks normal, healthy cells in addition to its primary target, tumor cells. The choice of magnetic nanoparticle-based targeting (Magnetic Drug Delivery, MDD) lies in the potential to reduce or eliminate the side effects of chemotherapy drugs by reducing their systemic distribution as well as the possibility of administering lower but more accurately targeted doses of the cytotoxic compounds. The idea of using magnetic nanoparticles to act as therapeutic drug carriers to target specific sites in the body dates to the late 1970s.[11,12] Widder and others developed magnetic nanoparticles to which cytotoxic drugs could be attached. The drug/carrier complex is then injected into the subject either via intravenous or intra-arterial injection. High-gradient external magnetic fields generated by rare earth permanent magnets or electromagnets with a specific 3D architecture are used to guide and concentrate the drugs to the tumor locations. Once the magnetic carrier is concentrated at the tumor or other target *in vivo*, the therapeutic agent is then released from the magnetic carrier, either via enzymatic activity or through changes in physiological conditions such as pH, osmolality, or temperature, leading to increased uptake of the drug by the tumor cells at the target sites.[13–15]

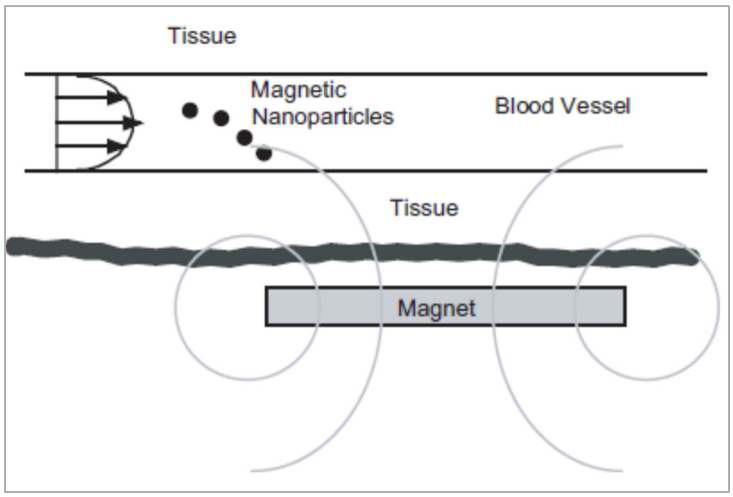

Figure 2. Scheme of magnetic drug delivery.[16]

Superparamagnetic Iron Oxide Nanoparticles (SPIONs) are a unique type of magnetic nanoparticles that have received most of the research focus because of their many desirable features, such as biocompatibility, biodegradability and ease of synthesis[17]. In addition, their superparamagnetic nature makes them the most suitable type of MNPs for biomedical application. Furthermore, no hysteresis is produced so that they do not leave any residual magnetization after the external magnetic field is removed.

This property assists in avoiding coagulation, which consequently lowers the possibility of agglomeration *in vivo* compared with other MNPs.[18]

Magnetic drug delivery seems particularly appealing since it allows to access regions not easily reachable with classical surgery; furthermore, the treatment would be much less invasive, requiring much lower doses for the drugs since it would be completely collected in the right place.

The functionalization of nanosized structure for MDD strongly affects also the uptake of the NPs inside the cells whereas the mechanism is not completely disclosed. Therefore, the NPs are usually coated with polymers such as dextran, dendrimers, polyethylene glycol (PEG) or polyethylene oxide or inorganic materials such as silica.

Enzymes that are naturally expressed in tumors can be also used for inducing the release of anticancer agents from a drug carrier. This strategy is based on drug delivery systems that are susceptible to a specific enzyme overexpressed by the tumor (*e.g.* plasmin). Under the influence of the enzyme, the drug is released in the target site.[19]

Hence, careful nanostructure construction (tailored drug release characteristics, low immunogenicity, specific recognition site etc.) brings to improved treatment efficacy and reduction of unwanted side effects. Delivery carriers have often been combined with imaging facilities into unique NPs through cleaver formulations of nanoscaled materials, enabling simultaneous *in vivo* diagnostic imaging and drug delivery for real time treatment tracking.

1.1.2 Magnetic Hyperthermia

Another important biomedical application of magnetic NPs is the magnetic hyperthermia (MH). The term “hyperthermia” is derived from two Greek words, “hyper” and “thermos” meaning “rise” and “heat,” respectively, because this treatment consists of increasing the temperature in a very well-

defined area just above the physiological temperature (up to ~40 °C) to induce a cytotoxic effect in tumor cells.[20] Cancer cells are considered vulnerable to "relatively" high temperatures ranging from 41 °C to 46 °C.

Taking into account the extent of the treated region, hyperthermia can be classified into three types: (a) whole body hyperthermia, (b) partial hyperthermia (applied to treat locally advanced cancer by perfusion or microwaves), and (c) local hyperthermia (mainly for smaller volumes than organs). Until now, hyperthermia treatments are used locally, to overcome adverse side effects and increase the efficiency, and mainly used as coadjutant treatment to chemotherapy. The temperature increase in local hyperthermia might be accomplished by distinct approaches based on the use of ultrasound, microwaves, or near-infrared radiation.[21] Even though these modalities have been commonly used during clinical treatment of different cancer types, showing poor spatial and temporal control, nowadays MH has some fundamental advantages. Firstly, the applied alternating magnetic field penetrates deeper than any other activation mechanism, allowing to reach internal tissues or organs; MNPs can be injected in a high concentration range and may stay at the tumor site for repeated treatments; tuning the size, morphology and surface functionalization of the MNPs results in enhancing biocompatibility, minimizing blood proteins adsorption and in different heating capabilities.

In magnetic hyperthermia, the heat increase is created by the presence of superparamagnetic NPs exposed to an oscillating magnetic field. For these particles, the response to the AC field can be described in term of their complex susceptibility and the generation of heat can be considered as a conversion of magnetic energy into internal energy that occurs when the NPs magnetization lags the applied field.[22] It is noteworthy to underline that the heating ability (generally referred as specific loss power, SLP) is strongly related to the characteristics of the particles in terms of material, size distribution, shape and crystallinity, thus an accurate characterization of the magnetic, physical and dimensional properties is required.

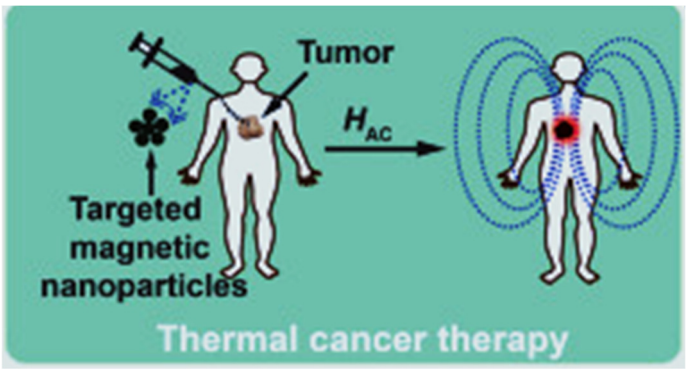

Figure 3. Scheme of magnetic hyperthermia in the cancer treatement. After the injection of the NPs, and their targeting to the tumor site, an alternating magnetic field (H_{AC}) is applied to generate the heating loss in the NPs.[23]

Magnetic hyperthermia, that ensures better performances and successful applications with limited damage for the surrounding tissue, have been reached already in 1957.[24] The potential medical market of the technique has been already achieved in an approved medical device (*Nanoactivator*) commercialized by MagForce («MagForce Company», n.d.) where magnetic NPs are used for the thermal treatment of glioblastoma multiforme. Even if the localized heating of tumor cell is obtained by hyperthermia, the commercialized device does not require the collection of the particles close to the cancer, but it involves the injection of the NPs directly in the treated zone. After the injection, the

particles (15 nm aminosilane-coated SPIONs) start to agglomerate thus fixing their position for multiple magnetic exposure.[25,26]

1.2 Environmental applications

1.2.1 Toxic metals capture

In recent years, nanosized magnetic systems attracted great attention due to their use for a possible new resolution of different environmental problems[27]; indeed, MNPs have shown promising performance in pollutant removal from water or toxicity mitigation.[28,29] Similarly, their effective application in membrane separation water treatment and purification processes has been demonstrated.[30,31]

Water pollution by heavy metals and dyes has become a serious problem because of their adverse effects on ecological systems and human health.[32] Heavy metals like copper, chromium, cadmium, lead, zinc, mercury, nickel or arsenic, are released into the environment as consequence of different natural or human induced activities such as mining, metal finishing, painting and printing processes, pesticides and fertilizers manufacture and use, etc.[33–35] Their presence is a major concern since they are highly toxic, carcinogenic and mutagenic even at low concentrations.[36] On the other side, organic dyes can be highly toxic for the aquatic life. Many different pollutant agents can be found since more than 100 thousand of different dyes are used in textile, pharmaceutical and cosmetic industries. To reduce the amount of such pollutant, various technologies have been developed for the removal of heavy metals and dyes from industrial wastewater, such as coagulation/precipitation,[37] ion exchange,[38] solvent extraction,[39] electrodeposition,[40] membrane filtration,[41] electrodialysis,[42] etc. Even if these approaches allow to decrease the pollutants concentration, many drawbacks have to be considered as cost, reduced or poor efficiency and complexity of the removal systems. In this field, MNPs have been studied as nanoadsorbent materials for heavy metals and dyes removal and their superior characteristics in comparison with traditional adsorbents (i.e. large surface area, high number of active surface sites, low intraparticle diffusion rate and high adsorption capacities), make their use very promising for the treatment of polluted waters, reducing costs and removing a larger amount of pollutants.[43] Moreover, the recent improvements in the synthesis methods allow the easy anchorage of different functional groups on the surface of the nanoadsorbents: these groups take part in the adsorption process as specific binding sites, increasing the adsorption capacity and improving the selectivity of the process for each specific pollution problem. Furthermore, their recovery can be easily performed with magnetic separators.

Many different kinds of magnetic NPs have been tested for the separation of heavy metals and dyes. Nanoparticles of Iron (0) have been successfully adopted for chromium and arsenic where the adsorption process is guaranteed by the oxidation of the particles surface in presence of air or water.[44] Iron oxide NPs have been tested as well; according to Chowdhury et al.[45] the surface of these particles is covered by hydroxyl groups and their chemistry regulate the adsorption properties. In particular, anionic metallic pollutants such as arsenate and chromate oxyanions can be adsorbed at low pH through electrostatic interactions.[34,46] On the contrary, at high pH values these materials are effective

in the capture of metal cations as Cu^{2+}, Ni^{2+}, Zn^{2+}, Pb^{2+} or Cd^{2+}.[47,48] Furthermore, maghemite and magnetite have been reported as novel adsorbent for dyes separation thank to electrostatic interactions. Even if bare nanoparticles have been proved to be effective in the adsorption process, many advantages can be achieved adopting a proper functionalization by surface coating with organic moieties. Amine functionalized silica coated NPs and amine functionalized NPs can be easily obtained by means of sol-gel reaction of (3-aminopropyl) triethoxysilane (APTES) and have demonstrated outstanding performances for the adsorption of many heavy metals.[49,50] In these functionalized compounds the amino group increases the electrostatic interaction as well as it acts as chelating agent for metal: thus higher concentration of reactive group generally correspond to better performances even if a linear dependence is not always observed.[51] Amino functionalized NPs showed good performances also for dyes removal, where the performances are pH dependent with adsorption effects mainly related to electrostatic interactions. Thiol functionalized silica NPs and thiol functionalized NPs can be synthesized considering (3-Mercaptopropyl) trimethoxysilane (MPTMS) in the functionalization reaction. Thiols functionalized NPs have been successfully employed for Hg^{2+} and Pb^{2+} removal[52] even in natural water.[53]

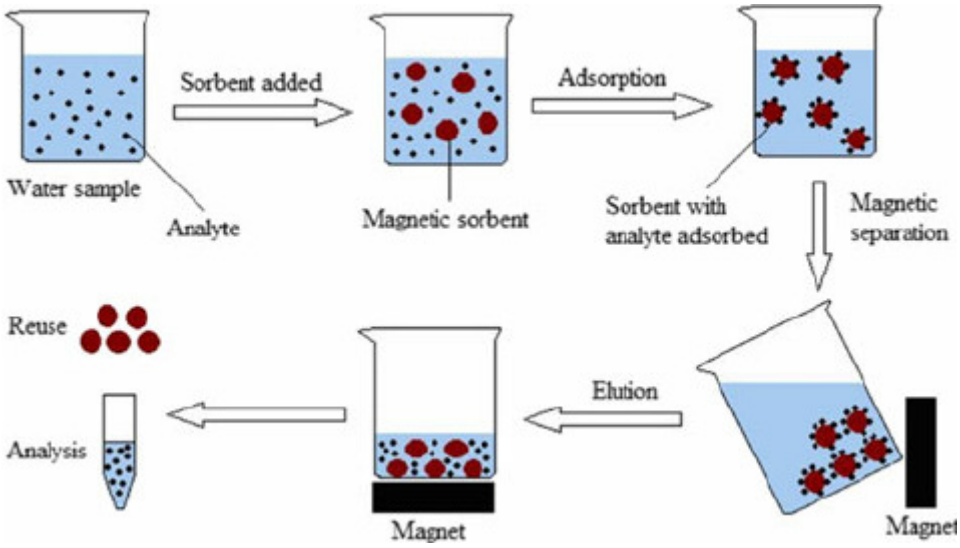

Figure 4. Scheme of magnetic extraction of an analyte from water.[54]

As mentioned before, one of the main advantages of the use of magnetic NPs is the possibility to collect the particles by means of an external magnetic field. On one side, magnetic separation is more efficient, selective and faster than centrifugation or filtration processes.[55] Furthermore, it is less affected by the condition of the aqueous environment such as temperature, pH and ionic concentration.[56] On the other side, the collection can be achieved using permanent magnets thus without consumption of additional energy. Despite the many advantages, several problems must be taken into account before an extensive use of nanosized particles for adsorption of pollutants. First, the collection is necessarily related to a certain degree of agglomeration of the particles, which cannot be easily brought back to the original state. This decrease in the available surface area brings a decrease in the adsorption performances thus a shortening of the life of the adsorbent material. Another challenging problem is related to the regeneration of the particles. Even if the adsorption process can be relatively straightforward, desorption and adsorbent regeneration is a critical step, which contributes to the process costs and pollutant recovery. A successful regeneration process should restore the initial characteristics of the adsorbent, allowing the complete reuse of the MNPs

during the maximum number of cycles and thus decreasing the costs of the overall separation process. However, in a large number of sorption studies, available in the literature, dealing with the use of nanoparticles for the removal of heavy metals and dyes, desorption and reuse of the adsorbents has not been accurately analyzed. Particularly, the desorption of heavy metals and dyes from loaded adsorbents has been carried out with different solutions, being most of them selected according to the influence of the pH value on the adsorption process.[57]

The regeneration of magnetic nanoadsorbents loaded with cationic or anionic metallic pollutants has been performed with aqueous solutions of acids or bases, respectively. In the case of dye removal, acid or basic solutions in alcohols such as ethanol or methanol have been reported as effective regeneration solutions.[58] Although most of the regenerated materials keep their adsorption capacity, the concentration of the regeneration agent and the contact time during the desorption process should be controlled to avoid modifications of the morphological and chemical structure of the MNPs.

1.2.2 Photocatalysis

Photocatalysis is the main technology breakthrough for water treatment and purification, becoming a helpful tool for existing techniques in the removal of trace contaminants. For example, for the disinfection of swimming pools, these systems are already commercially available. A photocatalyst is defined as a material that is capable of absorbing light, producing electron–hole pairs that enable chemical transformations of the reaction participants and regenerate its electronic structure after each cycle of such interactions. The electron-hole pair production process gives rise to the formation of radicals, at the surface of the photocatalyst, able to remove, by destruction, organic pollutants molecules.

The use of nanostructures based on metal oxide semiconductors such as zinc oxide (ZnO), titanium oxide (titania TiO_2), tungsten oxide (WO_3) and zinc stannate (Zn_2SnO_2) can be an attractive method of water purification as it can remove chemical species as well as biological contaminants.[59]

A good photocatalyst should efficiently absorb light preferably in the visible or near UV part of the electromagnetic spectrum. The underlying mechanism of heterogeneous photocatalysis is focused on a wide band gap semiconductor photocatalyst (see Table 1), which, upon irradiation with light with energy higher than the band gap energy of the material, creates electron–hole pairs.

Compound	ΔE (eV)
ZnO	3.3
TiO_2	3.2
WO_3	2.8
Zn_2SnO_2	3.6
Fe_2O_3	3.1
SiC	3.0
Si	1.1

Table 1. Bad gap values of some photocatalysts.[60]

The photogenerated electron moves up to the conduction band leaving a hole in the valence band. Majority of these photogenerated charge carriers undergo wasteful recombination, while escape recombination, and initiate redox reactions in molecules adsorbed at the surface of the photocatalyst and thereby degrading them. The photogenerated electrons and holes have been found to degrade almost all types of organic, inorganic and microbial contaminants, owing to their high redox potentials.

However, in order to inhibit recombination of electron hole pairs upon light exposure, sufficient electron vacant states need to be present. As a lot of work has done on photocatalysis in the agriculture and microbiology fields, it is important that the photocatalysts should be biologically inert and non-toxic. Nanostructured photocatalysts offer large surface to volume ratio, allowing higher adsorption of the target molecules. Intensive research over the past decade for its implementation in the purification of drinking water can be found in the literature.[61,62] Efficacy of photocatalysis in the detoxification of a wide range of industrial and agricultural effluents is also well documented.[63] Another interesting aspect of photocatalysis is the potential utilization of sunlight, which could allow energy-efficient treatment in remote locations.

Heterogeneous photocatalysis by semiconductors such as titanium dioxide (TiO_2) is a promising technology for water purification.[64] It can degrade water pollutants such as benzene, various dyes, and complex mixtures of water contaminants in industrial and domestic wastewaters.[65] In addition, it is able to degrade many chemical contaminants and microorganisms completely into carbon dioxide, water, and mineral acid.[66]

When the electron in the valence band of the semiconductor, under UV light, absorbs a photon with energy greater than the band gap (**ΔE**) of the semiconductor, the electron becomes excited and jumps to the conduction band, leaving a positively charged hole in the valence band. Besides recombination with the electron, the positively charged hole can oxidize water molecules to form hyper-reactive hydroxyl free radicals (•OH). The resulting hydroxyl radicals are the main agent that attack the chemical pollutant molecules or microorganism cells to purify water.

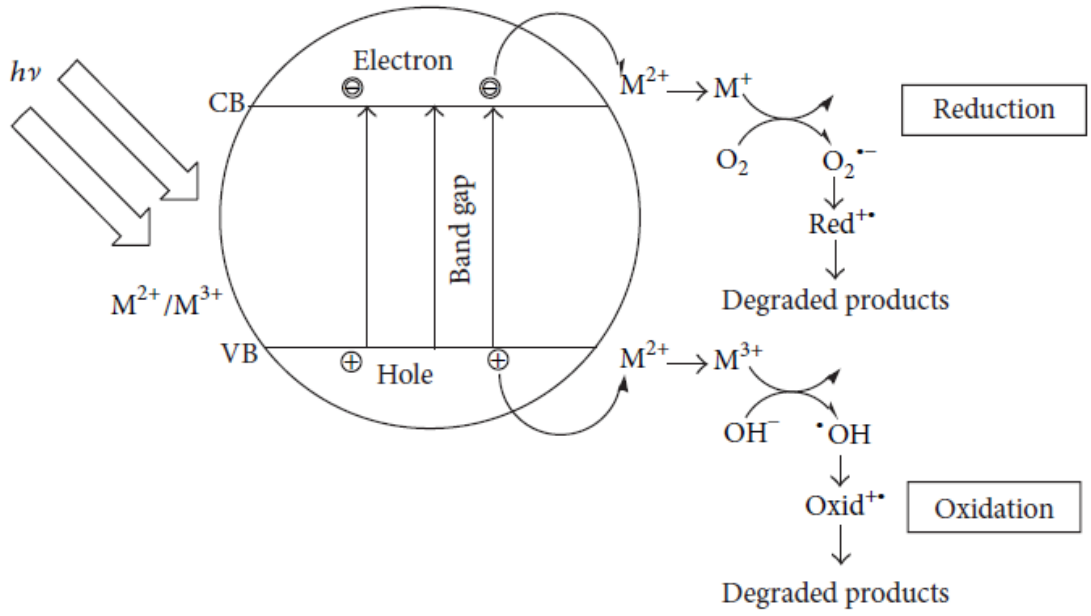

Figure 5. Mechanism for semiconductor photocatalysis.[60]

Unfortunately, the UV component of the natural solar light irradiation spectrum (the highest and cheapest illumination source) is quite small; moreover, titanium dioxide is not able to absorb the solar radiation in the visible region. Therefore, the scientific and technological research in this field is strongly involved to find new possibilities to enhance the overall efficiency. Two different strategies can be generically followed.

The first approach implies the use of opportunely doped ions able to decrease the absorbed band gap from the UV to the visible light (around 2.7 eV): in this model some transition metals, such as Fe, V, and Zn, have been widely tested and adopted. The second method is related to the increase of the intrinsic efficiency of the material through the control of the synthesis process; in this way, it is possible to control and govern important parameters such surface area, dimensions, and morphology, all affecting the photocatalytic activity. Further innovative systems have been recently developed, as to support the photocatalyst on the surface of luminescent materials, allowing an excellent increase in the degrading power and working time.

Furthermore, a challenging task is the efficient recovery of nanoscale TiO_2 from treated water. In this framework, many efforts have been made to achieve greater efficiency and new composite materials have been developed. Indeed, magnetic Fe_3O_4 NPs have been considered as a suitable support due to its outstanding superparamagnetism, flexible surface functionalization, and easily dispersity.

2 Magnetism at the nanoscale

In the following, the magnetic properties at the nanoscale level will be described. Dimension of the particles strongly affects the magnetic properties leading to a phenomenon called *superparamagnetism*.

2.1 Magnetic properties of bulk materials

All the elements, materials and compounds present in nature, in any physical state (solid, liquid or gaseous) can be distinguished in three categories: those that are totally indifferent to the action of a magnetic field (except for a fable negative signal), those that exhibit magnetic behavior, with a small positive signal, in the presence of a suitable field and those in which the magnetic behavior is also found in the absence of field.
What determines the membership of a material to a group rather than to the other is the presence of unpaired electrons. Magnetism is generated by the motion of electric charges: in a system, the magnetization (small or large) observed when the system is affected by a magnetic field, is related to the presence of atoms with incomplete atomic shells; the magnetic moment of the unfilled shell, given by the sum of orbital moment and the spin magnetic moment, is different from zero.
In this subdivision, substances belonging to the first group are defined as diamagnetic type: the molecules do not possess a moment of intrinsic magnetic dipole and there are no unpaired electrons. Diamagnetism can be regarded as originating from shielding currents induced by an applied field in the filled electron shells of ions. These currents are equivalent to an induced moment, opposite to the applied magnetic field direction, present on each of the atoms. All the materials exhibit a diamagnetic contribution, but when they have other magnetic properties, the effect is negligible because it is masked by other, much larger, effects (paramagnetism, ferromagnetism).
Materials that present more obvious magnetic effects can be classified as:
(a) paramagnetic, materials in which the unfilled shell of the atoms gives rise to a net magnetic moment per atom, with a distribution of the magnetic moments in the space producing a net magnetization equal to zero at every temperature. Under the action of an external magnetic field, the magnetic moments tend to align along the field direction, giving rise to a magnetization parallel with that of the field and with intensity proportional to the field itself;
b) ferromagnetic, materials in which a driving force (Molecular Field, Stoner criterion…) tends to align in the same direction all the magnetic atoms within a microscopically region named *magnetic domain.* The net magnetization of a single magnetic domain is different from zero, even if the requirement of minimization of the Magnetostatic Energy forces, in most of the cases, a random distribution of the magnetization vectors of the different magnetic domains in a macroscopic system with a vectorial sum equal to zero.
c) antiferromagnetic, materials in which the next neighbor magnetic moments are arranged in opposite directions giving to two (or more) magnetic sublattices; the moments show an antiparallel alignment and the resulting total magnetic moment is zero.
d) ferrimagnetic materials in which two (or more) magnetic sublattices with opposite direction of the magnetic resultant are again present but a) with a different magnetic moment per atom in each sublattice or b) a different number of atoms in each sublattice. In both cases, the magnetization is of

different amplitude in the two sublattices, resulting in total non-zero magnetic moment. Magnetite and other ferrites are ferrimagnetic.

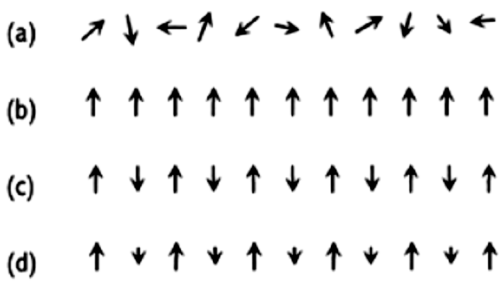

Figure 6. Magnetic moments orientation in a paramagnetic state (a), ferromagnetic state (b), antiferromagnetic state (c) and ferrimagnetic state (d).

When a magnetic material is placed into a magnetic field of magnitude $\boldsymbol{H}$, the magnetic induction $\boldsymbol{B}$ is the result of the following relation:

$$\boldsymbol{B} = \boldsymbol{\mu_0}(\boldsymbol{H} + \boldsymbol{M})$$

where $\boldsymbol{\mu_0}$ is permeability in vacuum and $\boldsymbol{M}$, given by the contribution of all individual atomic moments, is magnetization per volume unit.
In general, magnetic materials are classified in terms of magnetic susceptibilty $\boldsymbol{\chi}$, adimensional parameter defined as the derivative of magnetization with respect to the magnetic field. It can be written as follow in the presence of low field:

$$\boldsymbol{\chi} = \frac{\boldsymbol{M}}{\boldsymbol{H}}$$

For diamagnetic substances, susceptibility presents small negative values, as they are characterized by completely empty and completely full electronic shells. The electronic structure of the paramagnetic materials is instead made up of unpaired electrons: an applied field can cause magnetization of the material but the magnetization decays to zero in short time as soon as the field is removed.
Even ferromagnetic substances have unpaired electrons but the magnetic susceptibility $\boldsymbol{\chi}$ is positive and very high. When the sample is removed from the applied magnetic field $\boldsymbol{H}$, a residual magnetization $\boldsymbol{M_r}$ remains. Figure 7 is a clear representation of the main parameters and shows the hysteresis cycle curve, typical of a ferromagnetic material. For high magnetic field values, magnetization tends to a maximum value ($\boldsymbol{M_s}$) in which all magnetic moments are aligned in the direction of the magnetic field. To reset the residual magnetization of a ferromagnetic material, a magnetic field of intensity $\boldsymbol{-H_c}$ must be applied.

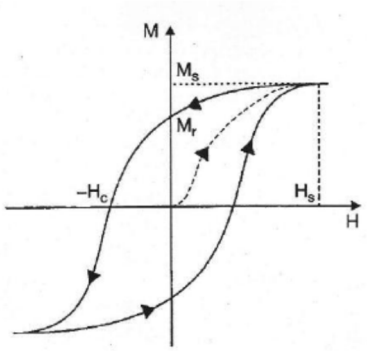

Figure 7. Typical hysteresis cycle, plotted as Magnetization (M) versus magnetic field (H), for a ferromagnetic material.

2.2 Superparamagnetism

The most interesting classes are *ferromagnets* and *ferrimagnets* since the alignment of the magnetic moments, within the material, can bring to a permanent magnetization. These magnetic properties arise from a particular microstructure. Indeed, magnetic moments are not coherently aligned all over the material, but they subdivide it into a multidomain structure to reduce the Magnetostatic Energy. Within each domain, the atomic moments are aligned along certain easy directions, related to electronic and structural properties of the material. At the same time, the total magnetization of each domain varies between the domains in order to minimize the magnetostatic energy. The number of these domains decreases by decreasing the dimensions of the material until the diameter of a small particle reaches a critical value (D_c). Below this value, the most stable structure is a single domain one, as shown in Figure 8.

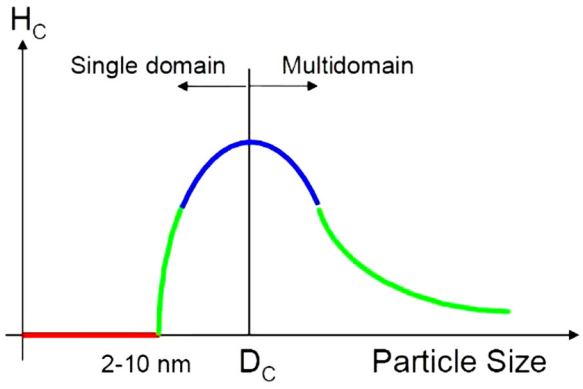

Figure 8. Dependence of coercive field (H_c) on dimension of particles. Below a critical diameter (D_c), with the *single domain* formation, the coercive field decreases up to zero for small particles.

This diameter is related to the characteristics of the material through the relation:

$$D_c \approx 18 \frac{\sqrt{AK_1}}{\mu_0 M_s^2}$$

where A is the stiffness constant, K_1 is the uniaxial anisotropy constant, μ_0 is the permeability constant and M_s is the saturation magnetization. Below this critical diameter, all the atomic magnetic moments are aligned and the particle still retains a remnant magnetization.

If the diameter is further decreased, the thermal energy k_BT (where k_B is the Boltzmann constant) becomes high enough to overcome the energy barrier between the two energy minima (parallel and anti-parallel to the easy direction). This behavior is called *superparamagnetism*. The critical diameter to obtain this state is related to the energy barrier between the two minima defined as:

$$E = KV \sin\theta$$

where K is the anisotropy energy constant, θ is the angle between the magnetization and the easy axis and V is the volume of the particle (Figure 9). The easy axis is defined as the energetically favorable direction of spontaneous magnetization.

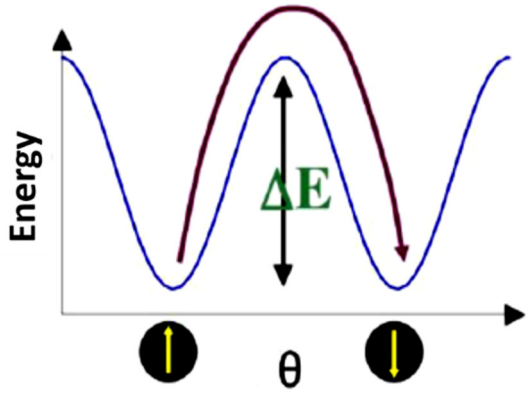

Figure 9. Energy barrier for the two minima states.

When $k_BT \gg KV$ the magnetic moment is able to reverse between the two preferred directions and the particles do not show coercive field or magnetization, behaving like a single paramagnetic atom, but carrying a giant moment. In fact, the difference with respect to a single atom is that the overall magnetic moment of the particle arises from the sum of all the atomic moments. Since these particles contains typically 10^5 atoms, the moment will be an order of magnitude higher than the one of a single atom: that's why the name *superparamagnetism*. These oscillations between the minima are characterized by a typical frequency and can be described by an Arrhenius type equation (valid for non-interacting nanoparticles):

$$\tau = \tau_0 e^{\frac{K_A V}{K_B T}}$$

where $\tau=2\pi/f$ (f is the oscillation frequency), K_A is the anisotropy constant, V is the volume of the particle, k_B is the Boltzmann constant and T the temperature.

As already mentioned, the possibility to flip between the two directions is strongly related to the temperature. If the thermal energy is decreased, it can be found a temperature below which the moment of the particle results frozen in a certain direction. This temperature, called *blocking temperature (T_B)*, is related to the dimension of the particles and to the material through the formula:

$$T_B = \frac{K_A V}{K_B \, ln \frac{\tau_m}{\tau_0}}$$

where K_A is the anisotropy constant, V is the volume of the particle, k_B is the Boltzmann constant, τ_m is the measuring time of the instrument and τ_0 is a constant. Measuring T_B, dimensional information about the magnetic system can be acquired.
The use of magnetic NPs in a superparamagnetic state is particularly appealing for different applications. In this case, the NPs strongly respond to an external magnetic field thanks to the collective behavior of the magnetic moments. At the same time, as soon as the external field is switched off, the NPs lose their magnetization, preventing the system from excessive agglomeration. This is the reason why most of the works involving magnetic NPs regard structures with diameter lower than D_c.

2.3 Exchange coupling

The advances in synthetic chemistry, leading to an extraordinary control of the growth parameters, has brought to the development of more advanced magnetic nanoparticles comprising two (or more) materials such as core/shell MNPs.[67,68] Much research into magnetism at the interfaces over the past decades has been driven by important and useful features, often simultaneously present, that can combine different functionalities (*e.g.,* catalytical, optical, magnetic or biomedical) of the diverse constituents bringing about novel and enhanced properties which are resulting in innovative applications of magnetic nanoparticles.
The key to the successful design of magnetic structures for applications, is the ability to manipulate and control magnetic properties. The basic energies involved are exchange and anisotropy, where the former controls magnetic ordering and the latter controls the preferred orientation.
Both parameters are phenomenological descriptions of fundamental correlations and energies associated with the electronic and crystalline structure of a material. A powerful technique for modifying and controlling magnetic characteristics is based on the use of magnetic heterostructures with properties governed by the interface region.
A particularly interesting topic in core/shell magnetic nanoparticles is the study of bi-magnetic core/shell nanoparticles, i.e., where both the core and the shell exhibit magnetic properties (ferromagnetic (FM), ferrimagnetic (FiM) or antiferromagnetic (AFM)). In these systems, the exchange interaction between both constituents brings about an extra degree of freedom to tailor the overall properties of the nanoparticles.[69,70]
A ferromagnet, such as iron, has a large exchange parameter but a relatively small anisotropy. This makes the ferromagnetic order stable at high temperatures but the orientation may not be highly stable, particularly if the dimensions are a few nanometres. Many antiferromagnets have large anisotropies and consequently very stable orientations. In heterostructures, exchange coupling between a ferromagnetic structure and an antiferromagnet one, in the same NP, can, in principle, produce a ferromagnetic behaviour with higher anisotropy. In such a structure, the anisotropy may behave as unidirectional feature not found in ferromagnets. This phenomenon is called *exchange bias* because the hysteresis loop associated with the ferromagnet/antiferromagnet structure can be centred about a non-zero magnetic field.

Since the discovery of the *exchange bias* (*i.e.*, the loop shift in the field axis of the hysteresis loops[71,72]) in Co/CoO nanoparticles,[73] FM/AFM and inverse AFM/FM core/shell nanoparticles as "hard/soft" and "soft /hard" NPs have been extensively studied.[74–76]

In recent years substantial advancement has occurred in this field, particularly in permanent magnets,[77,78] magnetic recording media,[79] microwave absorption, ferrofluids or biomedical applications, where it has been shown that, for certain applications, the use of bi-magnetic core/shell nanoparticles can be advantageous over single magnetic nanoparticles.

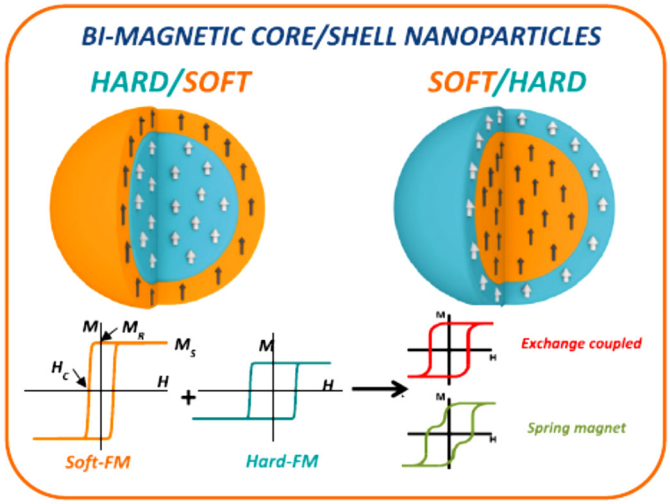

Figure 10. Schematic representation and hysteresis cycles for "hard/soft" and "soft/hard" core-shell NPs.[80]

Many of the biomedical applications of magnetic nanoparticles are based on the high values of the saturation magnetization avoiding at the same time excessive agglomeration. Thus, most of these applications are based on the use of superparamagnetic nanoparticles.[81] In these cases, there is no real need for hard-soft core/shell nanoparticles. However, in other applications the use of bi-magnetic core/shell nanoparticles can be desirable.

Indeed, the academic research on biomedical applications is also strongly focused on hyperthermia. Magnetic hyperthermia, described in the previous chapter, is based on the phenomenon that occurs when nanoparticles are subjected to an alternating magnetic field leading to heat production. Three main mechanisms are involved in hyperthermia, namely Brownian relaxation, Néel relaxation and hysteresis loss, although for magnetically blocked nanoparticles only hysteresis loss is prevalent.[82] Hence, the Specific Loss Power (*heating efficiency*) (SLP) of nanoparticles depends on material, size, composition, frequency and intensity of the applied alternating magnetic field.[22]

SLP, expressed as W/g, can be evaluated with the following equation:

$$SLP = f \cdot \frac{A}{\rho}$$

where A is the area of the hysteresis loop, f is the frequency of the measurement and ρ is the concentration of MNPs in the sample.

Since heat dissipation depends on intrinsic material parameters such as K_u, the anisotropy constant, and M_S, the saturation magnetization, the combination of two phases in a core/shell structure can be advantageous to enhance the response of the material to the AC field. Experimentally, it has been demonstrated that the combination of different magnetic soft/hard or hard/soft ferrite core/shell particles (e.g., $MnFe_2O_4/CoFe_2O_4$ or $CoFe_2O_4/MnFe_2O_4$) leads to enhanced SLP values compared to

single phase ferrite particles.[83] Remarkably, inverse core/shell systems exhibit larger SLP values than conventional hard/soft structures.[84] Moreover, further enhancement of the SLP values has been obtained in cubic soft/hard core/shell nanoparticles, with SLP values in excess of 10000 W/g. The decrease of the surface anisotropy and the size of the particles (60 nm) appear to be key factors for achieving SLP values higher than the one obtained for the spherical single component ferrite particles and higher than that of exchange-coupled spherical nanoparticles.[83]

3 Magnetic NPs for biomedical applications

In this part of the thesis, the investigation of iron oxide-based nanostructures for biomedical purposes is reported. The work can be divided into two main parts, drug delivery and hyperthermia.
In both projects, the experimental part has been focused on the synthesis and chemico-physical characterization of functionalized magnetic nanostructures.
In the following, a first section will be devoted to describe nanoparticles designed for drug delivery activities; then, in the second part the synthesis and characterization of ferrite NPs with preliminary results as hyperthermia factors will be described.

3.1 Drug delivery nanovectors

In this section, the drug delivery work will be divided into two main parts: the first part deals with the conjugation between magnetite based NPs to an organic moiety formed by a tripeptide coupled to a fluorescent molecule and the consequent enzyme activated cleavage. The second part is dedicated to a research activity, carried out in collaboration with the University and CNR of Bari (Italy), focused on the study of micellar and solid lipid nanovectors encapsulating SPIONs and loaded with Sorafenib, a drug for hepatocellular carcinoma treatment.

3.1.1 Coupling and enzymatic cleavage of 1-Pyrenemethylamine

A complex system for potential drug delivery or other biomedical applications has been studied. The aim of the work was to proof its potential use as magnetic drug delivery system. The nanovector should be directed to the tumor site, through the application of a magnetic field, where protease enzymes as plasmin, overexpressed on tumor cells, cleaves the "drug".
As reported in Figure 11 and explained hereafter, the system was based on the conjugation of a tripeptide linked to a fluorescent molecule, 1-pyrenemethylamine, to magnetite NPs through a linker, APTES.

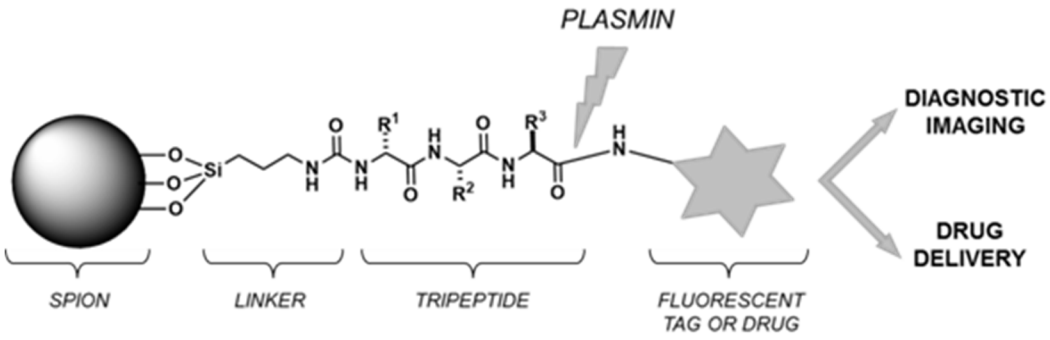

Figure 11. Scheme of the NPs conjugated to tripeptide-pyrene; possible applications are also shown.

As the specifier peptide, on the basis of previous work by others and of our own experience, the most suitable choice was a tripeptide to grant selectivity by plasmin or other similar proteases. It is well known that plasmin is selective for lysine as the scissile aminoacid, while an unpolar aminoacid, such

as leucine, is preferred as second position. For the last position any aminoacid can be used, but, as suggested by Carl et al.,[85] a D-Amino acid is preferred for the amino terminus to prevent degradation of the peptide specifier by other proteases. In the previous related work by Cheng and coworkers, a simpler dipeptide was instead employed.[86]
Hence, the tripeptide is formed by three aminoacids ordered in this way: D-Valine – D-Leucine – L-Lysine; the latter aminoacid lysine is placed in the farthest position from the nanoparticle surface and is linked to the fluorescent tag (see compound **7** in scheme of Figure 13).
Furthermore, the choice of the spacer was not trivial, since both the specifier peptide and the APTES functionalized NPs ends with an amino group. We selected two possible ways to join these two amines: i) the transformation into a urea; ii) the coupling with a dicarboxylic acid. In this latter case, the dicarboxylic acid needs to be quite long, in order to prevent intramolecular imide formation,[87] with detachment of the specifier peptide from the nanoparticle.

In order to study the best conditions and approaches for both the coupling and the enzymatic release, two different ways were followed (Figure 12):
A) coupling the tripeptide-pyrene to the already APTES functionalized NPs;
B) coupling APTES to tripeptide-pyrene before conjugating the whole molecule to the NPs.

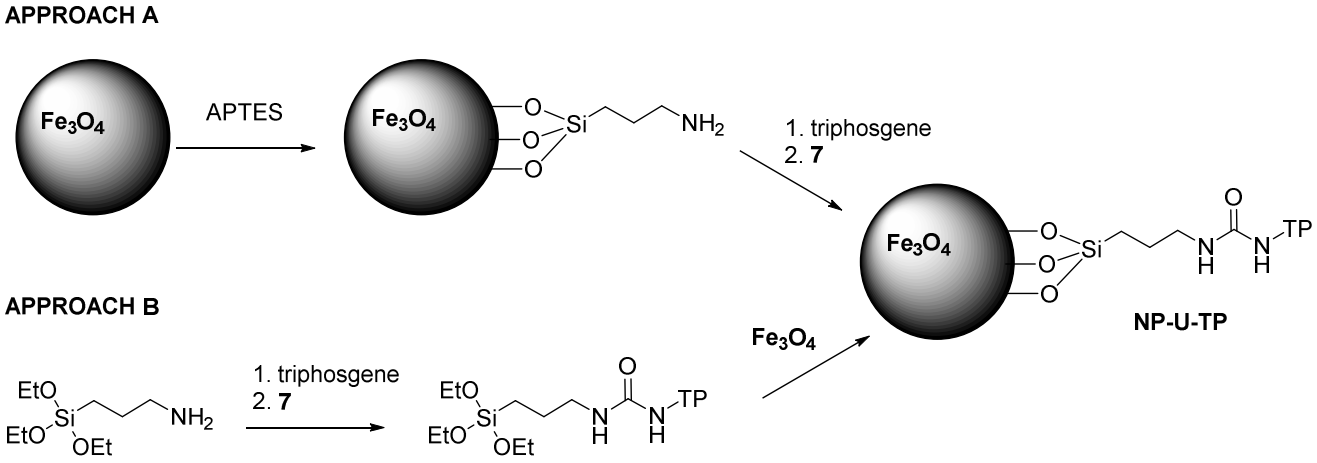

Figure 12. Approaches adopted for the conjugation. Approach A: APTES functionalization before coupling tripeptide; Approach B: APTES coupling to tripeptide before conjugation to NPs.

The nanostructure resulting from the two procedures is the same and has been named **NP-U-TP**, indicating that the coupling is induced via a urea bridge (U) between APTES functionalized nanoparticles (NP) and tripeptide-pyrene (TP).
The best approach, due to the chemical properties of APTES that cause complex problems in manipulation and purification treatments, was based on a first functionalization of the NPs with APTES and then the coupling to tripeptide-pyrene (approach A).
Concerning the consequent enzymatic release, due to the high cost of plasmin, only tests on the organic substrate were performed with it. To explore the cleavage of 1-pyrenemethylamine on real samples containing NPs, the enzymatic release was performed with trypsin, after a careful comparison of the activity of the two enzymes.

The other way of bonding TP to NPs was the coupling through a dicarboxylic acid. In our opinion, the best additional linker was found to be the monomethyl azelate, a nine-carbon chain acid (C9), which allowed to obain the sample defined as **NP-C9-TP**.

In the next paragraphs, the synthesis of the tripeptide based molecules, magnetite nanoparticles, their functionalization and conjugation will be described.

3.1.1.1 Synthesis of Tripeptide-pyrene compounds

In Figure 13, a scheme for the synthesis of the tripeptide-pyrene compound (**7**) is reported. **7** will be conjugated to magnetic NPs via urea bond to form **NP-U-TP**, as reported in Figure 9.

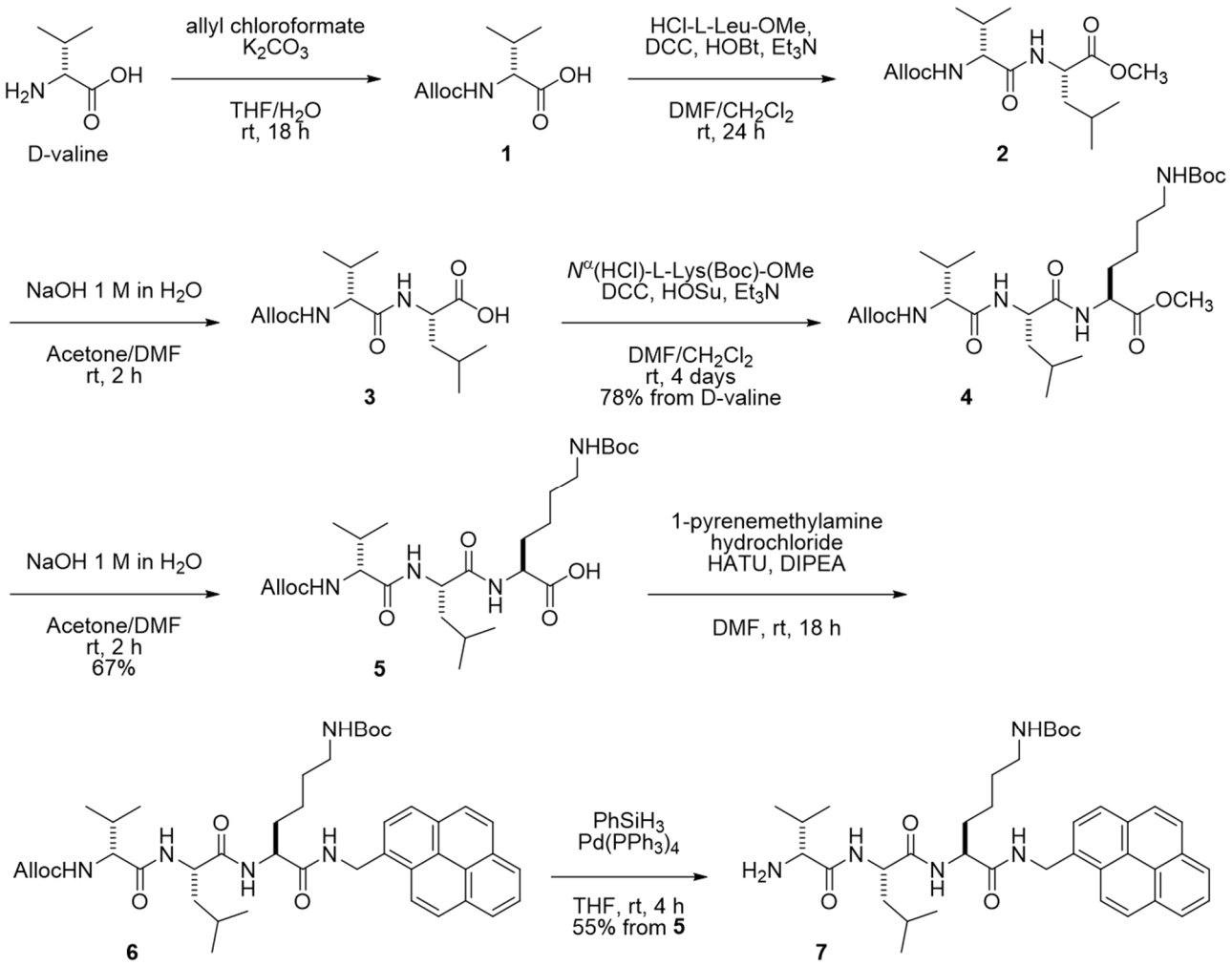

Figure 13. Scheme for the synthesis of tripeptide-pyrene. D-valine is coupled to L-leucine and then to L-lysine to obtain **5**; after saponification, pyrenemethylamine is added and coupled to the tripeptide **6**. A deblocking step to remove the Alloc group is needed to obtain the final product **7**.

Figure 13 reports the scheme for the synthesis of the tripeptide specifier and the coupling to the fluorescent amine. For our purposes, two orthogonal protections for the D-Valine and the amino groups are strongly required. Particularly crucial is the protection of ε-Lysine, since it was planned to be removed as the last step after linking to the nanoparticles. We selected the Boc protecting group thanks to its easy removal that releases no side-products. Moreover, we chose to perform the synthesis from left to right, contrary to what is typically done, to prevent use of further protecting groups as Fmoc that is found to be quite troublesome in the synthetic procedure. In this way, performing the synthesis from left to right we selected the Alloc as protection for D-Valine.

Thus, D-Valine was smoothly protected as allyloxycarbamate under Schotten-Baumann conditions[88] and then coupled with L-leucine methyl ester hydrochloride using DCC and HOBt. The resulting

dipeptide methyl ester was hydrolyzed under basic conditions and coupled with N_{ε}-Boc-L-lysine methyl ester hydrochloride using DCC and HOSu affording compound **4** with excellent yield from the starting amino acid.
Coupling of product **5** with 1-pyrenemethylamine was more troublesome from the stereochemical point of view. After testing several coupling agents and bases using benzylamine as model compound, we found out that the best one was HATU in combination with DIPEA. The crude coupled product was directly deprotected at the *N*-terminus without intermediate isolation.
Even this deblocking step was problematic. Optimization was carried out on the benzyl ester of **3**. Different solvents (THF and DCM) and scavengers (pyrrolidine, $PhSiH_3$, thioanisole, dimedone and triethylammonium formate) were investigated maintaining $Pd(PPh_3)_4$ as the source of Pd(0). We found that the combination of a high excess of $PhSiH_3$ and THF as solvent were the best conditions. The optimized conditions were then applied to the real system, affording **7** in 55% yield over 2 steps. The moderate yield was mainly due to the high insolubility of all pyrene containing compounds in most organic solvents leading to the loss of material during the workup and the purification. Preliminary experiments of conjugation with Fe_3O_4 nanoparticles functionalized with APTES showed that the purification of **7** was essential. In fact, the presence of the excess of $PhSiH_3$ and the residues of Pd were detrimental for the conjugation reaction.

In the case of insertion of the longer spacer, **7** was modified to obtain **9** coupling it with the monoester of azelaic (nonanedioic) acid. The presence of a carboxylic acid as terminus of the aminoacidic left chain allowed to employ milder conditions for conjugation of the tripeptide to the nanoparticles.

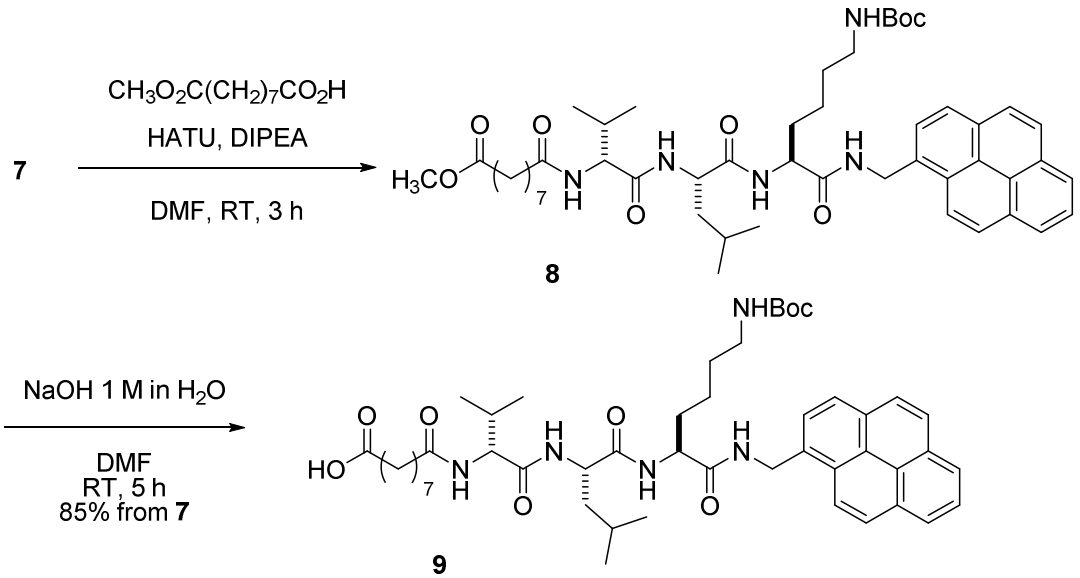

Figure 14. Scheme of synthesis of azelate-tripeptide-pyrene starting from **7**.

After saponification of **8**, the acid **9** was coupled to the functionalized nanoparticles.

3.1.1.2 Synthesis of APTES functionalized magnetite NPs

Magnetite nanoparticles were prepared according to Massart procedure.[89] Briefly, $FeCl_2 \cdot 4H_2O$ (2.5 mmol) and $FeCl_3 \cdot 6H_2O$ (5 mmol) were dissolved in Milli-Q water at pH 2 under N_2 atmosphere and vigorous mechanical stirring. Once the solution reached 75 °C, a proper amount of NaOH aqueous solution (100 ml, 2 M) was quickly added, causing the sudden appearance of a black precipitate. The reaction was continued for 20 min, after which the particles were washed several times with boiling water and magnetically collected after each wash, in order to reach neutral pH.

APTES functionalization was achieved dispersing Fe_3O_4 NPs in water (40 mL, 1 g/L) and adding 40 mL of ethanol and 1.6 mL of 2% v/v solution of APTES. The reaction was carried out at 50 °C for 24 h under vigorous mechanical stirring.

The sample was magnetically washed several times using first ethanol and then Milli-Q water and then stored under vacuum.

3.1.1.3 Conjugation to tripeptide-pyrene: synthesis of NP-U-TP

The urea linked sample (**NP-U-TP**) was obtained with an initial transformation of the amino groups of APTES into isocyanate groups, as here described.

NP@APTES (28.6 mg) were dispersed in dry DCM (2 mL) under N_2 atmosphere. Et_3N (19 µL, 0.135 mmol) and triphosgene (5.4 mg, 0.018 mmol) were added at 0 °C. The mixture was stirred at RT for 20 min; then the solvent was evaporated and the nanoparticles were dispersed in dry THF (2 mL) under N_2 atmosphere. Then, DIPEA (15 µL, 0.086 mmol) and **7** (28.6 mg, 0.043 mmol) were added. The reaction occurred in oil bath at 50 °C for 18 h. The final material was magnetically washed with EtOH and stored under vacuum.

In Figure 15, a scheme of the conjugation of tripeptide-pyrene to NP@APTES is reported.

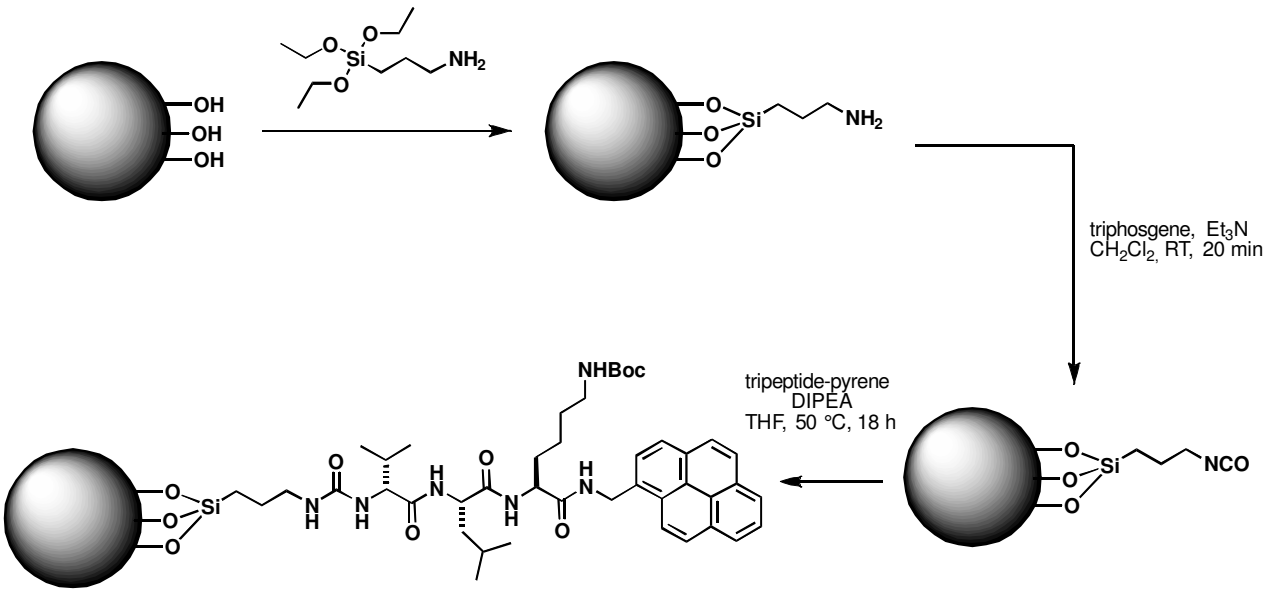

Figure 15. Scheme of the conjugation of tripeptide-pyrene to NP@APTES through the formation of a urea bridge between the two compounds.

3.1.1.4 Conjugation to azelate-tripeptide-pyrene: synthesis of NP-C9-TP

NP-C9-TP was prepared as here described: 30 mg of NP@APTES were dispersed in dry DMF (1 ml) under N_2 atmosphere. **9** (30 mg, 0.036 mmol), DIPEA (31 µL, 0.178 mmol) and HATU (14 mg, 0.037 mmol) were added. The dispersion was mechanically stirred for 18 h at RT. The final material was magnetically washed with EtOH and stored under vacuum.

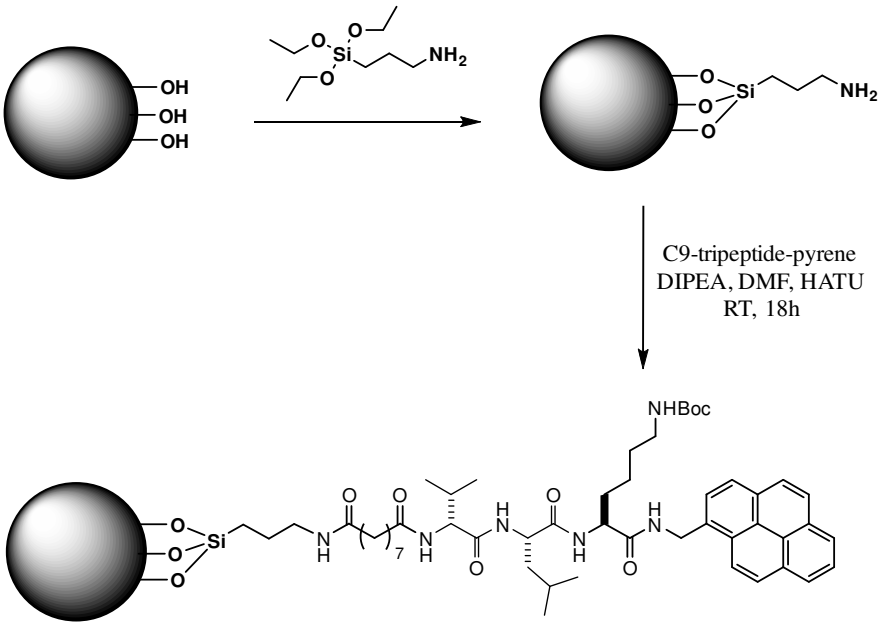

Figura 16. Scheme of the preparation of NP-C9-TP.

3.1.1.5 Chemico-physical characterization

In this section, the characterization of NP-U-TP and NP-C9-TP will be shown and discussed.

Morphological and compositional analyses

In Figure 17, a FE-SEM image of Fe_3O_4@APTES nanoparticles is presented. EDXS analysis confirms the presence of the expected elements in the nanostructures, namely iron, silicon, and oxygen. Cu and C peaks are related to the copper grids used to deposit a drop of sample.

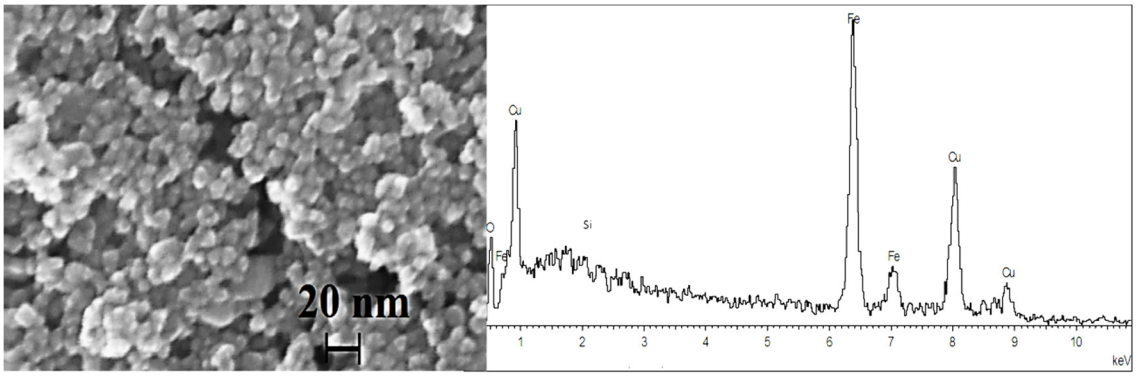

Figure 17. FE-SEM image of NP@APTES and related EDXS spectrum.

The sample is characterized by large aggregates, due to the magnetic interactions among particles, in which single nanoparticles with mean diameter of about 10 nm can be observed.

Fluorescence analyses

In Figure 18, the fluorescence spectra of molecules (**7** and **9**) and the related conjugated NPs, **NP-U-TP** and **NP-C9-TP** respectively, are reported. The analyses were performed in DMSO using an excitation wavelength equal to 346 nm. No fluorescence signal was detected for Fe_3O_4@APTES nanoparticles (not reported).
The fluorescence spectra of **7** and **9** are ascribed to the fluorescent spectrum of pyrene which is characterized by a set of four major bands with well-defined peaks at ~375, 388, 398, and 415 nm, respectively.

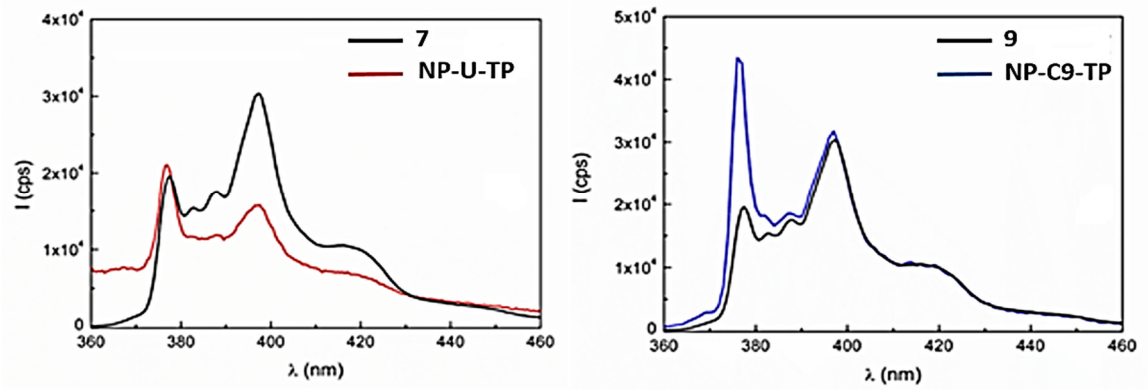

Figure 18. Fluorescence spectra of **7** (black line) and **NP-U-TP** (red line); on the right, **9** (black line) and **NP-C9-TP** (blue line).

The peaks are attributed to the $\pi \rightarrow \pi^*$ transitions and are cumulatively defined as monomeric emission. The peak at 375 nm corresponds to the first vibronic band with a 0 – 0 transition, while the one at 388 nm is attributed to the third vibronic band with a 0 – 2 transition.[90,91]
The coupling reaction between NP@APTES and **7** or **9** caused a slightly different emission profile: all the peaks related to pyrene derivatives were detected but a variation of intensity occurred, especially for band I (378 nm) and band III (398 nm). This evidence can be ascribed to the effective coupling occurred on the surface of the nanoparticles, that affects the mobility of the molecules, forcing them in fixed configurations.

ThermoGravimetric Analysis

Nanoparticles based samples were investigated through thermogravimetric analysis to evaluate the loading of tripeptide-pyrene or azelate-tripeptide-pyrene on the surface of NP-U-TP or NP-C9-TP respectively.
NP-U-TP: A loading amount of **7** equal to 5.3 % was found out.

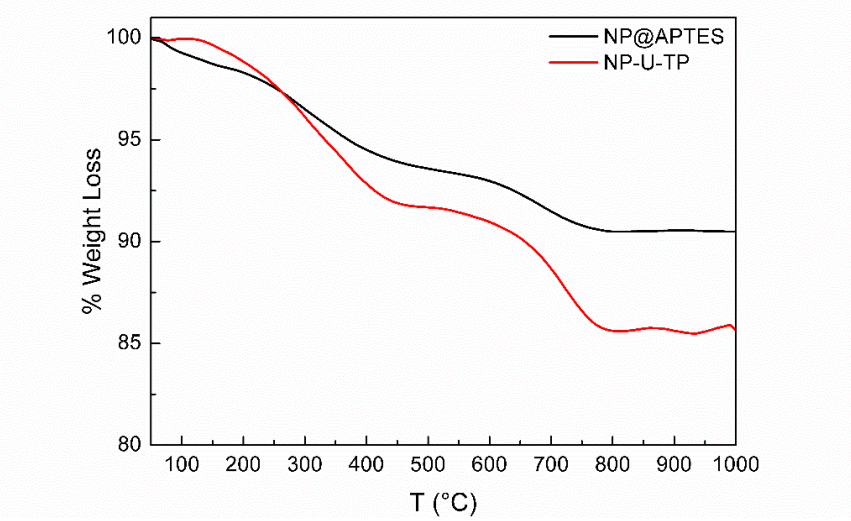

Figure 19. TGA curves of NP@APTES (black line) and NP-U-TP (red line).

NP-C9-TP: The loading amount of **9** was equal to 15.5%.

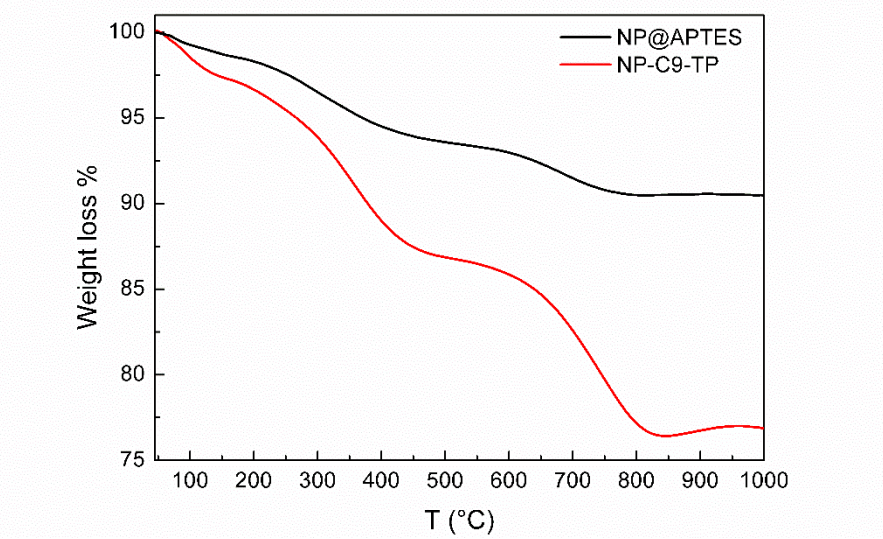

Figure 20. TGA curves of NP@APTES (black line) and NP-C9-TP (red line).

Through the comparison with the TGA analysis performed on NP@APTES, which provided a value of 9.5% of silane attached on the surface of magnetite NPs, it was possible to calculate the loading results of NP-U-TP and NP-C9-TP.

It is evident that there is a relevant difference between the two loadings, suggesting that the milder coupling conditions used for NP-C9-TP brought to a more efficient loading, improving the amount of 1-pyrenemethylamine anchored to the NPs.

InfraRed analyses

IR analyses are a qualitative tool to confirm the conjugation of tripeptide-pyrene to APTES functionalized nanoparticles. Fingerprint signals deriving from tripeptide-pyrene are detectable in the spectrum of NP-U-TP (green curve).
In particular, carbonyl and amide bands at about 1500-1600 cm^{-1} are the most intense signals.

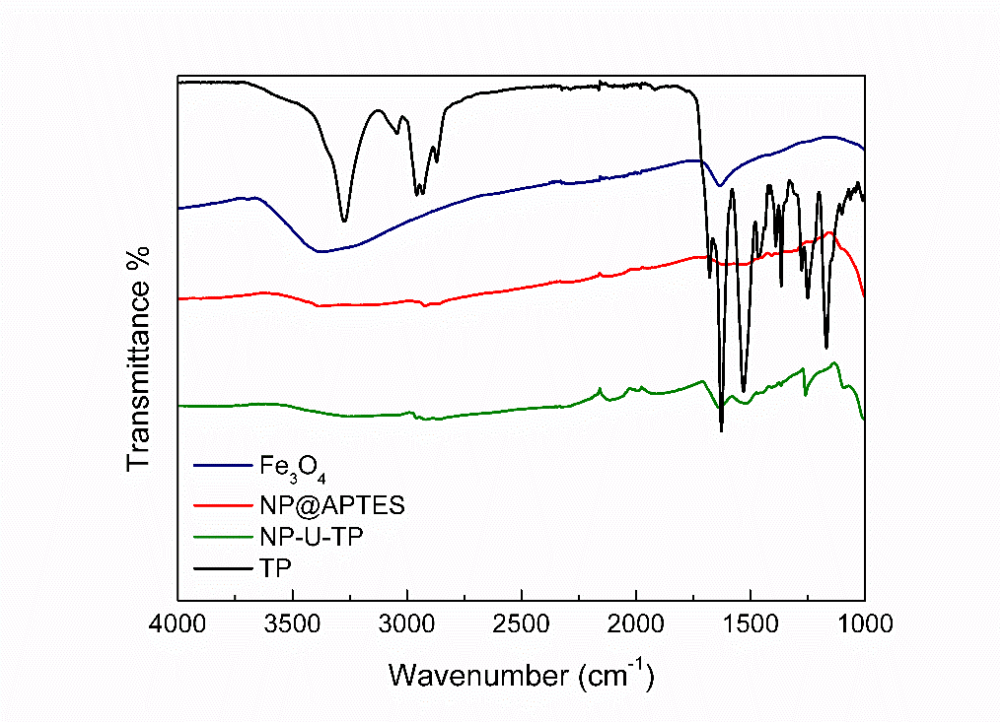

Figure 21. FT-IR spectra of the samples concerning NP-U-TP.

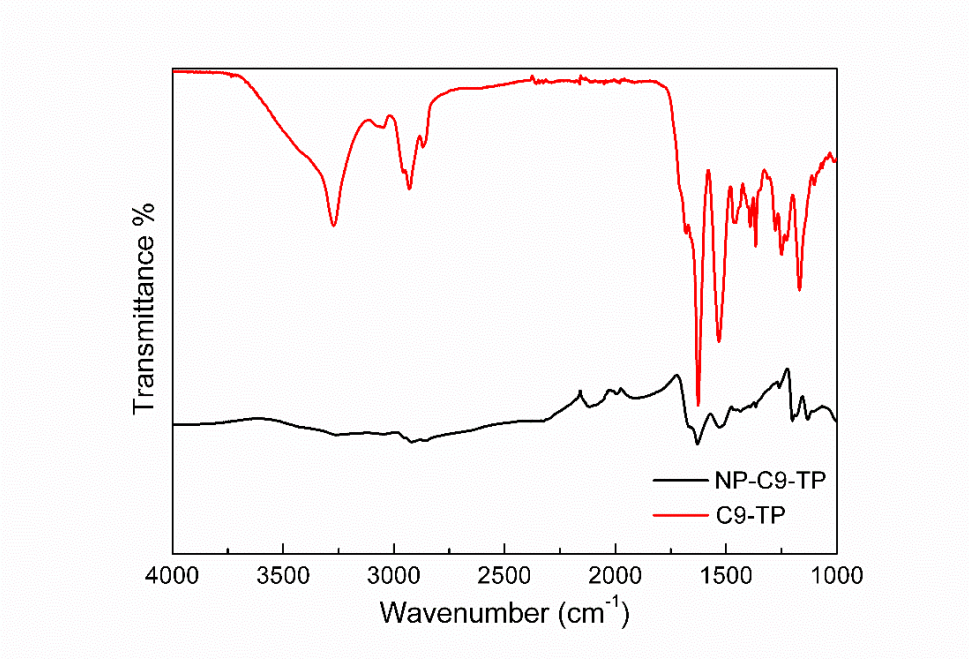

Figure 22. FT-IR spectra of NP-C9-TP (black curve) and the azelate-tripeptide-pyrene (red curve).

As occurred for NP-U-TP, even for NP-C9-TP, the signals related to carbonyl and amide groups deriving from the aminoacids sequence and azelate linker are the most easily detectable around 1500 and 1600 cm^{-1}.

Magnetic measurements

Magnetic properties of **NP-C9-TP** were investigated by measuring the hysteresis cycles at 300 K before and after the enzymatic cleavage (NP-C9-T + P): saturation magnetization values of about 60 A m^2 Kg^{-1} were observed for all the samples, confirming that the material was not degraded in the synthetic procedures and in the enzymatic cleavage.

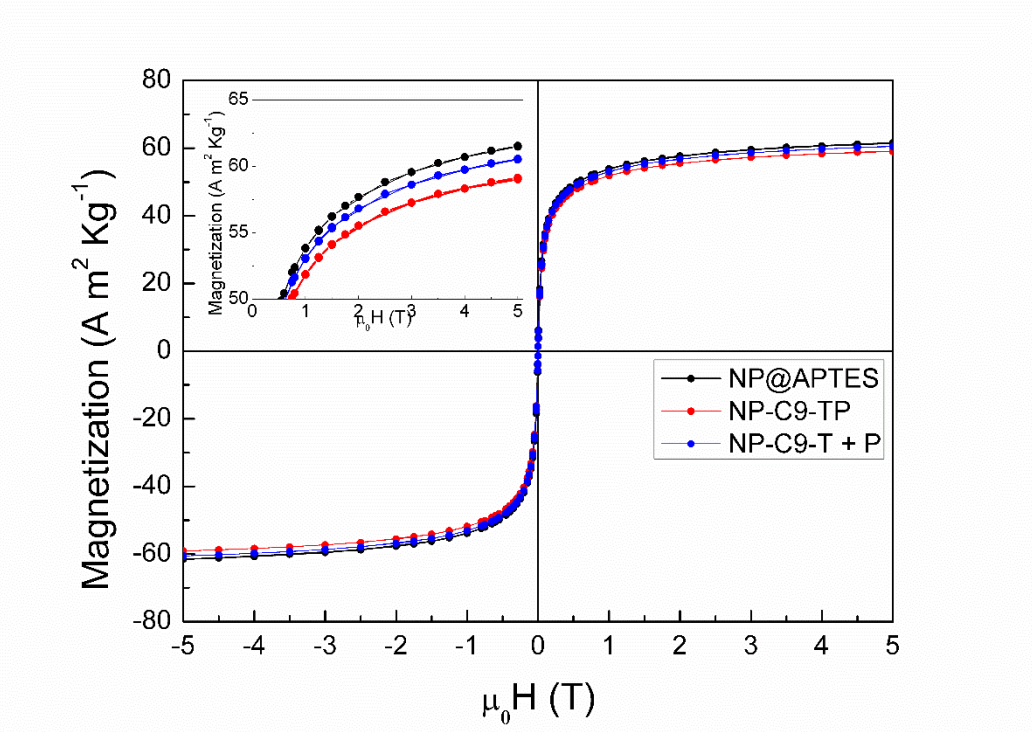

Figure 23. Hysteresis cycles recorded at 300 K for **NP@APTES**, **NP-C9-TP** and **NP-C9-T + P**. The inset represents an enlargement of saturation magnetization of the three samples.

3.1.1.6 Enzymatic cleavage

Compound **7** was deblocked at the ε-Lysine aminogroup to furnish diamine **10**, which was used as model for the enzymatic reaction and for assessing analytical detection of the released fluorescent amine. The enzymatic assay was tested with both Plasmin and Trypsin, following the kinetics of the hydrolysis by HPLC-FLD.

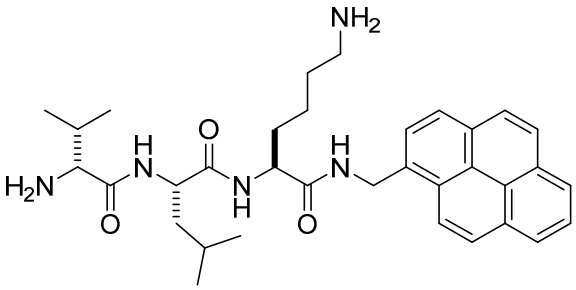

10

The Boc deprotection followed the procedure hereafter described. A solution of **7** (13 mg, 0.0198 mmol) in dry DCM/TFA 20:1 (2.0 mL, 0.01 M) was stirred at RT for 2 h. After removal of the volatile components, the residue was taken up with *n*-heptane (× 3) and the solvent was evaporated again to give **10** as an off-white solid that was quantitatively transferred to a 10 ml graduated flask with MeOH obtaining a 1.98 mM stock solution of **10**.

3.1.1.7 Enzymatic reactions on substrate (10)

TRIS buffer pH 7.5 was freshly prepared by dissolving 3.64 g of TRIS in 50 ml of deionized water and subsequent addition of 1N HCl until pH 7.5 (measured by pH-meter). The volume was adjusted to 100 ml in a volumetric flask with deionized water.
0.3 U/ml stock solution of Plasmin from human plasma (Sigma-Aldrich P1867-150 µg) was prepared by dissolving 150 µg of lyophilized powder in 1 ml of TRIS buffer.
0.1 mg/ml and 0.5 mg/ml stock solutions of Trypsin from porcine pancreas (Sigma-Aldrich T4799) were prepared by dissolving 5 mg of enzyme in 50 ml and 10 ml of TRIS buffer respectively.
10 (25 µl of stock solution, 50 nmol), Plasmin (77 µl of stock solution, 0.023 U) and 730 µl of TRIS buffer were added in a 2 ml Eppendorf.
10 (25 µl of stock solution, 50 nmol), Trypsin (46 µl of stock solution, 1:6 w/w enzyme:substrate) and 760 µl of TRIS buffer were added in a 2 ml Eppendorf.
Each enzymatic reaction was carried out at 37 °C in Thermomixer (650 rpm) and was monitored after 24 h, 48 h and 72 h by HPLC-FLD.

	TRYPSIN		PLASMIN	
	Area (%)		Area (%)	
	Substrate	Product	Substrate	Product
24 h	3.3	96.7	11.1	88.8
48 h	3.5	96.5	6.2	93.8
72 h	1	99	4	96

Table 2. Area % of enzymatic cleavage promoted by Trypsin and Plasmin in 24h, 48h and 72 h.

In a 72 hours time span, around 100 % of enzymatic release, measured with respect to area percentage, was achieved both with Plasmin and Trypsin. In Figure 24, chromatograms of the solutions resulting from the enzymatic reactions are presented.

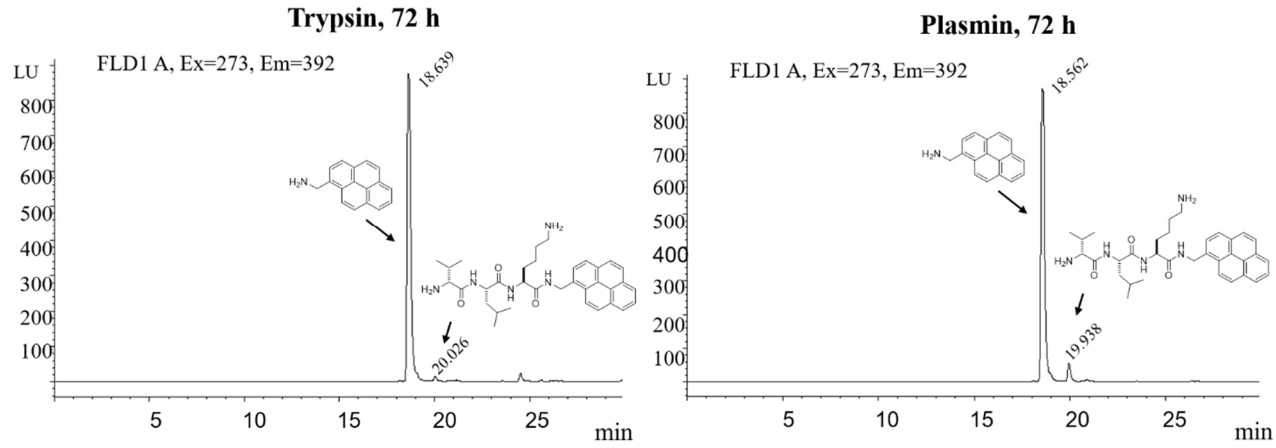

Figure 24. HPLC chromatograms of the enzymatic cleavage obtained with Trypsin (left) and Plasmin (right) after 72 h reaction.

The results showed that both enzymes efficiently recognized the substrate and that after 72 h the conversion was almost complete. These experiments also demonstrated that Plasmin can be replaced by the most available Trypsin, thus allowing its use in the experiments performed on nanoparticles based materials.

3.1.1.8 Enzymatic hydrolysis on NP-U-TP and NP-C9-TP

As occurred for the enzymatic cleavage of substrate **10**, the Boc cleavage is required to proceed with the enzyme promoted release on NPs. In a vial containing **NP-U-TP** (10 mg) or **NP-C9-TP** (20 mg) a solution dry DCM/TFA 20:1, 200 µL or 400 µL respectively, was added. The reaction proceeded for 4 h under vigorous shaking. The sample was then dried and used for the enzymatic cleavage without any further purification.
In an Eppendorf containing **NP-U-TP** after Boc cleavage, 975 µL of 0.1 mg/mL Trypsin stock solution was added. The final volume was adjusted to 1 mL with TRIS buffer.
In an Eppendorf containing **NP-C9-TP** after Boc cleavage, 920 µL of 0.5 mg/mL Trypsin stock solution was added. The final volume was adjusted to 1 mL with TRIS buffer.
A ratio of 1:6 enzyme/substrate was maintained in both cases. The samples were kept under shaking in Thermomixer (650 rpm) at 37 °C for 72 h.
The samples were then washed several times with MeOH using both magnet and centrifuge (Eppendorf 15000 rpm 10 minutes each) recovering the washings in a volumetric 10 ml flask.

In this case, HPLC-FLD was not suited for following the enzymatic reaction on the nanoparticles. Thus, we generated a calibration curve to quantify the released 1-pyrenemethylamine through HPLC-VWD (Variable Wavelength Detector). The sample injected in the HPLC-VWD was preconcentrate by a factor of 20.

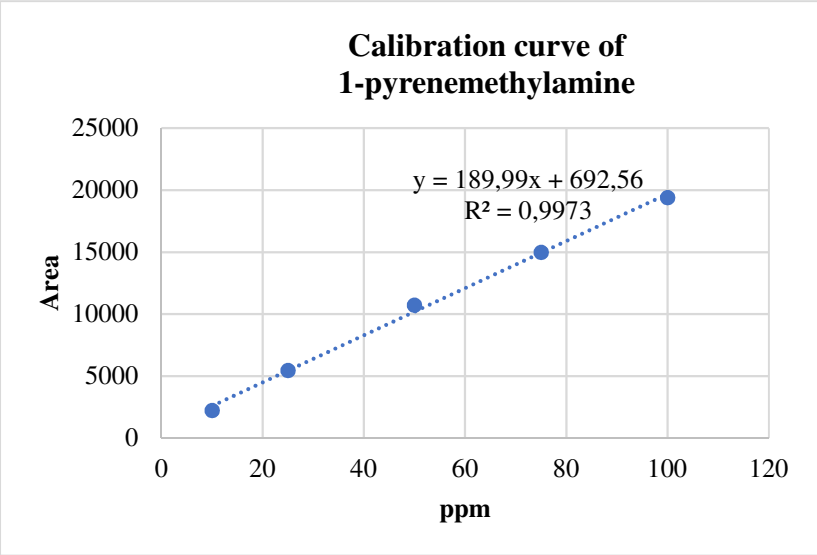

Figure 25. Calibration curve for determination of 1-pyrenemethylamine.

The determination of 1-pyrenemethylamine in the buffer after trypsin hydrolysis on NPs samples was performed by HPLC-VWD. By comparison with the calibration curve and from the loading determined by TGA, it was possible to determine the released µmols of 1-pyrenemethylamine that were 7.1% and 5.8% for the urea spacer and for the azelate spacer respectively.
Thus, although the enzymatic reaction was actually possible when the specifier tripeptide is anchored to magnetic NPs, the rate of reaction is considerably low. Clearly, the presence of the nanoparticle and the length and nature of the spacer influence the enzymatic activity. Although the longer azelate spacer produced a higher loading of TP, the release was not so high, showing that the shorter urea spacer was even better from this point of view. The lipophilic nature of the longer spacer may have caused aggregation phenomena that have made the access to the active site more difficult.

3.1.2 SPION/Sorafenib/Micelles

Currently, Sorafenib is the only systemic therapy capable of increasing overall survival of patients affected by hepatocellular carcinoma. Unfortunately, its side effects, particularly its overall toxicity, limit the therapeutic response that can be achieved.
In this work, SPIONs have been encapsulated into PEG modified micelles loaded with Sorafenib and the cytotoxicity was evaluated on human liver cancer cell lines (HepG2) using the MTT assay. Furthermore, magnetic accumulation experiments in a dynamic flow circuit were carried out to simulate a blood circulation for future *in vivo* applications.
The preparation of SPIONs/Sorafenib/micelles and the in vitro tests were carried out in the laboratories of CNR and University of Bari, while the magnetic characterization and the flow circulation simulation were carried out in the laboratories of the University of Genoa.

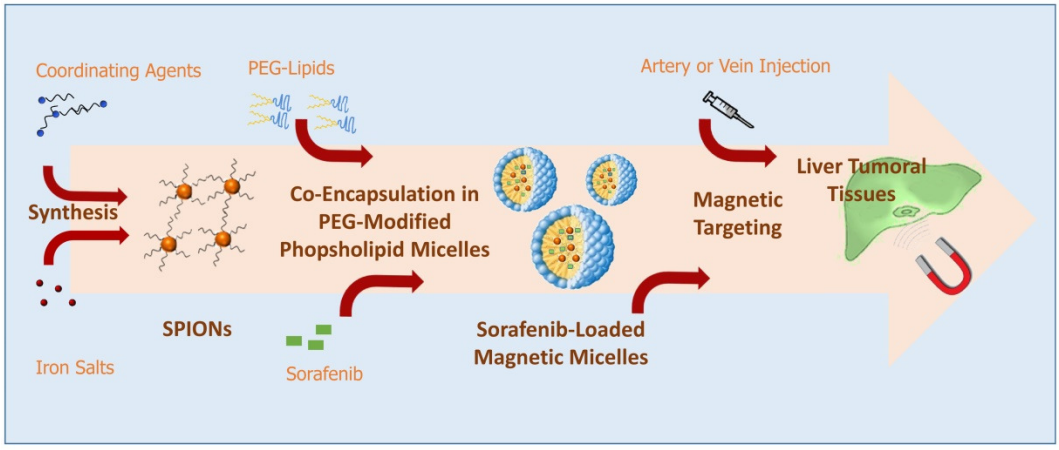

Figure 26. Fabrication route of PEG-modified phospholipid micelles loaded with sorafenib and SPIONs and their possible application for magnetic targeting to liver tumors.

Nanoformulations based on polyethylene glycol modified phospholipid micelles, loaded with both SPIONs and Sorafenib, were successfully prepared and thoroughly investigated by complementary techniques.

Four different samples were synthesized and magnetic measurements, performed in a DC-SQUID magnetometer (MPMS Quantum Design) allowed to evaluate the content of SPIONs inside micelles. The starting weight percentages used in the synthesis were: 16 % (sample a), 20 % (sample b), 24 % (sample c) and 28% (sample d).

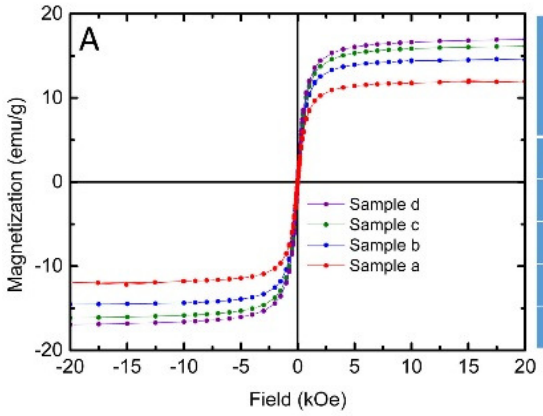

B

Sample	M_s (emu/g)	Real SPION Weigth (%)
Bare SPIONs	56.5	100
Sample a	11.9	21
Sample b	14.5	26
Sample c	16.2	28
Sample d	17	30

Figure 27. (A) RT Hysteresis cycles of PEG-micelles loaded with different SPIONs content. (B) Real SPIONs weight percentage in the four different PEG-micelles samples calculated from RT saturation magnetization (Ms) values.

Hysteresis cycles performed at room temperature confirmed the superparamagnetic nature of the nanoparticles. Furthermore, through the comparison with the measurement on bare SPIONs, it was possible to evaluate the content of magnetic nanoparticles embedded into micelles, as reported in Figure 27.

In fact, the real SPIONs content was calculated to be 21 % (sample a), 26 % (sample b), 28 % (sample c) and 30 % (sample d).

A key issue in magnetic delivery is whether SPIONs can be effectively confined to target regions of the body against blood flow which tends to transport them away. Therefore, the behavior of the SPIONs/micelles was investigated by using an *in vitro* system simulating the blood flow rates in the liver. In particular, a dynamic circuit used to simulate the blood flow in the liver of human body and

composed of an accumulation vessel (1), a peristaltic pump (2), a digital fluxmeter (3), a homemade differential pressure sensor (4-6), the magnetic accumulation system (5) and a sampling holder (7) was appositely designed and realized (Figure 28).

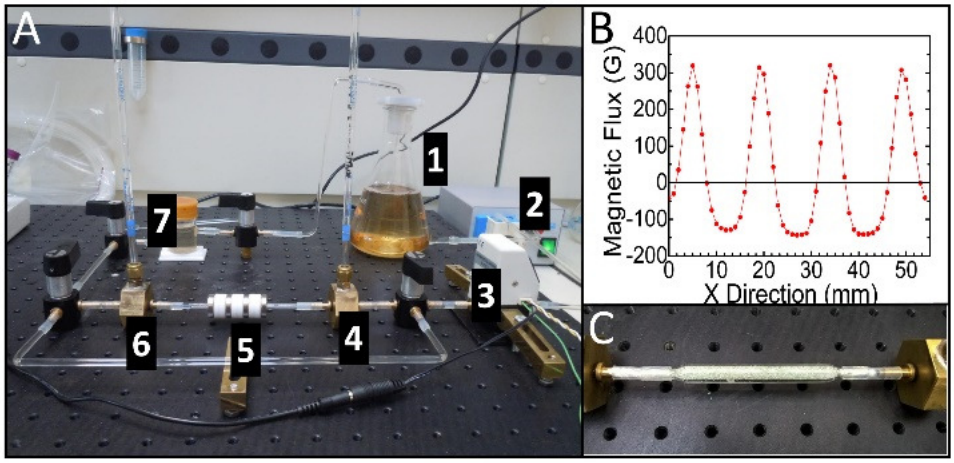

Figure 28. Dynamic flow circuit (A) with (1) accumulation vessel, (2) peristaltic pump, (3) digital flowmeter, (4) and (6) in-house built differential pressure sensors, (5) magnetic accumulation system and (7) sampling holder; magnetic flux generated inside the capture station (B) and capillary vessel for accumulation (C).

This circuit was constructed using glass capillary tube with an inner diameter of 4 mm and an outer diameter of 6 mm, a mini peristaltic pump (VELP Scientific SP311) able to produce flow rates in the 5–125 mL/min flux range, a digital fluxmeter (Omega FLR1000 series) to accurately measure the flow rate, and a differential pressure sensor built in-house to monitor the pressure drop at the end of the accumulation vessel. A configuration of four NdFeB ring permanent magnets (Magnetic Flux $\boldsymbol{B}$ = 1.27 Tesla), with inner diameter of 4 mm and outer diameter of 20 mm, separated by non-magnetic polymeric rings, was used to produce the magnetic field. Capture of micelles by the permanent magnet configuration was studied by monitoring the variation in Fe (SPIONs) content in the fluid as a function of time. For this purpose, during each 8-hour experiment, fluid samples were sequentially collected at fixed times and analysed by Inductively Coupled Plasma Atomic Emission Spectroscopy (ICP-AES).

In an accumulation system like this one, a magnetic nanoparticle, in a dynamic fluid with a fixed flow rate, under a static magnetic field is affected by an attractive magnetic force defined as

$$\boldsymbol{F_M = V_{NP} \cdot \chi_{NP} \cdot H(x) \cdot \left(\frac{\partial H}{\partial z}\right)_x}$$

where $\boldsymbol{V_{NP}}$ is the volume of the NP, $\boldsymbol{\chi_{NP}}$ is the magnetic susceptibility (correlated with the magnetization) of the NP, $\boldsymbol{H(x)}$ is the magnetic field *at* $\boldsymbol{x}$ distance from the magnet and $\boldsymbol{(\partial H/\partial z)_x}$ is the gradient of the magnetic field in the flow direction. From this point of view, it is evident that for a large magnetic force acting on a NP, a great value of the product $\boldsymbol{H(x)\cdot(\partial H/\partial z)_x}$ is required. Since the flow is perpendicular to the magnetic force, the flow rate will interfere with the attractive force of the magnet, *i. e.* higher flow rates will correspond to reduced number of magnetic nanocarriers captured by the magnetic field.

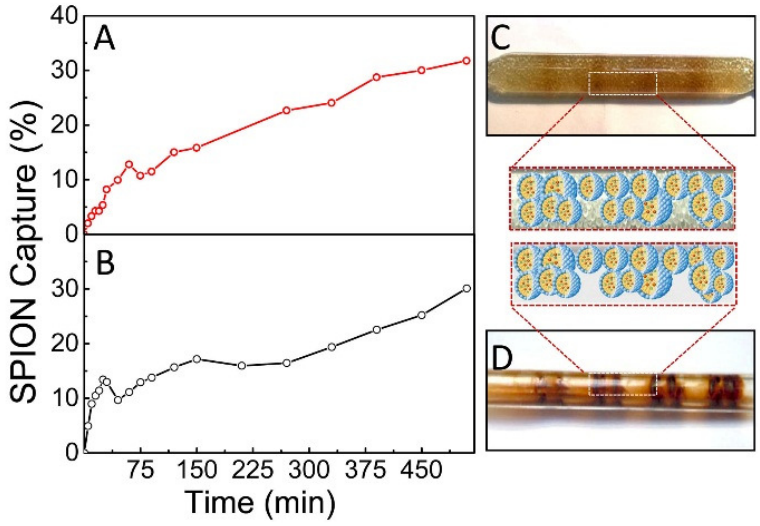

Figure 29. Percent capture of SPION/Micelles in the capillary flow model (A) and in an organic tissue simulation (B). Picture of glass capillary filled with glass spheres (C) and of glass empty capillary (D) along with their corresponding schematic sketch after circulation of the solution containing SPION/Micelles and removal of the NdFeB ring magnets.

Therefore, a magnetic configuration formed by four NdFeB ring permanent magnets with inner diameter of 4 mm and outer diameter of 20 mm separated by non-magnetic polymeric rings was adopted. This configuration allows to increase the number of capture zones inside the capillary glass inserted in the rings, *i.e.* the number of zones where the $\boldsymbol{H(x)\cdot(\partial H/\partial z)_x}$ product is maximum.

The SPION/Micelles were dispersed in physiological solution at pH 7.4 to a concentration of 80 mg/L. To test the speed capture of the adopted configuration of NdFeB ring magnets, two different flow rates, namely 100 and 50 mL/min, were used for the circulation of the solution in the capillary flow model. After a time span of eight hours, about 28% of magnetic micelles capture was observed for the 50 mL/min flow rate by means of ICP-AES analyses (Figure 29B). This value slightly decreases to 23% at the higher flow rate of 100 mL/min, as expected (not reported here). The employed *in vitro* model clearly only mimics the most basic features of blood vessels since there are numerous additional factors that could influence magnetic targeting, such as the mechanical and surface properties of the blood vessel wall. Therefore, since the *in vivo* flow of micelles in liver should be surely affected by many obstacles in the form of cells and extracellular matrix components, a secondary, larger, glass tube (8 mm inner diameter) completely filled with glass spheres with diameters ranging from 0.8 up to 1 mm (void fraction around 0.5) was used to simulate an organic tissue (Figure 29C). A flow rate of 50 mL/min, the best one for our dynamic configuration in these conditions, and a similar configuration of four NdFeB ring permanent magnets was used for the micelles dynamic circulation. In this case (Figure 29A), after eight hours accumulation time span, a percent capture of 32 % has been detected from the ICP-AES analyses. The recorded increase of percent capture can reasonably be related to the increased friction of the PEG-micelles with the surface of the obstacles (glass spheres) that affects the flow rate inside the accumulation vessel and promote the magnetic capture. These experiments highlighted the effect of the flow rate on the amount of micelles blocked by the permanent magnets configuration and the increase of percent capture of micelles loaded with SPIONs in a more dense system due to physical adsorption inside in a more realistic “simulated” organic tissue.

3.1.3 Solid Lipid Nanoparticles (SLNs)

Another type of drug delivery system has been designed. Solid lipid nanoparticles embedded with SPIONs and Sorafenib were similarly prepared to nanoformulations of micelles as reported in Figure 30. This approach benefits from the hydrophobic nature of the nanoparticle surface, characterized by almost spherical morphology and a diameter of 8.8 ± 1.5 nm, and at the same time overcomes the very low solubility of the drug in water.

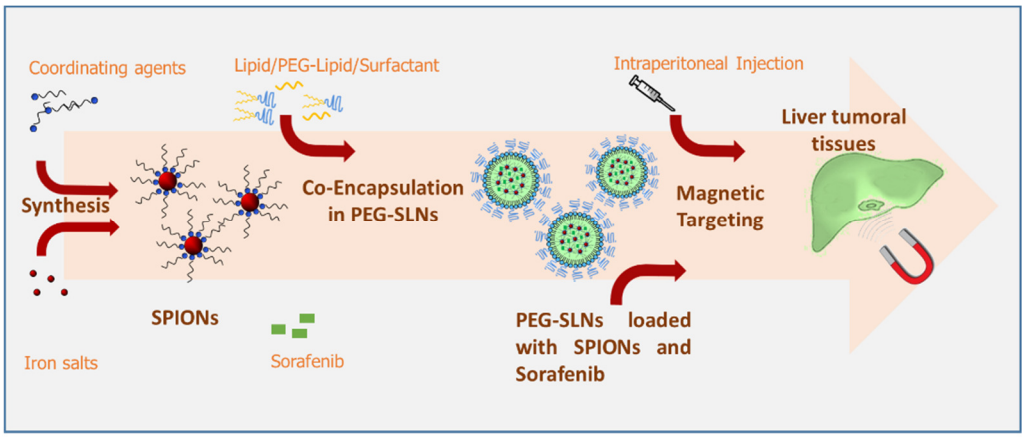

Figura 30. SLNs preparation scheme.

Room temperature SQUID measurements (Figure 31) allowed to evaluate saturation magnetization and calculate SPIONs amount embedded inside SLNs.

The name of the samples represents the amount of nanoparticles suspension added to the solution during the synthesis of solid lipid nanoaperticles, *i.e.* SLN160 means 160 µL of SPIONs.

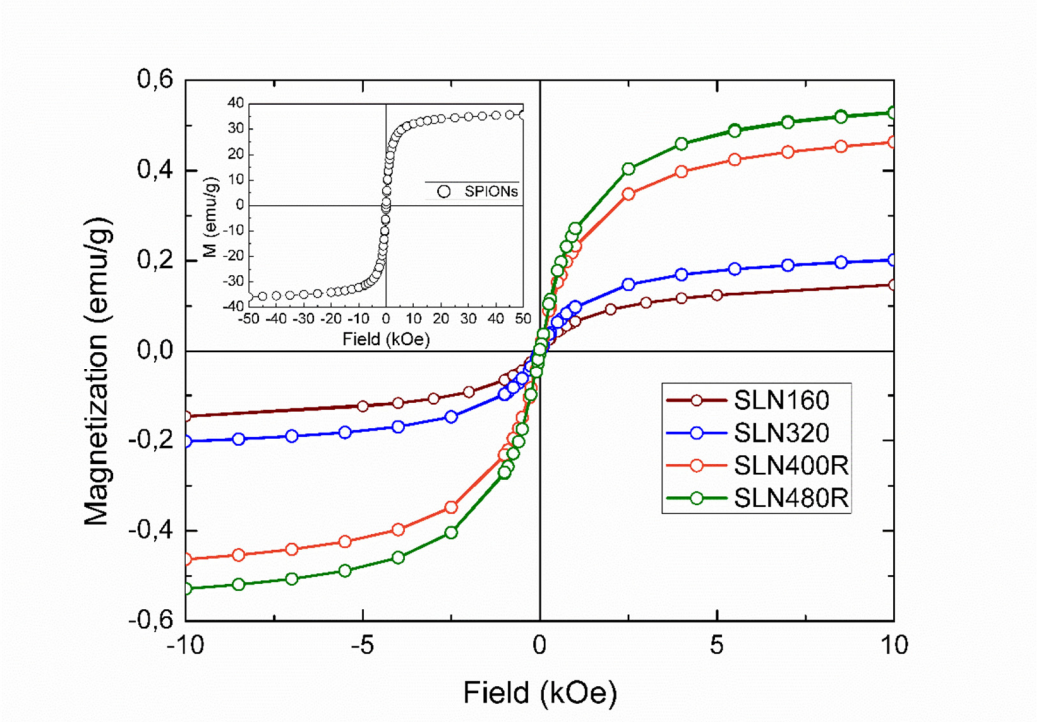

Figure 31. RT hysteresis cycles of SLNs samples with different amount of SPIONs. Inset: SPIONs hysteresis cycle.

As studied for micelles, accumulation tests of SLNs through a circuit and an external magnetic field simulating blood circulation under *in vivo* therapy conditions (mouse liver), were performed.

Once the best conditions have been achieved, the SLNs accumulation tests were performed. SLNs solution, approximately 100 mg /L in water mQ, circulated in the circuit for a total time of 8 hours, reducing to 4 hours for the next experiments. At fixed intervals, closer to the first 2 hours, samplings (about 3 ml) were analyzed by ICP-AES.

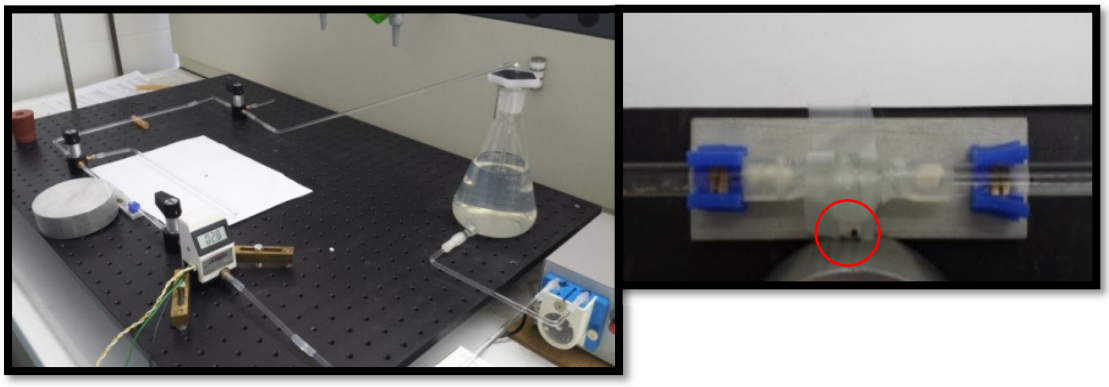

Figure 32. Pictures of the circuit and detail of the capture station (highlighted magnets).

The flux was adjusted at about 3 ml/min to approximate blood pressure in mouse liver. Furthermore, a different and smaller capture station, from the one used in micelles accumulation experiments, was employed (to mimic the mouse liver volume). Moreover, two types of magnets (maximum volume 2x3x3 mm^3) have been tested: a) two NdFeB cylindrical magnets ($\boldsymbol{B} \approx 1.3$ T) and b) one SmCo parallelepiped magnet ($\boldsymbol{B} \approx 1.1$ T), both located along the flow direction as shown in Figure 28.
In the case of NdFeB magnets, maximum SLNs accumulation reached 17 % in about 1.30 h from the beginning of the experiment (Figure 29); in the second case, results from ICP-AES analysis provided no magnetic capture of SLNs.
This result could be ascribed to the different type of magnet used: in the first case, NdFeB magnets are characterized by a higher magnetic flux (B) than SmCo magnet, that is not able to capture and accumulate SLNs with respect to the circuit flow.

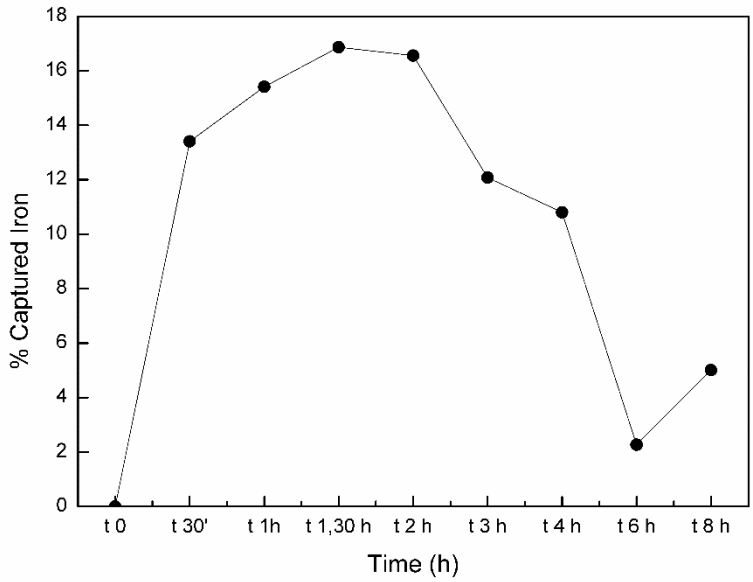

Figure 33. Percent capture of SLNs versus time for accumulation with NdFeB magnets.

3.2 Core-shell and multi-shell ferrite nanoparticles for hyperthermia studies

The last investigated biomedical application concerns magnetic hyperthermia. During the research activity spent at Norwegian University of Science and Technology (NTNU) in Trondheim (Norway), I worked on the preparation of magnetic ferrite nanoparticles. The final task of this project was the synthesis of core-shell and multi-shell ferrite NPs with enhanced magnetic properties.
Once extensively characterized, the *heating efficiency* (SLP) of few samples has been evaluated in hyperthermia preliminary laboratory tests carried out by a research group working at the University of Milan (Prof. A. Lascialfari).

Ferrite nanoparticles, generally indicated as MFe_2O_4, where M is a bivalent cation as Manganese, Iron, Cobalt, Nickel, etc., have been extensively studied during last decades for their good magnetic properties and their easy syntheses through numerous procedures.
The work was mainly focused on the synthesis of Cobalt and Nickel ferrite NPs and their growth into core-shell (CS) or multi-shell layers of *hard* (Co) and *soft* (Ni) structures.
Moreover, two types of configuration have been prepared: a "conventional" structure in which the *hard* core ($CoFe_2O_4$) is coated with a *soft* shell ($NiFe_2O_4$) and an "inverse" structure in which the soft core ($NiFe_2O_4$ or Fe_3O_4) is coated with a hard shell ($CoFe_2O_4$).

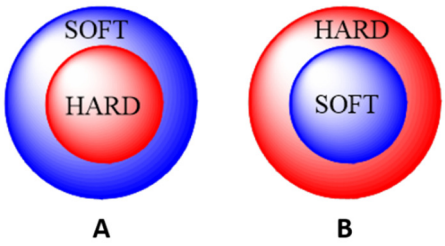

Figure 34. Scheme for the two configurations: conventional (A) and inverse (B).

3.2.1 Conventional and inverse core-shell ferrite NPs

3.2.1.1 Synthesis

Two steps synthesis is required to obtain core-shell NPs: from the first synthesis, the core NPs are formed, then they undergo a second process to grow the shell on them.
Both methods followed a high temperature decomposition of the precursors salts in presence of surfactants to prevent excessive agglomeration between the nanoparticles.
A scheme for the synthesis of the core NPs ($CoFe_2O_4$) is hereafter reported.

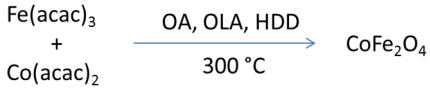

Figure 35. Scheme of the synthesis of $CoFe_2O_4$ NPs.

The synthesis for $CoFe_2O_4$ NPs is here described. In a typical procedure, $Co(acac)_2$ and $Fe(acac)_3$ in molar ratio 1:2 are placed in a two-neck round bottom flask (100 ml) with 20 ml BE. To this solution, 6 mmol of OA, 6 mmol of OLA and 10 mmol of HDD are added. The solution is mixed under Nitrogen flux and undergoes a heating process with a first step at 200 °C (heating rate 5 °C/min) kept for 2h and a second step up to 300 °C (heating rate 5 °C/min) kept for 1h.[92] After cooling down to room temperature, the sample is purified from excess reactants with numerous washings in ethanol in centrifuge at 4000 rpm for 10 minutes each.

Once the core is formed and purified, another synthetic step is required to obtain the shell. In a typical procedure, around 20 mg of core NPs are placed in a two-neck round bottom flask (100 ml) with 5 ml of BE to create a homogeneous dispersion. Then, depending on the case of conventional or inverse core-shell NPs, a suitable amount (0.33 mmol) of $Ni(acac)_2$ or $Co(acac)_2$, respectively, is added. In both cases the correct amount of $Fe(acac)_3$, 0.67 mmol, is also added. Finally, 15 ml of BE and 1.2 ml of OA are added and left to mix.

After a vacuum cycle to eliminate oxygen from the reaction flask, the reaction proceeds under Argon for 30 minutes at 290 °C (heating rate 5 °C/min). After cooling down to room temperature, the sample is magnetically washed overnight in toluene and isopropanol (1:10 V/V approximately).

3.2.1.2 Characterization of conventional CS NPs

The conventional CS1 system is based on a $CoFe_2O_4$ core (SEEDS1) and a $NiFe_2O_4$ shell. In figure 36, STEM images of the core and the CS NPs are reported.

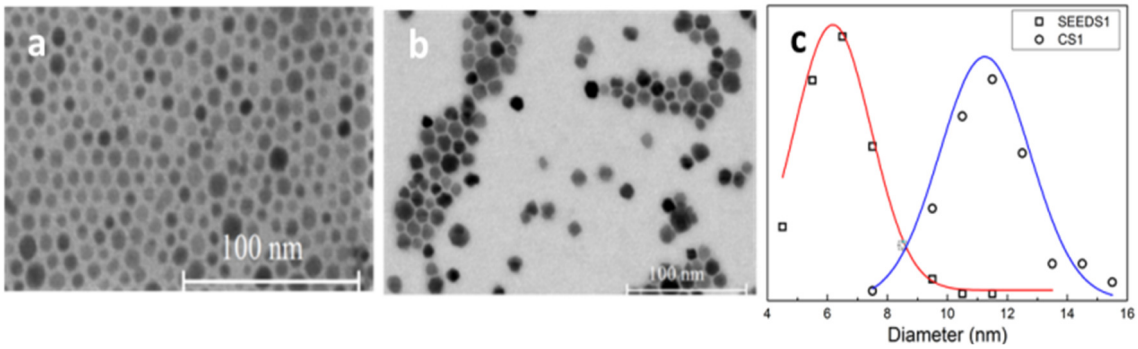

Figure 36. STEM images of core (a) and CS NPs (b). Size distributions of the systems are also reported (c).

The spherical morphology of the core became more irregular after the growth of the ferrite shell on its surface. Obviously, also the dimensions of the NPs changed, varying from 6.2 ± 1.9 nm for the core to 11.2 ± 2.3 nm for the CS1, indicating a shell thickness of about 2.5 nm.

Statistic distributions were obtained elaborating STEM images with ImageJ software on more than 100 particles.

The NPs have been extensively characterized by different techniques in order to evaluate the core-shell nature of the system.

XRD analysis

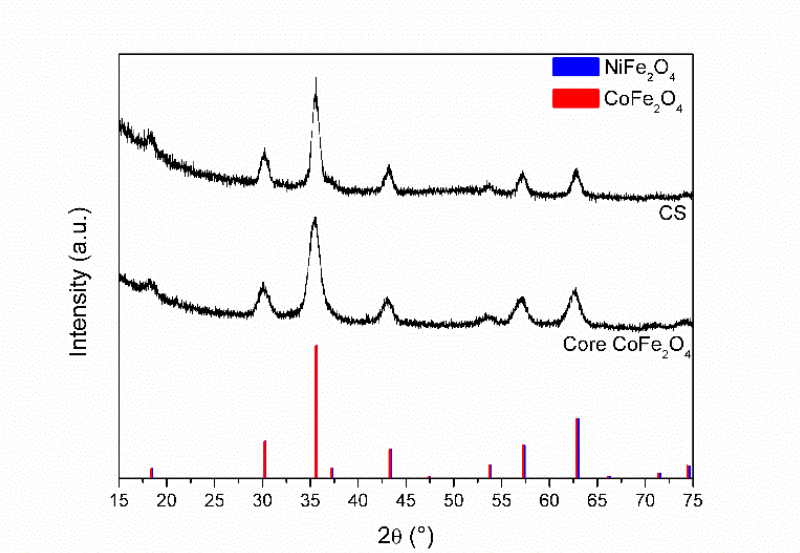

Figure 37. XRD patterns for experimental samples, core and CS; $CoFe_2O_4$ and $NiFe_2O_4$ reference patterns from Pearson's Crystal Data are shown as red and blue lines respectively.

XRD analyses confirmed the spinel crystalline structure for both core NPs and core-shell NPs, but didn't allow to completely evaluate the core-shell nature of the NPs due to the quite identical XRD diffractograms of the two components.

Magnetic measurements

In Figure 38, the hysteresis loops recorded at 5K of the core and core-shell nanoparticles (CS1) are reported. A comparable value of the saturation magnetization, a slightly different value of remanence while a relative high difference in the value of coercive field can be observed (see Table 3.2).
The shape of hysteresis cycle of the CS1 NPs suggests a strong coupling between the hard core and the soft shell. Moreover, also the decrease of the coercive field in the core-shell system confirms this hypothesis.

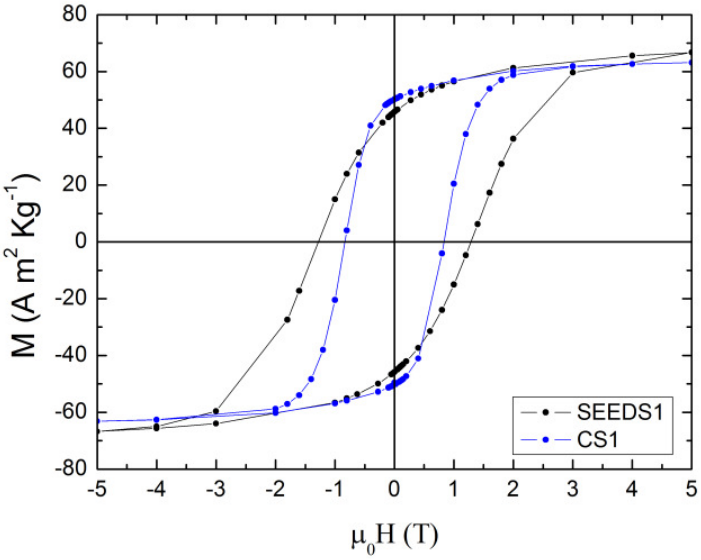

Figure 38. Hysteresis cycles recorded at 5 K for seeds1 and CS1.

Magnetic parameters	Core	CS1
$M_{@25Oe}$ [A m^2 Kg^{-1}]	67 ± 6.7	63 ± 6.3
Remanence [A m^2 Kg^{-1}]	46 ± 4.6	50 ± 5
$\mu_0 \cdot H_c$ [T]	1.3 ± 0.1	0.8 ± 0.08

Table 3. 5K magnetic parameters of the core and core-shell nanoparticles.

In Figure 39, the ZFC-FC curves performed at $\mu_0 H = 2.5 \times 10^{-3}$ T for both core and core-shell samples are presented. In $CoFe_2O_4$ NPs, a broad maximum in the ZFC curve around 250 K is observed, while no maximum in the ZFC curve of CS NPs is detected up to 300 K.

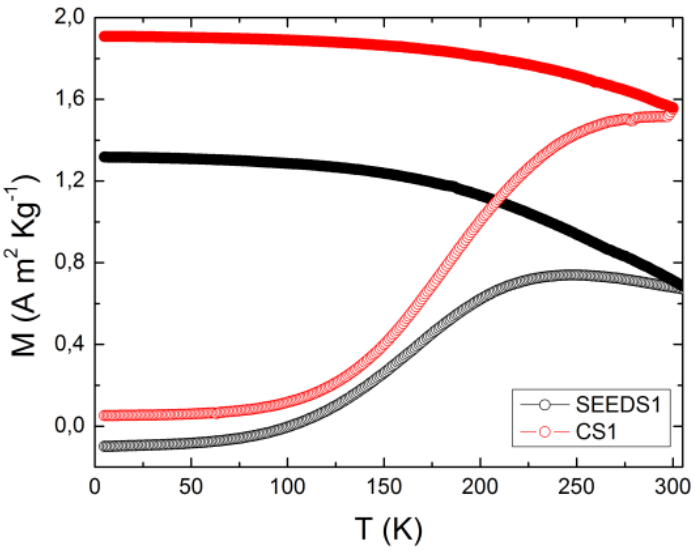

Figure 39. ZFC-FC curves, performed at 25 Oe, for seeds1 (black line) and CS1 (red line).

3.2.1.3 Characterization of Inverse CS

The inverse system was composed by a $NiFe_2O_4$ core and a $CoFe_2O_4$ shell. In figure 40, STEM images of the core (SEEDS2) and the core-shell (CS2) are reported.
As occurred in the conventional system, the inverse CS NPs present an increment in dimensions from 7.9 ± 3.1 nm to 12.1 ± 2.3 nm. The growth of the shell brings to a rough and irregular surface.

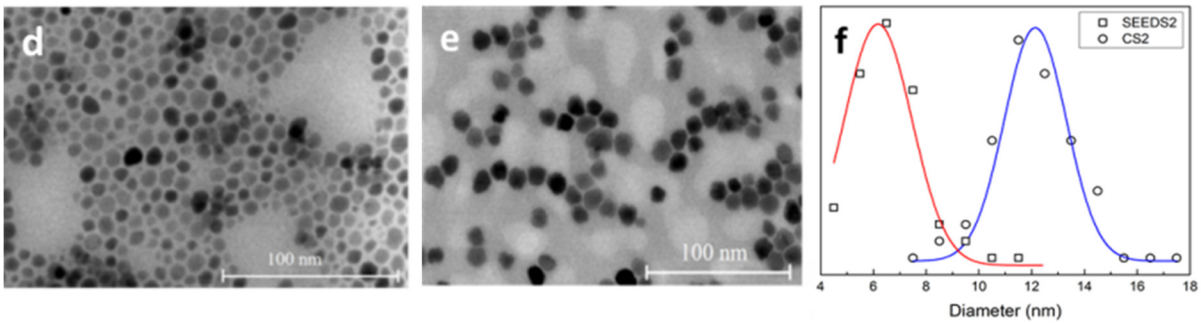

Figure 40. STEM images of core (d) and CS (e). Size distributions of the systems are also reported (f).

Further analyses have been carried out to prove core-shell nature. In particular, EDS profile is able to recognize the elements (Ni, Co and Fe) and allows a first evaluation of the distribution of the elements in the NPs, as reported in Figure 41.

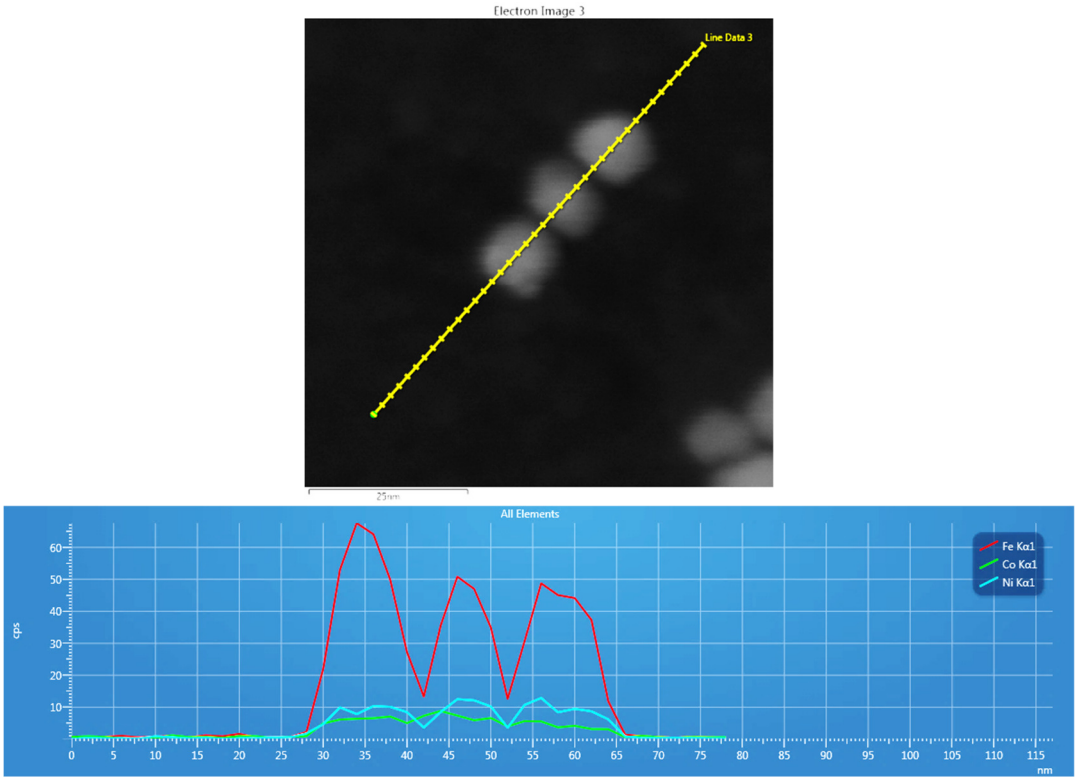

Figure 41. TEM images of the CS NPs and related EDS spectrum.

It can be noted that there is not a clear confirmation of the core-shell structure; indeed, only Iron is easily detectable as external element of the NPs.

Magnetic measurements

SEEDS2 NPs hysteresis cycle, performed at 5 K, has the fingerprint of a very soft material with a relatively high saturation magnetization and very low coercive field (black curve). The growth of a shell of Cobalt ferrite on the surface of core has the effect to increase the hard properties of the material due to the high difference in the first order magnetocrystalline bulk anisotropy constants between $NiFe_2O_4$ ($\boldsymbol{K_u} \sim 4 \times 10^4$ erg/cm^3) and $CoFe_2O_4$ phase ($\boldsymbol{K_u} \sim 4 \times 10^6$ erg/cm^3)[93].

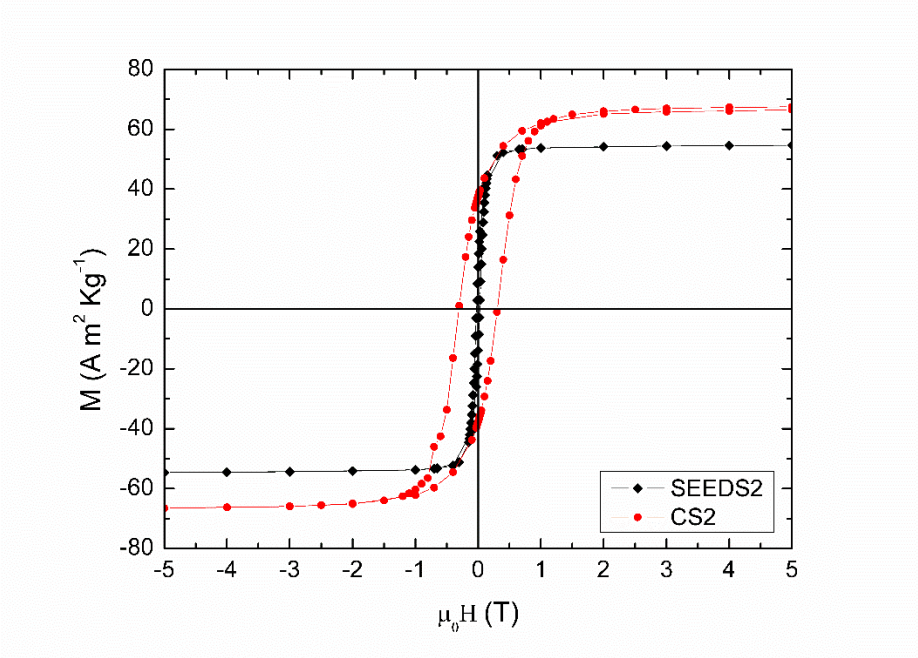

Figure 42. Hysteresis cycles measured at 5 K of Core and CS NPs in the inverse configuration.

The ZFC-FC curves, performed at $\mu_0 H = 2.5 \times 10^{-3}$ T, (Figure 43) indicate, for Nickel ferrite NPs, a low blocking temperature with narrow size distribution. In fact, the difference between the blocking temperature and $\boldsymbol{T_{irr}}$, *i.e.* the temperature at which the irreversibility between the ZFC and FC curves begins, is very small.

The growth of the cobalt ferrite shell has the effect to strongly increase the value of Tmax.

It is known that blocking temperature $\boldsymbol{T_b}$ can be obtained using different methods: a first rough evaluation is from the maximum of the ZFC curve while a second more correct approach is a mathematical analysis using a model suggested by Golubenko et al [94]. The results of both estimates are reported for SEEDS2 and CS2 in table 4.

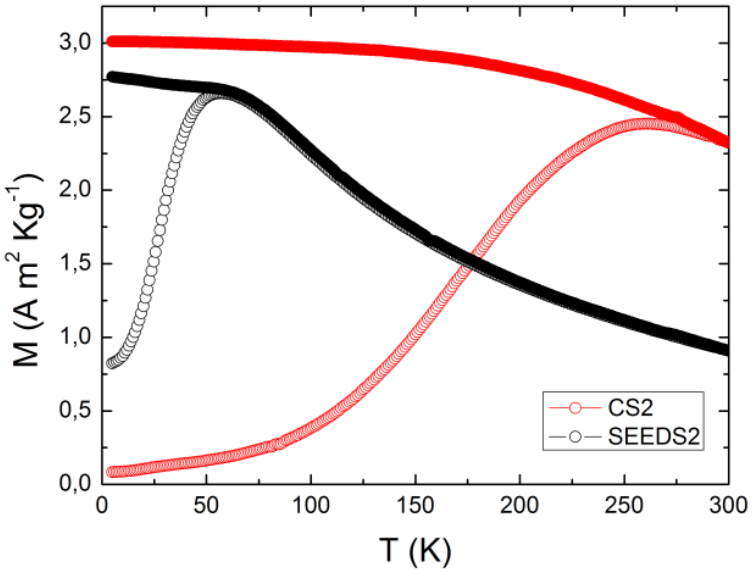

Figure 43. ZFC-FC curves for core (black line) and CS2 (red line).

Magnetic parameters	**SEEDS2**	**CS2**
M_s [A·m^2/kg]	54.6 ± 5.5	67 ± 6.7
Remanence [A·m^2/kg]	13.9 ± 1.4	37.6 ± 3.8
$\mu_0 \cdot H_c$ [T]	0.02 ± 0.002	0.31 ± 0.03
T_b (from ZFC max) [K]	57 ± 5.7	261 ± 26
T_b from Golubenko model[94] [K]	51.4 ± 5.1	265 ± 26

Table 4. Magnetic parameters and characteristic temperatures of the core and core-shell nanoparticles. The magnetic data are taken at 5 K.

3.2.2 Multi-shell Nanoparticles

As the core-shell nanostructures, multi-shell NPs have been investigated. The preparation followed the procedures already described for core-shell NPs (Par. 3.2.1.1.); the core is obtained through a two heating steps (2h at 200 °C + 1h 300 °C) while the shells are formed through one step (30 min. at 290 °C).

3.2.2.1 Conventional multi-shell NPs

Conventional multi-shell NPs are based on a $CoFe_2O_4$ core coated with three layers of $NiFe_2O_4$. The growth of the shells brings to an increase in dimensions (see Table 5) and to a more irregular shape than the spherical core NPs.

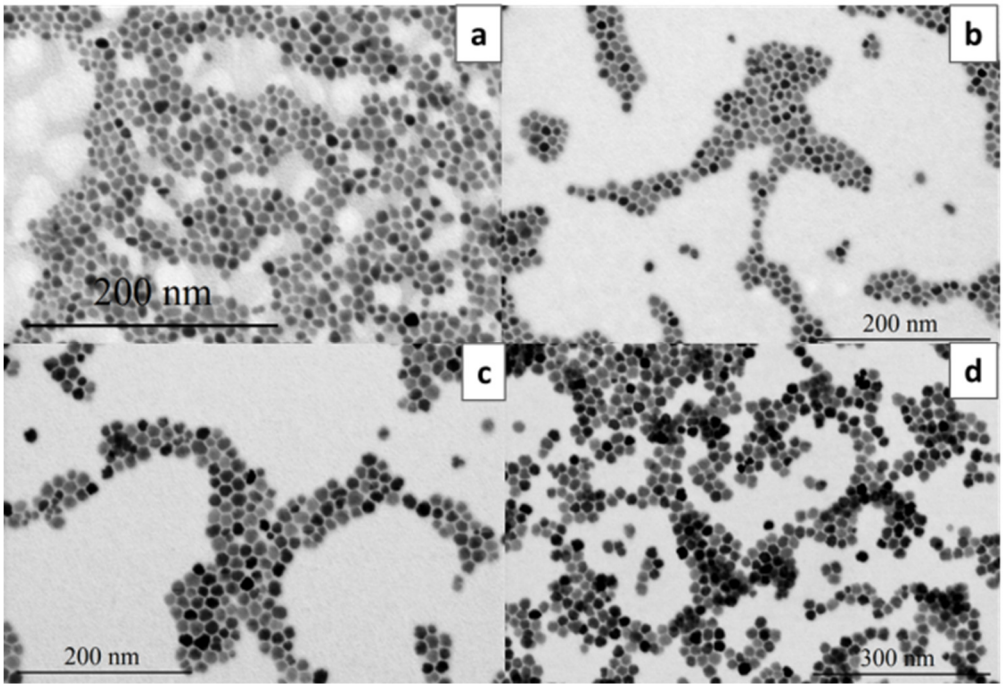

Figure 44. STEM images of core (a), one shell (b), two shells (c) and three shells (d).

Sample	Size (nm)	Shell thickness (nm)
CORE	8.6 ± 2.1	0
1° shell	10.0 ± 1.8	0.7
2° shell	15.1 ± 2.4	3.25
3° shell	19.0 ± 1.9	5.25

Table 5. Dimensions of the NPs from core to multi-shell.

It is noteworthy that the increase is adjusted to an average value of 4 nm for 2° and 3° shells, as happened for CS NPs, but in this case the formation of the first shell brings to a maximum increase of 1.4 nm (0.7 nm shell thickness).
The difference in the shell thickness between the first and the following ones can be related to a different kinetics of deposition of the $NiFe_2O_4$ phase. Even if the time of reaction is the same for all the shells, it is possible that the first deposition of $NiFe_2O_4$ on the core $CoFe_2O_4$ presents a slower growth, achieving only a 0.7 nm thickness with respect to about 2 nm of the other shells.

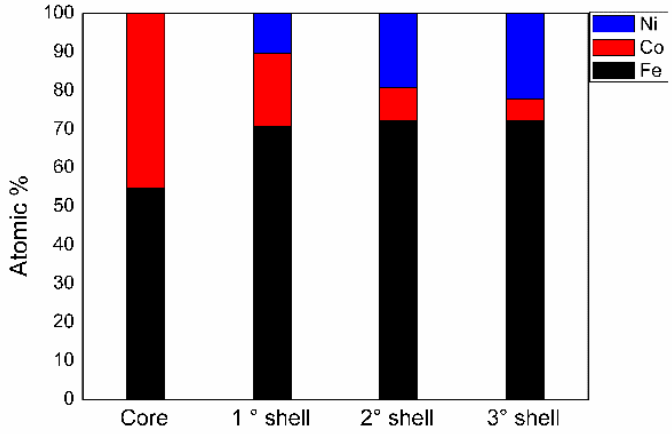

Figure 45. Atomic percentages obtained from EDS analysis.

Sample	% Iron	% Cobalt	% Nickel
CORE	54.68	45.32	0
1 ° shell	70.78	18.83	10.39
2° shell	72.13	8.62	19.25
3° shell	72.36	5.56	22.07

Table 6. Atomic percentages obtained from EDS analysis.

EDS results show that on the increasing number of shells, as expected, Iron and Nickel percentages increase due to the formation of $NiFe_2O_4$ shells, while Cobalt, present only in the core structure, decreases down to 5.56 at% in the three shells system.

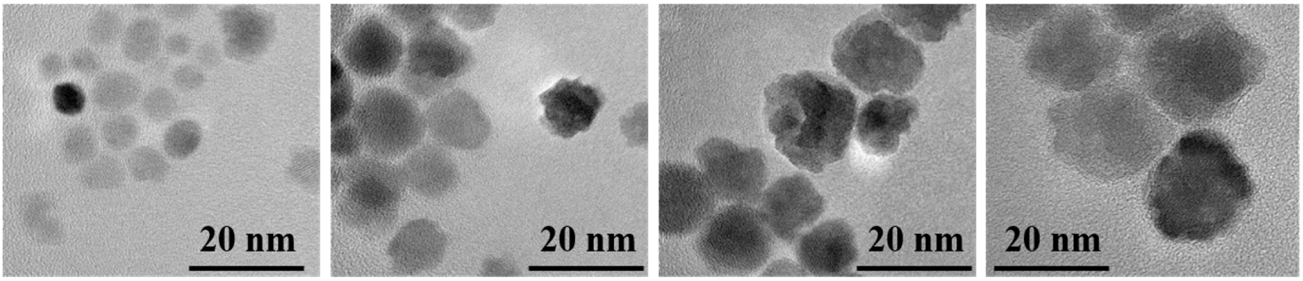

Figure 46. HR-TEM images of the conventional system from left: core, 1° shell, 2° shell and 3° shell NPs.

HR-TEM analyses allows to visualize the shells grown onto the surface of the NPs. In particular, it can be noted that the coating is not uniform but irregular for every deposition step and all over the surface.

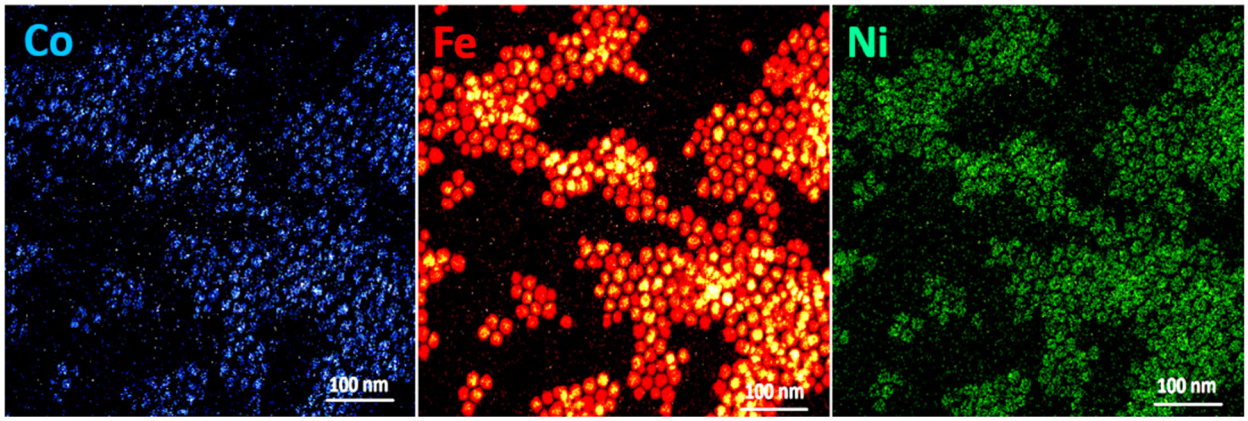

Figure 47. EDXS maps of the 3° shell sample.

EDXS maps of the multi-shell NPs allows to detect the distribution of the elements, namely Co, Iron and Nickel, in the nanoparticles.
In particular, for the 3° shell sample, it can be observed that Cobalt, that should be present only in the core, spread out into the shells, maybe due to the repeated cycles of high temperature synthesis; Iron is detected all over the NPs as base element of ferrites; Nickel, base element of the shells, is detected only in the external part of the NPs and can be visualized as green empty circles (Figure 47).
This analysis is fundamental to prove the multi-shell structure arising from the distribution of the elements in the NPs.

Thermogravimetric analysis

Thermogravimetric behavior, performed using He as carrier gas, is reported in Figure 48. All the decomposition processes observed are completely ascribed to absorbed molecules on the surface of the NPs.
The measurements suggest that a relevant difference in weight loss occurs in the samples from the core to the 3° shell NPs. In fact, the maximum weight loss up to 35 % is detectable for the core NPs (black curve), considering 800 °C as the last decomposition temperature for all the samples. On the increasing number of formed shells, the weight losses decrease, down to 15 % for the 3° shell NPs (blue curve). As observed from HR-TEM images (Figure 46), TGA curves give evidence of the increasing size and thus of the decreasing surface/volume ratio from core to three-shell NPs, indicating a significant less amount of surfactants adsorbed onto the surface of NPs.

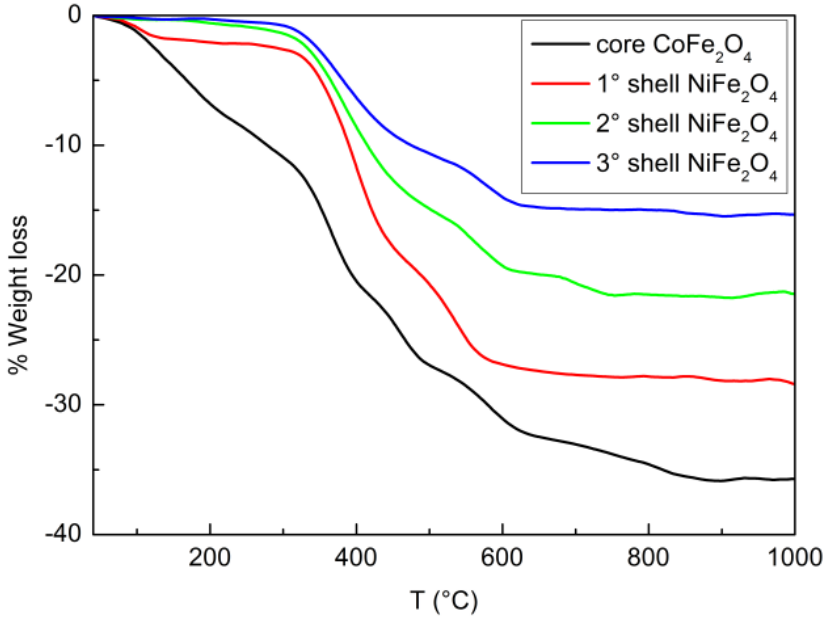

Figure 48. TGA analyses on conventional multi-shell NPs.

Magnetic measurements

Hysteresis cycles were performed at 5 K in the -5 T/+5 T $\mu_0 H$ range.

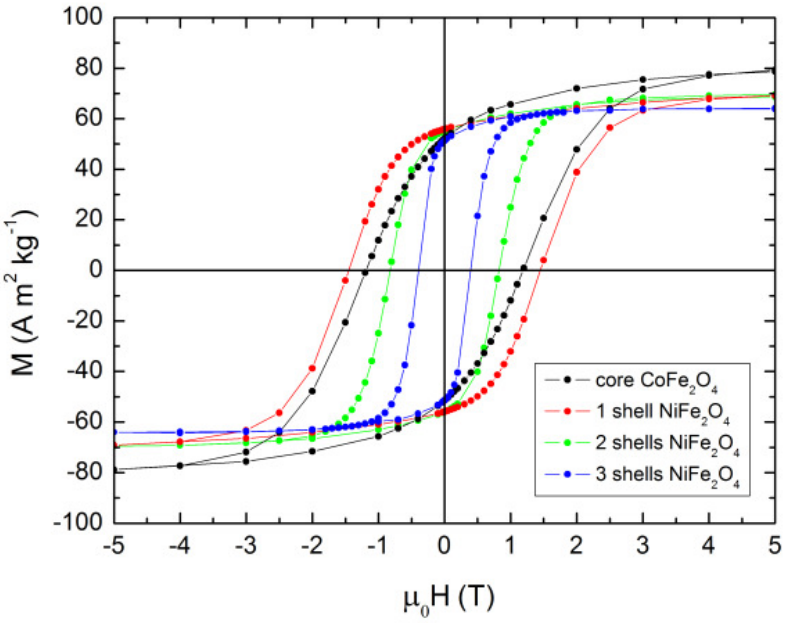

Figure 49. Hysteresis cycles recorded at 5 K for the conventional multi-shell system.

It is worth to note the remarkably large coercivity of 1° shell sample (red curve). As occurred for conventional core-shell NPs, *soft* $NiFe_2O_4$ shell should bring to a decrease in the coercivity of the material; surprisingly, in this case, a higher value of coercivity for the first shell is observed. From STEM size distribution evaluation, the shell thickness for the 1° shell is equal to 0.7 nm. As reported

by Moon et al.,[78] this phenomenon is related to the effect of *exchange coupling* which is particularly intense for very thin shells.

Magnetic parameters	Core	1° shell	2° shell	3° shell
$\mathbf{M_s}$ [A·m^2/kg]	78.7 ± 7.9	69.1 ± 6.9	68.6 ± 6.8	64.1 ± 6.4
$\mathbf{M_r}$ [A·m^2/kg]	52.1 ± 5.2	40.4 ± 4.1	43.3 ± 4.2	43.6 ± 4.3
$\mu_0\mathbf{H_c}$ [T]	1.2 ± 0.1	1.4 ± 0.1	0.8 ± 0.08	0.4 ± 0.04

Table 7. Magnetization and coercivity values.

The temperature dependence of the zero-field cooled (ZFC) and field cooled (FC) magnetization curves present an irreversible behaviour up to the highest measured temperature for all the samples (not reported).

3.2.2.2 Inverse multi-shell NPs

Inverse multi-shell NPs present a $NiFe_2O_4$ core and two $CoFe_2O_4$ shells. HR-TEM and STEM images show the morphology and size of inverse multi-shell system.
As observed for core-shell and conventional multi-shell structures, the growth of the shells is irregular on the surface of the NPs. Dimensions and shell thickness are very similar to conventional multi-shell NPs.

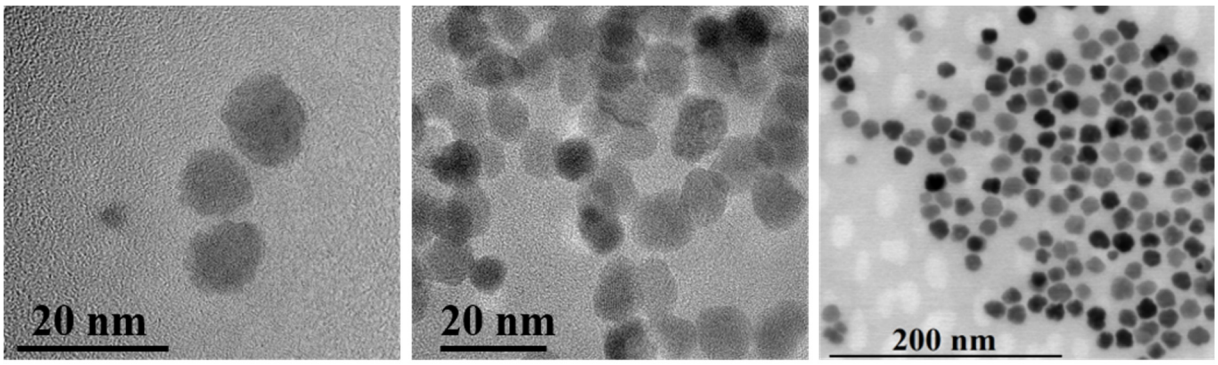

Figure 50. TEM images of core, 1° shell and 2° shell NPs.

	Size (nm)
Core	7.9 ± 3.1
1 ° shell	12.1 ± 2.3
2° shell	17 ± 6.3

Table 8. Size of inverse multi-shell samples.

Magnetic measurements

Hysteresis cycles, presented in Figure 51, give evidence of the growth of one and two layers of *hard* phase ($CoFe_2O_4$) on the surface of *soft* core $NiFe_2O_4$ (black curve), 1° shell (red curve) and 2° shell (blue curve).

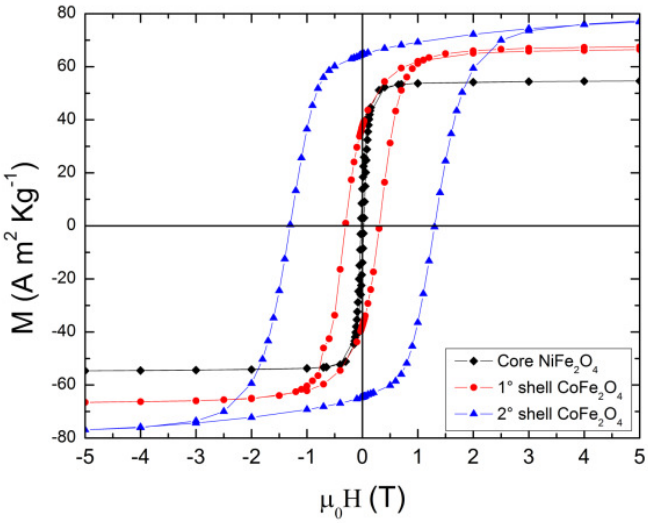

Figure 51. Hysteresis cycles recorded at 5 K for inverse multi-shell system.

In Table 9, magnetization and coercivity values are reported.

Magnetic parameters	**Core**	**1° shell**	**2° shell**
M_s [A·m^2/kg]	55 ± 5.5	67 ± 6.7	76.9 ± 7.8
M_r [A·m^2/kg]	14 ± 1.4	38 ± 3.8	64.6 ± 6.5
$\mu_0 H_c$ [T]	0.02 ± 0.002	0.3 ± 0.03	1.3 ± 0.1

Table 9. Magnetization and coercivity values.

3.2.2.3 Preliminary hyperthermia results

Few ferrite samples, described in current section, have been investigated in hyperthermia experiments to evaluate their heating power (SLP).
Set Parameters for each measurement, made in triplicate, were 110 kHz and 20.3 mT. Samples present an average increase of temperature of 5 °C in 5 minutes. However, some dispersions were not stable during the test and so SLP values are affected by the deposition of nanoparticles in the vial.
Only three samples are stable, marked with an arrow in Figure 48, and the maximum SLP, 7°C in 5 minutes, is generated by sample E, *i.e.* conventional multi-shell NPs with two $NiFe_2O_4$ shells.

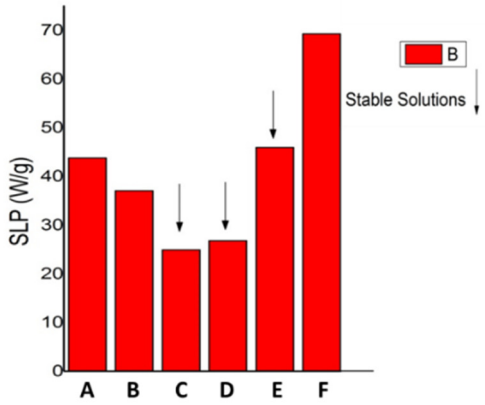

Figure 52. Sample A: inverse core-shell; Sample B: inverse multi-shell; Sample C: core $CoFe_2O_4$; sample D: 1° shell conventional multi-shell; sample E: 2° shell; sample F: 3° shell conventional multi-shell.

The plot in Figure 52 shows that synthesized core-shell and multi-shell samples present moderate SLP values, reaching almost 50 W/g in the most stable nanoparticles (sample E).

4 Environmental Applications

Due to high surface area-to-volume ratio, high and fast extraction capacity and high specific affinity for heavy metal ions adsorption, magnetic nanoparticles have great potential to provide toxic metal capture from aqueous systems.[95] Adsorption procedure combined with magnetic separation makes magnetite a potential candidate, so that the magnetic system and the captured metals can be easily and simply separated, from the aqueous phase, by the application of an external magnetic field. Magnetic nanoparticles as the solid phase adsorbent also possess the surface modification ability due to the presence of hydroxyl groups on the iron oxide nanoparticles surface which provides a versatile synthetic handle allowing the attachment of different functionalities. Whenever certain functional ligands are bounded with these magnetic nanoparticles, these ligands could enhance their capacity and affinity for targeting metals. Recent research has indicated that functionalized magnetic nanoparticles have become widely common, because of the possibility of them to be applied as adsorbents for the removal of heavy metals from contaminated water.

4.1 Static and dynamic removal of Pb (II) ions from waters

Among functional groups, thiol functionalized magnetite was observed to be the most efficient one which forms a strong complex with toxic metals as Pb(II) and Hg(II) species. Couple of investigations have been carried out utilizing thiol-functionalized functionalized adsorbents.[95,96]

4.1.1 Synthesis of thiol functionalized Fe_3O_4 NPs

Magnetite nanoparticles were synthesized through a coprecipitation method of stoichiometric amounts of Iron (II) and Iron (III) from an aqueous solution under basic conditions, as described in Par. 3.1.1.2..[89]

The magnetite NPs functionalization is here described: to a volume of 100 ml of ethanol, a proper volume of magnetite NPs dispersed in aqueous medium (final concentration 0.5 g/l) was added. Then 800 µl of ammonia aqueous solution and 1 ml of MPTMS was added; the reaction proceeded for 24 hours at 50 °C under vigorous mechanical stirring.

The sample was then magnetically washed several times with ethanol and mQ water to reach the final product, *i.e.* Fe_3O_4@MPTMS, and stored in an aqueous medium.

4.1.2 Morphological, chemical and thermogravimetric characterization

The NPs have been characterized by FE-SEM microscopy, FT-IR spectroscopy and ThermoGravimetricAnalyses (TGA).

The morphology of the magnetite nanoparticles after the functionalization was detected by Field Emission Scanning Electron Microscope. In Figure 49, a typical FE-SEM image of the magnetite NPs coated by the thiol derivative MPTMS, together with the EDX analysis, is presented. Even if single particles have relatively small size (20 nm), large agglomerates can be detected all over the sample.

EDX spectrum confirms, through the detection of the characteristic peaks of Sulphur and Silicon, the presence of the organosilane molecule as well as the presence of Iron and Oxygen related to magnetite, while Copper and Carbon are due to the support grid.

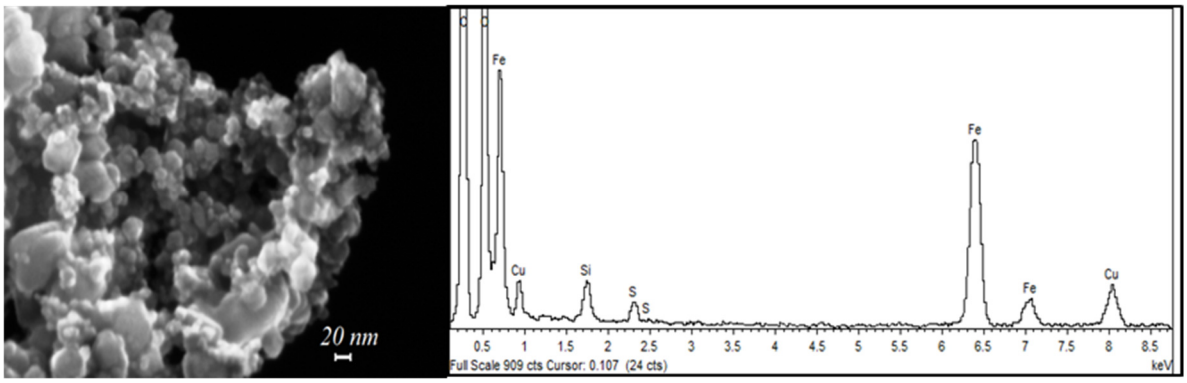

Figure 53. FE-SEM image of Fe_3O_4@MPTMS NPs (left) and the corresponding EDX spectrum (right).

To further confirm the nature of the final product, the dried powders have been investigated by FT-IR measurements. From the spectra reported in Figure 54, peaks around 3000 cm^{-1}, related to C – H stretching deriving from the alkyl chain of MPTMS can be observed in the spectrum of Fe_3O_4@MPTMS.

The broad peak in the spectrum of bare Fe_3O_4 NPs (blue curve) at about 3400 cm^{-1} is due to O – H stretching. On the contrary, the typical very weak peak related to functional S – H group at about 2600 cm^{-1} was weakly observed only in the spectrum of the pure organosilane (enlargement of black curve).

Furthermore, the functionalization causes the appearance of additional barely resolvable peaks in the finger print region. The strong peaks near 1100 and 800 cm^{-1} are due to Si – O – Si and Si – O stretching vibrations, respectively, and related to the condensation between hydroxide groups on magnetite NPs surface and the organosilane molecule.

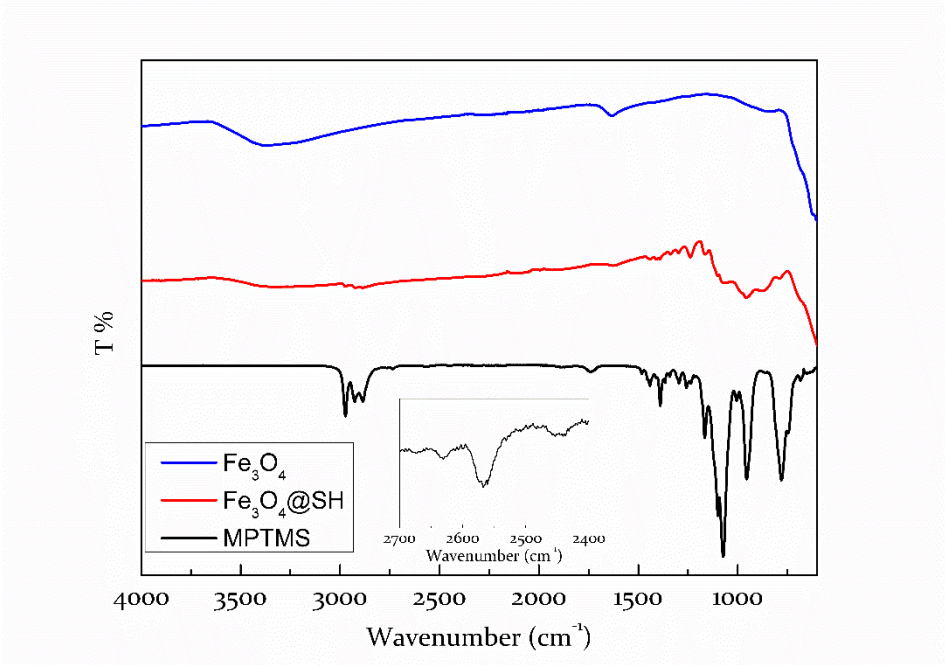

Figure 54. FT-IR spectra; enlargement of SH signal as inset.

The TGA analysis, reported in Figure 55, was used to quantify the amount of organosilane molecule coating the NPs. From the analyses, performed on different Fe_3O_4@MPTMS samples, a total weight

loss of about 8.2% has been detected. In particular, two different weight losses were observed: the first, beginning at low temperature up to 200°C, is due to the release of solvent absorbed onto the nanoparticles surface, while the second one, starting at about 200°C up to 950°C, is due to the organic ligand decomposition. Data present in literature are not exhaustive and not sufficient to hypothesize the real degradation mechanism. The most reasonable hypothesis for the corresponding degradation mechanism consists in the Si – C bond breaking, with the release of the organic chain, while the silane part of the ligand remains attached on the particles surface.

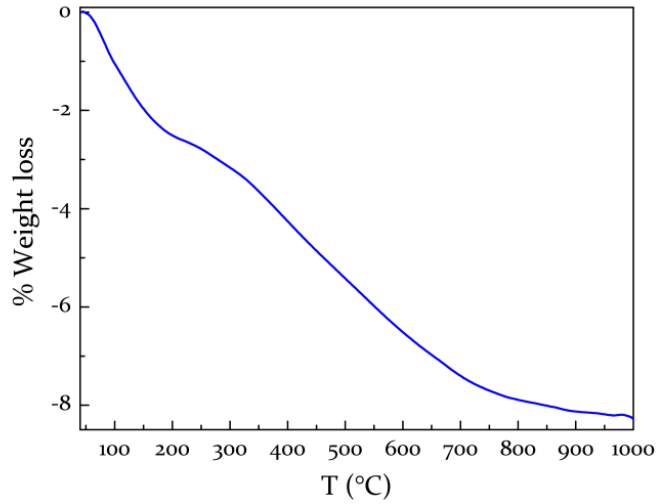

Figure 55. TGA profile of Fe_3O_4@MPTMS.

4.1.3 Capture experiments

After sonication, proper amounts of functionalized Fe_3O_4@MPTMS NPs were dispersed with Milli-Q water in a 50 mL Falcon test tube to obtain samples of different concentrations, ranging from 50 ppm to a maximum of 300 ppm of Iron. Then a fixed volume of Pb^{2+} solution was added to the Falcon to reach the final concentration of 5 ppm. The Falcon tube was then shaken for few minutes and placed in the NdFeB ring magnets configuration to provide the capture from the aqueous medium (Figure 56).

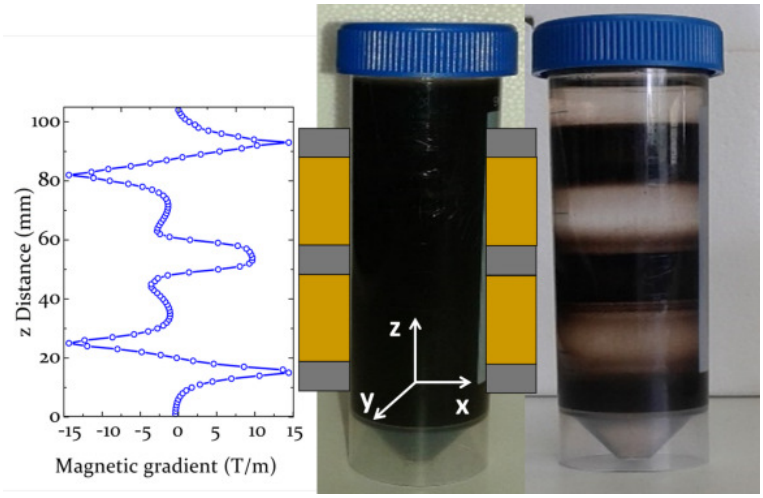

Figure 56. Static capture before and after the application of the external magnets. On the left, the magnetic gradient versus z distance induced by the magnets inside the Falcon tube is presented.

The magnetic gradient was evaluated measuring the magnetic field generated by the magnets every 0.5 mm along the z axis inside the tube by means of a Hall probe connected with a gaussmeter (Lakeshore Cryotronics®).
In a 60 minutes timespan, samplings of 2 ml every 10 minutes were extracted from the Falcon tube for quantitative analyses of Iron and Lead in order to determine the amount of residual NPs and Pb^{2+} ions in solution, respectively.

The six experiments at different concentrations were performed keeping the Pb^{2+} concentration at 5 ppm, to evaluate the optimal condition to obtain the maximum uptake of Pb^{2+} ions from solution. ICP-AES was employed to analyze the solutions, measuring the residual concentration of Lead and Iron in solution. The resulting values were then subtracted to the initial concentrations to obtain the percentage of capture of Iron deriving from Fe_3O_4@MPTMS NPs and percentage uptake of Pb^{2+} bounded to NPs.
The results are reported in Figure 57. Black line represents the Iron content (Fe_3O_4@MPTMS NPs) which was almost identical in each experiment; for this reason, only one curve is reported. It is worth noting the very fast initial capture rate of the NPs; the capture is almost complete after 10 minutes (more than 99%), thus confirming the high efficiency of the magnets configuration adopted. At the same time, the Pb^{2+} ions uptake is also very fast in each experiment: already after 10 minutes, it reaches different constant (plateau) values, which depend from the concentration of Fe_3O_4@MPTMS. The maximum Pb^{2+} uptake value (91%) was obtained with the highest concentration of NPs of 300 ppm (blue curve). Based on these results, subsequent experiments have been carried out using a concentration of 300 ppm Fe_3O_4@MPTMS NPs to ensure the highest heavy metal uptake.

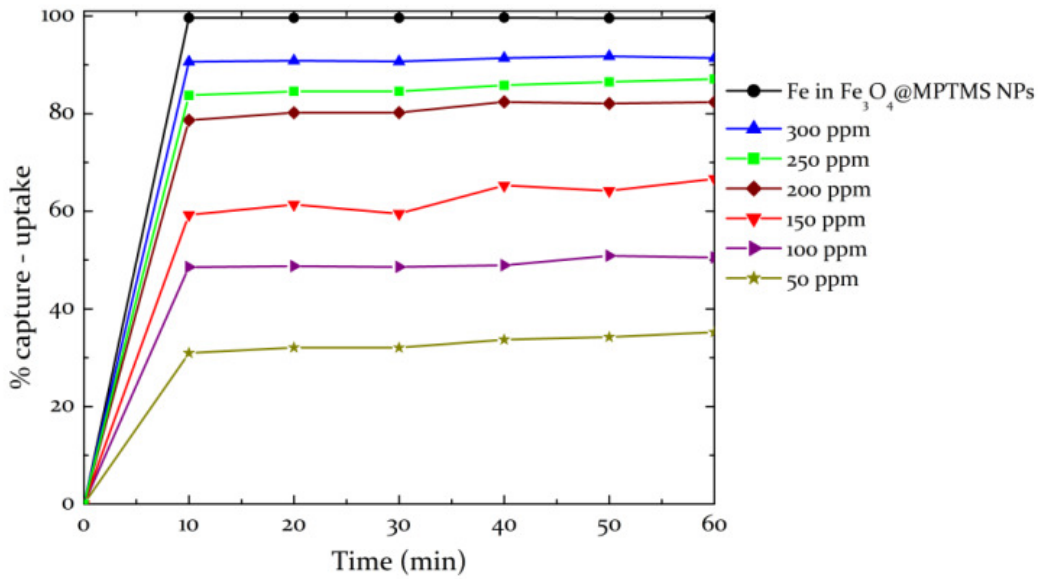

Figure 57. Uptake of Pb(II) ions from solutions by Fe_3O_4@MPTMS nanoparticles. Lines tagged 50 – 300 ppm define the six experiments with Fe_3O_4@MPTMS NPs at different concentration in water solution. Black line tagged Fe in Fe_3O_4@MPTMS NPs defines the NPs capture.

From the data reported in Figure 57, it is evident that the adsorption process of Pb^{2+} ions on Fe_3O_4@MPTMS NPs is strictly related to the amount of NPs and that it is a fast process. In fact, for a fixed NPs concentration, the proper maximum amount of heavy ions is captured after 10 minutes and only a very small increase of captured Pb^{2+} ions are observed between 10 and 60 minutes. The dependence of the 10 minutes % Pb^{2+} capture from NPs concentration, reported in Figure 58, shows a logarithmic trend, giving evidence of a kinetic law with a first order dependence from NPs concentration.

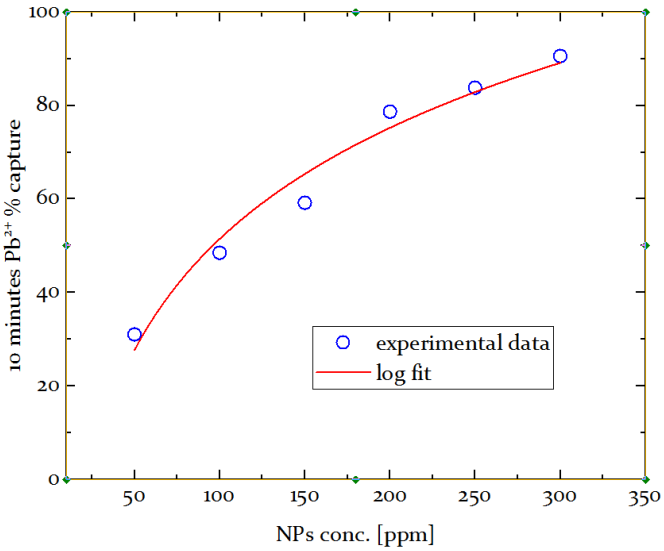

Figure 58. Experimental data (open symbols) of the Pb^{2+} % capture as a function of the NPs concentration and logarithmic fit (red line).

4.1.4 Regeneration and reuse of MNPs

To remove the Pb^{2+} ions from the NPs and reutilize them after the capture experiment, the chelating agent EDTA was employed. The stability constant of the Pb^{2+} EDTA complex[19] presents a pK_f value of 17.7, therefore the recovery of Pb^{2+} ions captured by the NPs, was attained using an EDTA solution (0.02 M) at pH 7.5-8.

After the capture process, the collected Fe_3O_4@MPTMS@Pb NPs were re-dispersed in aqueous solution of EDTA (50 ml) to recovery Pb^{2+} ions. In this step, the Falcon test tube was kept under mechanical shaking for 1 minute, stopped for 4 minutes and followed by magnetic capture for 10 minutes of contact between the test tube and the magnetic configuration. This protocol was repeated other two times to make only one sampling after 45 minutes of interaction with EDTA solution.

The aqueous solution containing Pb^{2+}/EDTA complex was completely removed. The collected NPs were dispersed again in a new Pb^{2+} standard solution (5 ppm) and then the procedure described in Par. 4.1.3. was repeated. After this second step of uptake, fresh EDTA was introduced in the Falcon tube to carry out a second cycle of Pb^{2+} extraction with the same NPs. This procedure was repeated for 5 cycles globally.

Considering that the amount of the NPs is decreased due to the samplings for the ICP-AES analyses, a similar experiment was repeated using the same procedure described above but adding after each cycle an aliquot of Fe_3O_4@MPTMS to restore the initial amount (results not reported).

The uptake data of the two set of experiments were not significantly different, indicating that the small volume, taken after each cycle for the ICP-AES analysis, doesn't affect the Pb^{2+} uptake efficiency. Lead recovery was very good in both set of experiments with a mean value of 91.4 for the first experiment and 81.3 for the second one.
The results of both the uptake and recovery cycles for the first experiment (without the addition of NPs) are shown in Table 10.

Cycle Number	Pb^{2+} uptake	Pb^{2+} recovery
1	85.6	89.0
2	50.1	100.5
3	46.2	90.9
4	46.6	83.4
5	34.4	93.3

Table 10. Percentage of Pb^{2+} Uptake and Recovery.

Regarding the reuse of Fe_3O_4@MPTMS NPs for different cycles it can be observed that, after the first cycle in which the efficiency is higher than 85 %, the uptake drops down to about 50 % for the next three cycles; a new important decrease occurs then during the fifth one.
Considering that the Pb^{2+} recovery is constant in each cycle either restoring the initial amount of Fe_3O_4@MPTMS NPs or not, we can hypothesize that several active sites onto the NPs surface have been deactivated during the recovery steps with EDTA.

Metal ions selectivity

To evaluate the different interaction between Fe_3O_4@MPTMS and metal ions, a selectivity test has been performed. A mix of the four investigated metal ions, Pb (II), Cu (II), Cd (II) and Ag (I), was added to the NPs dispersion and the capture experiment was carried out in the same conditions applied to Pb (II) experiments.

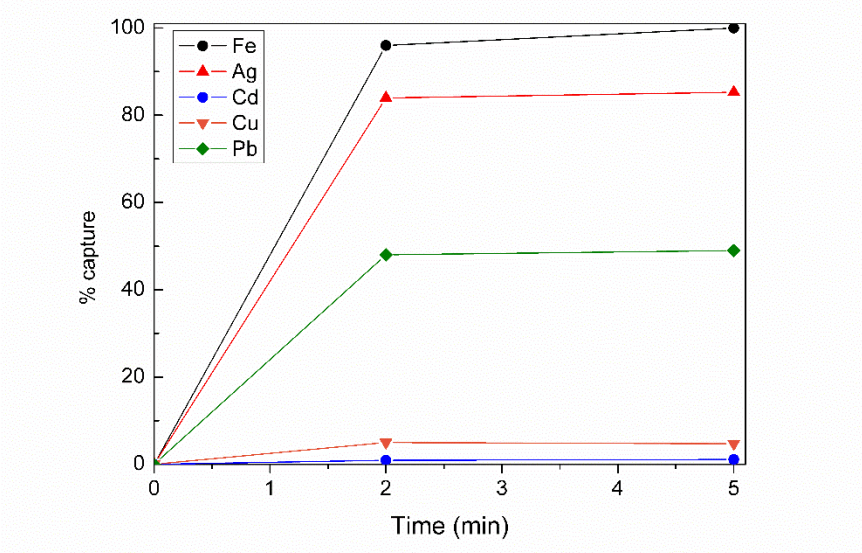

Figure 59. Selectivity for different metal ions.

From this simple test, the different affinity of metals and NPs can be observed. Indeed, Fe_3O_4@MPTMS seems to have the maximum affinity with Ag (I), then Pb (II), and a very low interaction with Cu (II) and Cd(II).

4.1.5 Capture in a dynamic circuit

A dynamic circuit was designed and built to investigate the possibility to treat higher volumes of polluted water. This improvement allows us to increase the volume of the treated liquid from 50 mL up to 1 L (with a 20:1 ratio) preventing the use of larger (and more hazardous) permanent magnets for a static capture.
This circuit, where the pipe line is a glass capillary tube with inner diameter of 4 mm and outer diameter of 6 mm, is composed by a mini peristaltic pump (VELP Scientific SP311) operating in the 150-500 ml/min flow rate and a digital fluxmeter (Omega FLR1000 series) to measure the correct flow rate. A magnetic configuration, formed by five *capture stations,* each one composed by four NdFeB ring permanent magnets (Magnetic Flux B = 1.27 Tesla) with inner diameter of 4 mm and outer diameter of 20 mm separated by non-magnetic polymeric rings, was adopted.

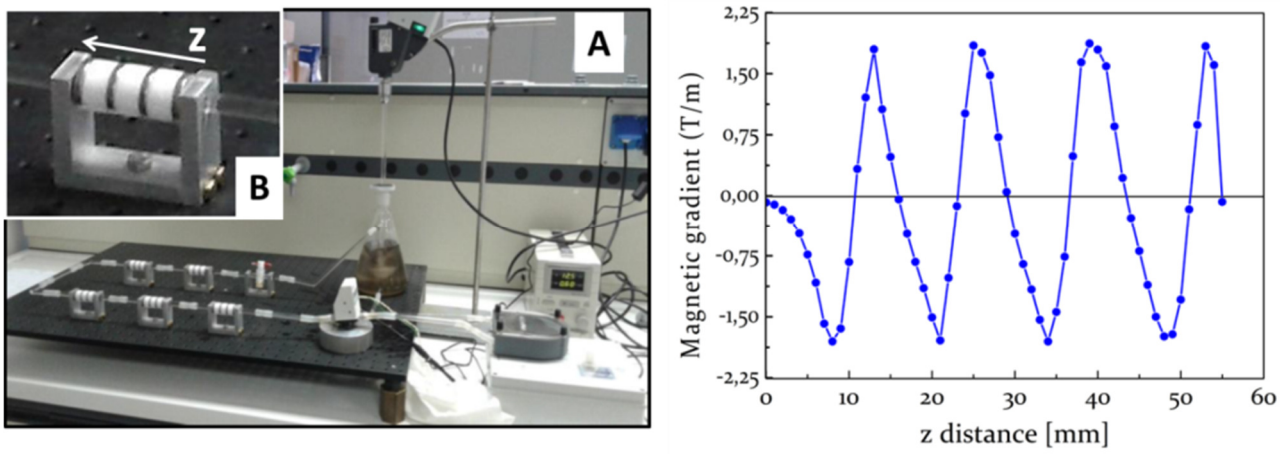

Figure 60. Picture of the dynamic circuit (A), a *capture station* as inset (B) and the related magnetic gradient (right).

The treated polluted volume was equal to 1 L with a Fe_3O_4@MPTMS NPs concentration of 30 ppm and an amount of Pb^{2+} ions equal to 500 µg/l. The flow rate was adjusted to 250 ml/min.
The capture results every fifteen minutes up to one hour, are shown in Table 11.

Time [min]	% captured Iron	% Pb^{2+} recovered by collected NPs
0	0	0
15	71.3	17.2
30	67.2	14.5
60	90.5	20.9

Table 11. Percentage of capture for the dynamic circuit.

It should be pointed out that the system is able to collect more than 90% of magnetic NPs, using a 250 ml/min flow rate, corresponding to a flux speed of 0.5 cm/s, a lower limit for rivers and streams flux speed.
The reduced amount of captured Pb^{2+} ions, is probably due the ionic interaction between the heavy metal ion and the thiol group, which is relatively weak with respect to the flow rate. Since the interaction energy of the HS – heavy metal ion complex is very high for Silver[17], we carried out a preliminary experiment of dynamic capture of Ag^{+} ions in the same experimental conditions already adopted for the Pb^{2+} ions, *i.e.* volume, temperature, NPs and heavy metal ion concentration, flux speed, time. In this case, the capture of Ag^{+} reached 100%.

4.2 Photocatalysis

In this section, research activities regarding environmental applications of nanoparticles, in particular their use as seeds for the preparation of efficient TiO_2 photocatalyst is described.
First, preliminary studies on magnetite nucleated TiO_2 NPs will be discussed; as second topic, a more accurate evaluation of different nanoparticulate seeds mediated synthesis and photocatalysis experiments will be reported.

4.2.1 Enhancement of TiO_2 NPs activity by Fe_3O_4 seeds

In this section, the results obtained for the synthesis of titanium dioxide NPs in presence of magnetite nanoparticles and their use as photocatalysts will be presented. Magnetic NPs have been evaluated as potential magnetic core for Fe_3O_4@TiO_2 hybrid material in order to facilitate the recovery of the catalyst from the polluted solution by applying an external magnetic field.
The attention was focused on the possibility of using, in the titania sol-gel synthesis route, very small amounts of magnetic nanoparticles, exploited as germination seeds affecting the nucleation, formation and morphology of the TiO_2 NPs.
Different syntheses have been carried out, varying the TiO_2/Fe_3O_4 ratio. The photocatalytic performance has been tested in the framework of a standard ISO 10678:2010 protocol, *i.e.* the degradation of MB solution of known concentration. The results showed a strictly correlation between the amount of Fe_3O_4 added during the TiO_2 synthetic process and the observed titania photocatalytic activity; moreover, also other properties, such as surface area and crystallinity, have been widely affected.
Furthermore, a comparison of the photocatalytic activity of our NPs with a commercial product (TiO_2 NPs P25 from Sigma-Aldrich), demonstrated the higher activity possessed by our materials. Consequently, the best material was also tested for the degradation of Ofloxacin (OFL), an important emerging water pollutant, belonging to the class of Fluoroquinolone (FQs) antibiotics.[97]
Synthesized samples had the following TiO_2/Fe_3O_4 ratios: Sample A 500:1; Sample B 1000:1; Sample C 2000:1 and Sample D, where no Fe_3O_4 NPs were added.

4.2.1.1 Chemico-physical characterization

In Figure 61, the X-ray diffraction patterns of samples A, B and C are reported. Samples A and B showed the characteristic peaks of the TiO_2 tetragonal anatase structure, presented as line pattern in the same figure. On the contrary, sample C and D (not reported in the figure) resulted completely amorphous and no identifiable peaks were detected. It is noteworthy that magnetite is well below the detection limit of the XRD technique, due to its very low amount respect to titania. It should be pointed out that sample A resulted more crystalline than sample B: this fact is underlined by the presence, in sample A, of higher intensity peaks and by a diffraction pattern better discernable from the baseline, especially at $2\theta > 60°$.

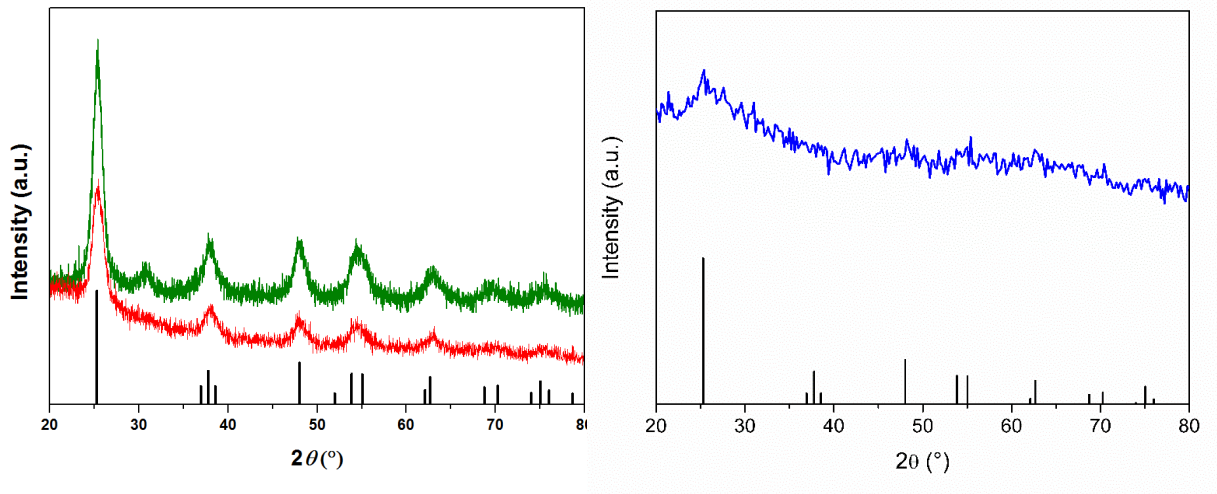

Figure 61. XRD patterns of Samples A (green curve), sample B (red curve) and crystallographic peaks of anatase phase (black line pattern). On the left, XRD pattern of amorphous sample C.

These diffraction data are consistent with the DSC investigations, reported in Figure 62. The thermal behavior of all the samples is characterized by a broad endothermic peak below 100 °C, characteristic of the dehydration caused by a small quantity of water adsorbed. A second exothermic peak is observed at 215 °C for samples A and B and 240 °C for C and D, respectively.

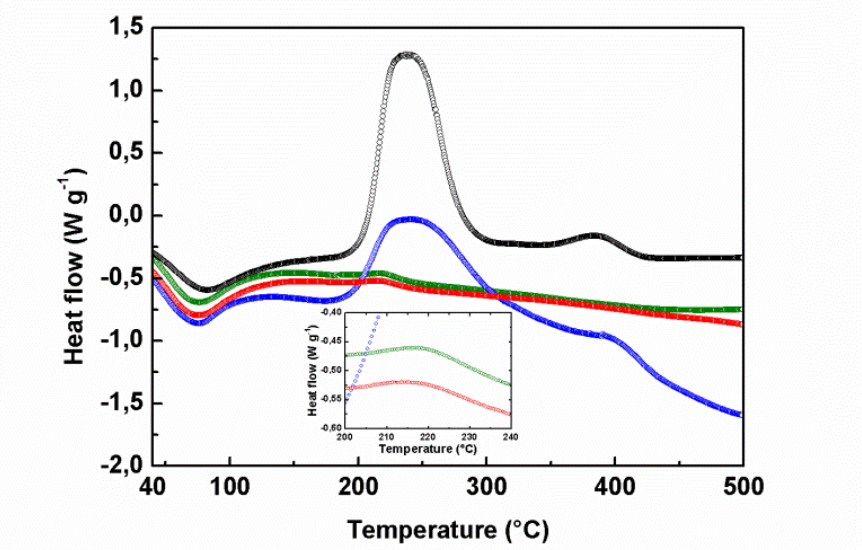

Figure 62. DSC analyses of sample A (green), sample B (red), sample C (blue) and sample D (black). In the inset the peaks at 215°C for samples A and B are enlarged.

In this step, the oxidation of the 2-propanol adsorbed on the surface occurred. The drastic difference in the intensity signals indicates a different amount of solvent that increased from sample A to D. Indeed, this result agree well with the surface area analysis from BET isotherms (Table 12), where the increased value of the surface to mass ratio from A to D, implies an increment of the possibility to adsorb the solvent. Samples A and B had no supplementary signals, demonstrating a complete crystallization already at 150 °C. On the contrary, sample C and D possessed a weak exothermic peak at 385 °C, correlated with the phase transition of the particles from amorphous to the tetragonal anatase structure. Consequently, the DSC investigation confirmed the data obtained from the XRD analysis, demonstrating the crystallization in the tetragonal anatase phase only for samples A and B.

Figure 63 reports FE-SEM images of the three different magnetite-TiO_2 samples. Apparently, no macroscopic differences were detected: all the materials presented a very similar roughly spherical morphology with large aggregates in which the TiO_2 NPs have dimensions of about 10 nm.

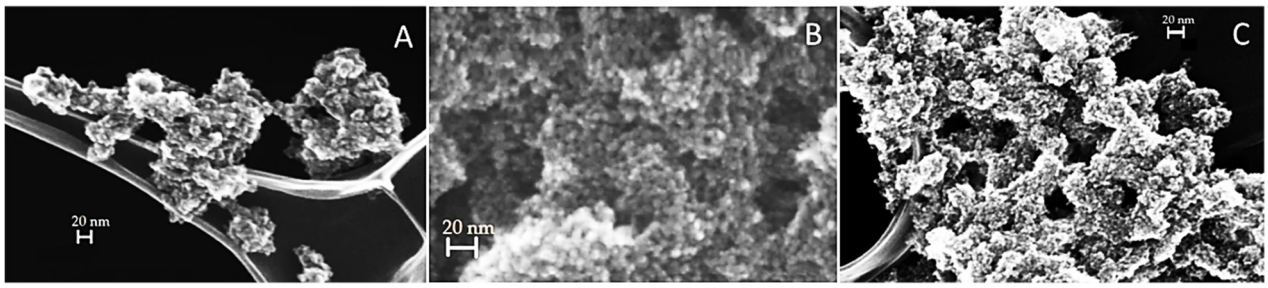

Figure 63. FE-SEM images of the three samples.

Finally, the surface area analysis, reported in Table 1, showed an evident increase in the surface to mass ratio, from 174.83 to 302.39 m^2/g from sample A to sample C respectively. All these values were lower than pure TiO_2 NPs surface area (D system with 341.86 m^2/g). The increase in the surface area is strictly correlated to the decrease of the crystallinity grade, as the aforementioned XRD analysis revealed. Since the adopted synthesis protocol in all the samples is the same, except the concentration of magnetite NPs, a clear dependence between the amount of Fe_3O_4 and the morphological and crystalline properties of the materials was observed. Decreasing the amount of magnetite, from sample A to D, a contemporary decrease in crystallinity and increase in surface area is clearly demonstrated. This general behavior can be correlated to the role of Fe_3O_4 nanoparticles that act, in the whole synthesis process, only as germination seeds for the growing and crystallization of TiO_2 in the anatase phase.

Sample	**BET (m^2/g)**
A	174.83
B	286.73
C	302.39
D	341.86

Table 12. Surface areas determined for the different samples.

4.2.1.2 Photocatalytic activity

Figure 64 reports the efficiency of the methylene blue degradation using the hybrid TiO_2/Fe_3O_4 samples (A, B, C) in comparison with pure TiO_2 NPs (sample D), synthesized in the same conditions but without the presence of magnetite, and commercial P25, *i.e.* TiO_2 powders from Sigma Aldrich. Magnetite NPs, tested in the same conditions, do not show photocatalytic activity towards MB. Sample D results the less active even if presenting the best surface area; this fact is clearly related to the low crystallinity that affects drastically the catalytic performance.

Even if from the XRD also sample C resulted amorphous, its degradation efficiency is similar to sample A; apparently, the synergic effect between surface area and crystallinity played an important role.

Consequently, sample A possessed a larger number of particles in anatase structure, but suffered for the lack in surface area; on the contrary, for sample C the high surface area compensated the low crystalline grade. However, the two samples reach a degradation of about 70% after 120 min of light exposure, value lower of only 10% respect to P25.

The best catalytic performance is reached by sample B that shows a conversion up to 95% after 120 min. It is noteworthy that, already after 60 min, sample B degrades more than 60% of MB.

The percentage of degradation (D%) was determined using the relation[98]:

$$D\% = \frac{C_0 - C_t}{C_0} \cdot 100$$

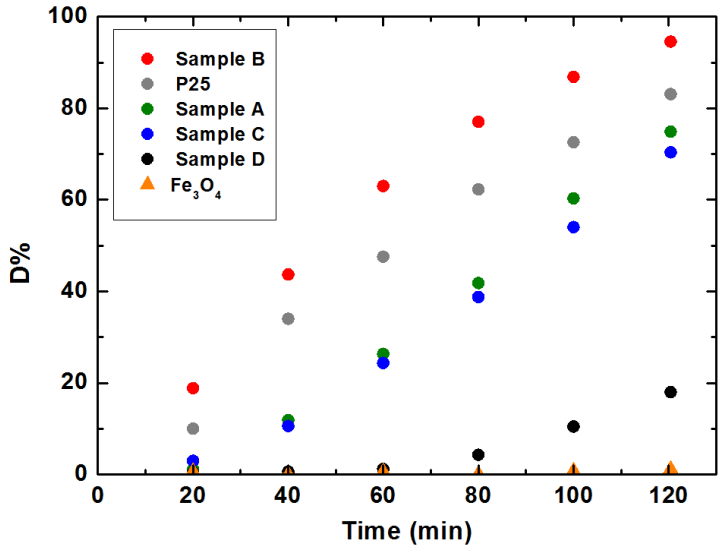

Figure 64. Percent degradation of MB versus time. The experimental points are averaged over three replicates with an error smaller than the used symbols.

Finally, the photocatalytic efficiency of the best material was tested for the degradation of OFL, a real emerging contaminant, in natural water sample. Among FQs, this compound was selected due to its wide presence in environmental matrices, and also because it is characterized by a slower photolytic decay in water matrices compared to other drugs.

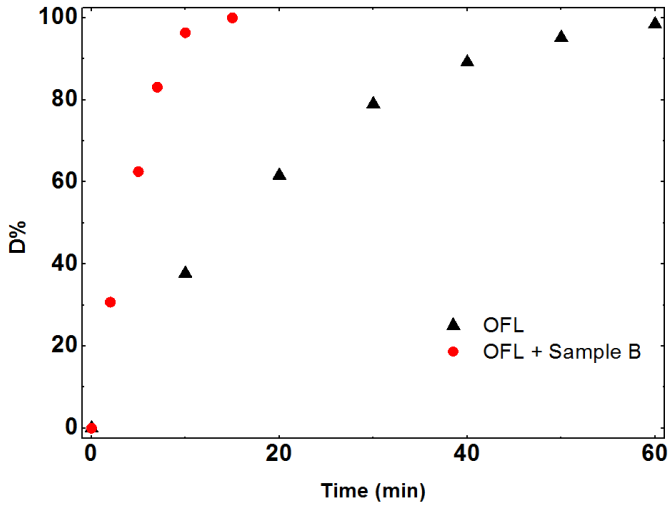

Figure 65. Photolytic (▲) and photocatalytic (●) degradation profiles of OFL under simulated solar light. The experimental points are averaged over three replicates with an error smaller than the used symbols.

Before irradiation, spiked samples (10 mg/L OFL, 0.5 g/L catalyst) were stirred in the dark, for 20 min to achieve sorption equilibrium. Under these conditions, a significant percentage of OFL was adsorbed onto the catalyst, namely 17%. As shown in Figure 61, a quantitative abatement (> 96%) of OFL was gained under simulated solar light in just 10 min. On the contrary, in the same experimental conditions, about 60 min were required to obtain a comparable degradation efficiency under direct photolysis.

4.2.2 NPs seed mediated synthesis for photocatalytically active TiO_2 NPs

Based on the good results obtained in the preparation of Fe_3O_4@TiO_2 NPs as hybrid photocatalytic material, other types of NPs have been tested as nucleation seeds for the synthesis TiO_2 NPs.
In particular, magnetic MFe_2O_4 ferrites (where M is Iron, Cobalt and Nickel) and non-magnetic lutetium oxide (Lu_2O_3) NPs were used during the synthesis of titania NPs.
STEM and TEM images of the seeds NPs are reported in Figure 66.

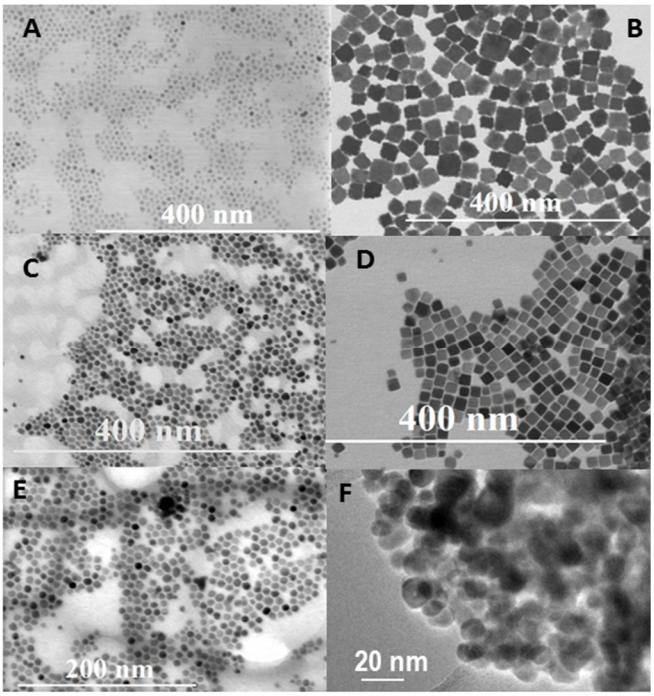

Figure 66. STEM images of Nickel ferrite seeds (A-B), Cobalt ferrite seeds (C-D), Fe_3O_4 seeds (E) and TEM image of Lu_2O_3 seeds (F).

It is important to notice that the different nucleation seeds have different morphological aspects, as the nanoparticles present different dimensions and shapes. Their size ranges from 8 to 30 nm, with cubic or spherical shapes, but all present cubic lattices.

Sample	Seeds chemical composition	Seeds size (nm)	Seeds shape	Seeds crystallographic structure	Theoretical lattice parameters
Sample 1	$NiFe_2O_4$	30 ± 5.2	Cubic	cF56 – Fd-3m	8.338 Å
Sample 2	$NiFe_2O_4$	8.8 ± 1.2	Spherical	cF56 – Fd-3m	8.338 Å
Sample 3	$CoFe_2O_4$	8.6 ± 2.1	Spherical	cF56 – Fd-3m	8.392 Å
Sample 4	$CoFe_2O_4$	17.2 ± 3.4	Cuboctahedron	cF56 – Fd-3m	8.392 Å
Sample 5	Fe_3O_4	7.2 ± 1.2	Spherical	cF56 – Fd-3m	8.394 Å
Sample 6	Lu_2O_3	19 ± 6	Distorted spherical	cI180 – Ia-3	10.39 Å

Table 13. Chemical composition, size, shape and crystallographic structure of the nucleation seeds.

These parameters, reported in Table 13, have been chosen to state if the crystallization of the tetragonal anatase phase would be anyhow affected by these ones.

4.2.2.1 Chemico-physical characterization

XRD analysis

In Figure 67, the XRD spectra of the synthesized samples are shown, together with the line pattern of the TiO_2 anatase, from the Pearson's Crystal Data software. It is possible to state that, whichever is the seed used, the temperature and pressure conditions reached with the hydrothermal synthesis can crystallize the amorphous titanium dioxide in the tetragonal anatase structure thanks to the presence of the nucleation seeds with a concentration one thousand times lower than the TiO_2. In fact, for each sample synthesized, it is possible to identify the typical anatase peaks without any other signal ascribed to secondary phases. The only slight difference that can be detected, but unfortunately not quantifiable with this kind of characterization, is the presence of small amounts of amorphous TiO_2; this can be roughly estimated from the goodness of the baseline. We couldn't make a comparison with a blank sample, since TiO_2 NPs were prepared by hydrothermal synthesis without any nucleation seed in the synthesis vessel: the obtained sample was completely amorphous, preventing thus any information from the XRD analysis.

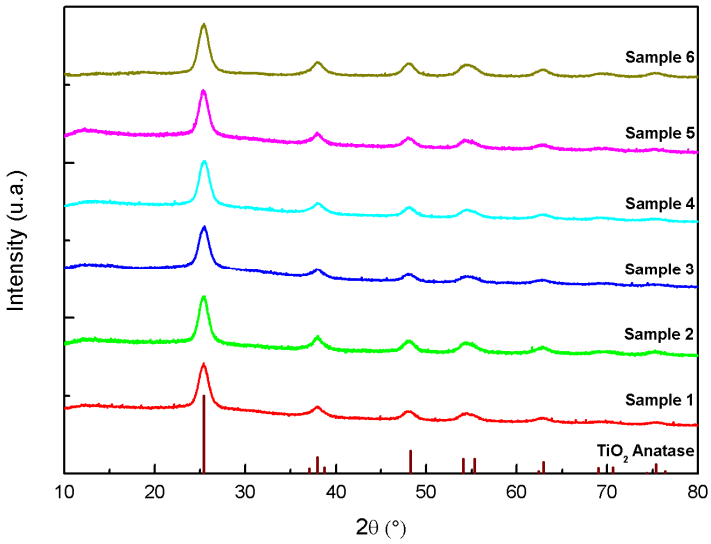

Figure 67. XRD patterns of the synthesized samples and the anatase TiO_2 reference pattern (line pattern).

The microstructural properties of the six synthesized samples are very similar for each systerm. This lack of difference could be assigned to the unspecific mechanism of the nucleation, as the ferrite nanoparticle acts as nucleation seed for other TiO_2 nanoparticles: titania doesn't grow homogeneously on the ferrite's surface but it begins to crystallize in certain spots of the ferrite surface and then the so-formed TiO_2 nanoparticle acts itself as new nucleation seed for further anatase TiO_2 nucleation.
It is noteworth that the crystallization of the tetragonal anatase phase occurred for every type of nucleation seeds used in the synthesis, even if they present different characteristics as the lattice parameter that varies from 8.338 for $NiFe_2O_4$ to 10.39 for Lu_2O_3. Thus, the nucleation is not affected by crystalline structure and/or lattice parameters of the seeds but it's an aspecific mechanism.

FE-SEM analysis

In Figure 68, the surface morphology of the samples is presented. All the synthesized samples show a similar morphology, so only FE-SEM images of sample 3 and 4 are presented. It is possible to state that the samples show a very small spongy appearance, with single particles with diameter ranging from 5 to 15 nm, mostly aggregated with each other in micrometric agglomerates.

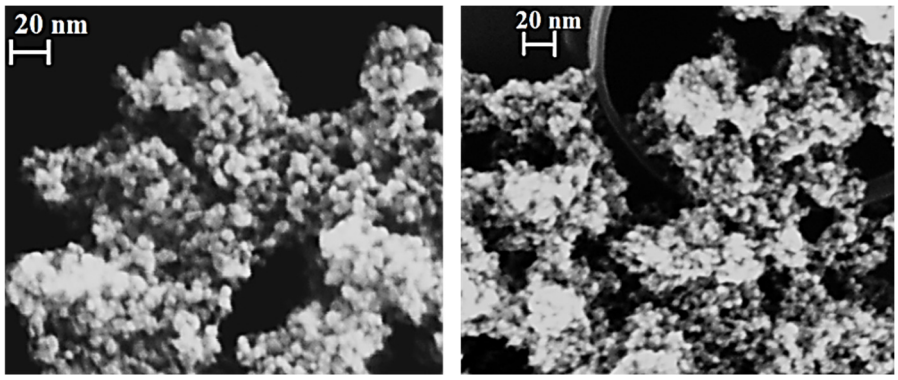

Figure 68. FE-SEM images taken at 20 kV of Sample 3 (left) and of Sample 4 (right).

Differential Scanning Calorimetry

The thermal behavior of the synthesized samples is shown in Figure 68. Each sample shows a similar trend, with a first endothermic peak due to the desorption of water around 80°C. Then, an exothermic signal is visible for each sample at a T_{onset} equal to about 210 °C, with a slight difference in the underlying area under the thermal signals, which can be ascribed to the amount of 2-propanol, arising from the sol-gel synthesis, physically adsorbed on the TiO_2 surface and burnt in the DSC analysis. A second small and broad exothermic peak, centered at around 380 °C, related to the phase transition from amorphous to anatase, can also be detected in all the samples. From this last thermal signal, we can state that the different nucleation seeds lead to different (small) amounts of amorphous residual phase, which, as noticed from X Ray diffraction data, can be anyway neglected with respect to the crystalline phase.

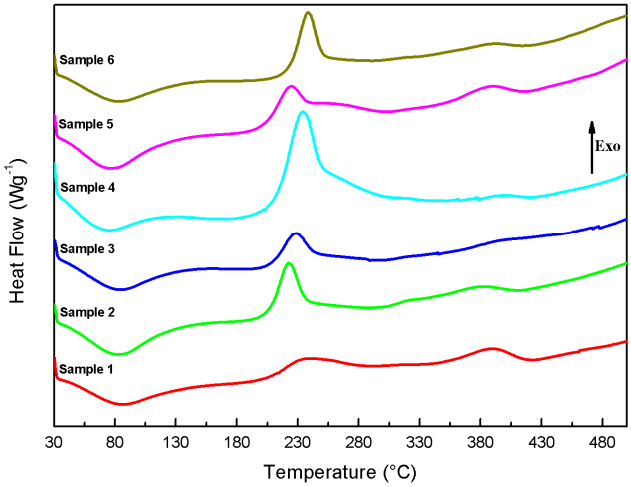

Figure 68. Thermal behavior of the different synthesized samples investigated under O_2 flow (20 mL/min) between RT and 500°C.

4.2.2.2 BET and Photocatalytic Experiments

In Table 14 the data from photocatalytic experiments, made in triplicate (n=3), are reported.

Sample	Degradation (%) (120 min)	St. Dev. (n=3)
Sample 1	98.71	1.38
Sample 2	95.36	4.01
Sample 3	97.94	1.26
Sample 4	97.11	2.10
Sample 5	98.78	0.59
Sample 6	96.88	0.10

Table 14. Photocatalytic efficiency of the synthesized samples

Concerning BET analyses, we couldn't perform the analysis for every sample and we decided to investigate the samples with Co ferrites with two different shape and dimensions, to justify the different thermal behavior highlighted with the DSC analysis and to compare the results with known data.

As we can see, the photocatalytic efficiency of the samples results to be the same for each one: considering the standard deviation, the percentage degradation values fit in the same range for every sample, thus indicating that the difference in the nucleation seed doesn't affect the photocatalytic efficiency at all. This peculiar efficiency must be related to the surface area, which settles to very high values for all the samples, thanks to the hydrothermal synthesis, which prevents the sintering of the powders, a disadvantage usually obtained with furnace thermal treatments, leaving the samples with a high surface to mass ratio. It is indeed demonstrated that the slight difference in the surface area, as shown by the BET measurements, reflects in slight different thermal behaviors: in fact, it can be oserved that sample 3 and 4, for which BET measurements have been made and are respectively equal to 200.23(1) and 218.30(1) m^2/g, show a different underlying area for the exothermic peak at a T_{onset} of 210°C attributable to the thermal desorption and decomposition of organic compounds, which burn under O_2 flow.

The BET measurement performed on the blank sample gave a surface area value equal to 341.86 m^2/g [99], but the photocatalytic activity of this sample is much lower than our samples: the sample is amorphous and reaches a methylene blue percentage degradation of 20%, in the same experimental conditions. The surface area of a solid state treated sample is much lower, as it is equal to 122.2 m^2/g [100], when annealed at 400°C in a furnace. Even if the annealing process allows to obtain the anatase structure, better for photocatalysis, the low value of the surface area prevents to achieve high degradation values. The photocatalytic activity of this sample, investigated with salicylic acid degradation, reached a value of around 35% in 250 min.

Conclusions

The aim of my PhD project was to investigate nanosized systems with potential applications in the biomedical and environmental field. In Chapter 3 of this thesis, results concerning iron based nanoparticles for different potential biomedical applications are reported. Among them, magnetite NPs are the most extensively investigated. From a chemical point of view, a modified coprecipitation method was employed to synthesize magnetite NPs. A silane derivative, carrying an amino group able to bond organic moieties to functionalize the MNP, has been attached on the surface of the nanoparticles by a hydrolysis and condensation process.
In a first step, a linker molecule (APTES) was bonded to magnetite thanks to the reaction between outward – OH groups and the ethoxy groups of APTES molecule. In the second step, converting the amino group into an isocyanate group, it was possible to couple the tripeptide-pyrene molecule. To evaluate another coupling approach of the tripeptide-pyrene to APTES functionalized NPs, we added a further linker, *i.e*. a dicarboxylic acid, between APTES and tripeptide. This second reaction was found to be milder and easier than the previous one, allowing also to achieve higher loading of tripeptide-pyrene.

Even if the synthesis represents the most important part of the work, great effort was dedicated to the evaluation of enzyme promoted cleavage of pyrenemethylamine from the nanoparticles. Although in this preliminary investigation the released molecule was only a simple fluorescent compound (pyrenylmethylamine), the same strategy can be applied to the release of other molecules as cytotoxic drugs. The tripeptide specifier has been designed in order to selectively release the organic molecule upon the action of a lysine selective serine protease such as trypsin or plasmin. Although the rate of enzymatic cleavage is quite low in both cases, urea and dicarboxylic acid linkers (7.1% and 5.8% respectively), this is not a disadvantage in view of continuous, slow release of a drug from the nanoparticle. The well-established possibility to guide magnetic nanoparticles to the malignant tissues coupled with the overexpression of proteases such as plasmin in many tumour cells, might allow a substantial increase in the therapeutic index.

Within biomedical applications, relevant results were obtained among SPION/sorafenib/micelles and Solid Lipid Nanoparticles (SLNs) topics. In particular, our effort was focused on the magnetic characterization of samples (prepared by the research team of the University of Bari) and the realization of a dynamic flow circuit to evaluate the accumulation of micelles in a simulated blood flow.
Magnetic characterization has confirmed not only the successful encapsulation of SPIONs in the core of the micelles, but, remarkably, has also demonstrated itself an extremely effective tool to quantify the magnetic NPs in a formulation. The design and application of the *in vitro* dynamic circuit simulating blood flow rates in the liver has proven that the SPION/micelles can be efficiently captured by a magnetic field, suggesting that they could be magnetically targeted to tumor sites under typical blood flow conditions found in the human liver.
The *Bari* group have performed a systematic study of the *in vitro* response of HepG2 cells exposed to SPION/sorafenib/Micelles to assess toxicity and the influence of a magnetic field on their toxicity. The experimental results have demonstrated that the antitumor activity of sorafenib is fully preserved upon encapsulation in hydrophobic micelle cores and that the presence of a magnetic field enhances cell internalization of SPION micelles, without affecting cell viability. Finally, cell recovery

experiments have highlighted the occurrence of slower release kinetics in SPION/sorafenib/Micelles treated cells than in cells incubated with free sorafenib.
Remarkably, the magnetically targeted SPION/sorafenib/Micelles have demonstrated superior antitumor efficacy. The PEG-PE micelles have enabled the convenient combination of an anticancer drug with magnetic NP based nanovectors in one versatile nanoformulation that can be magnetically concentrated in tumor tissues. This nanoformulation could potentially have a high impact on magnetically targeted therapies for HCC.

The last research activity among biomedical field concerns the preparation of ferrite based nanoparticles with core-shell and multi-shell structures to gain enhanced magnetic properties for a possible application in the field of the magnetic hyperthermia. Two configurations have been adopted, based on the alternating a hard $CoFe_2O_4$ phase and a soft phase $NiFe_2O_4$ or Fe_3O_4: conventional hard/soft and inverse soft/hard structures. STEM images allowed to determine the increase of dimension, thus confirming the formation of a shell on the cores.
For both core-shell systems, the magnetic coupling between the seed and the core-shell sample can be observed from the hysteresis cycles. The growth of a soft Ni ferrite shell affects the hard properties of the Cobalt ferrite seeds resulting in a decrease from 1.3 T to 0.8 T; on the contrary, the growth of a hard shell increases the value of the coercive field of the soft seeds of more than one order of magnitude (0.02 T to 0.3 T).
Multi-shell structures have been synthesized through multiple high decomposition syntheses. The system dimensions increase from 8.6 nm to 19 nm, and through HR-TEM images the multi-shell structure can be confirmed. As occurred for the conventional core-shell NPs, also in this case the magnetic hysteresis cycles should show a decreasing in coercive field, on the growing of soft shells. Indeed, it occurs for the second and third shell NPs but surprisingly not for the first shell NPs; an increase of $\mu_0 H_c$ is instead observed. This is due to the exchange coupling phenomenon that affect the magnetic properties of the system, enhancing the coercivity, when the shell thickness is very thin, as occurred in this case (0.7 nm).
In the framework of environmental applications, we successfully synthesized magnetite nanoparticles and functionalize them with thiol-silane derivative, achieving the product named Fe_3O_4@MPTMS NPs. The samples have been completely characterized by FE-SEM microscopy, FT-IR spectroscopy and TGA analysis.
Fe_3O_4@MPTMS NPs were employed in the capture and the recovery of toxic metal ions as Pb (II), Cu (II), Cd (II) and Ag (I) from waters. The most investigated metal was Pb (II) that allowed to optimize the method.
Two approaches have been adopted: *i*) a static mode, in which the capture and recovery occur in a Falcon test tube, thus in a small volume (50 mL), using an optimized configuration of commercial NdFeB ring permanent magnets; *ii*) a dynamic mode, in which an appositely designed glass capillary circuit has been built to treat higher volumes of polluted water, up to 1 L.
It should be pointed out that our optimized magnet configuration was able to collect more than 99% of magnetic nanoparticles in ten minutes and, adopting the correct nanoparticle concentration (300 ppm), more than 91% of Pb (II) in the same time.
Furthermore, we have demonstrated the possibility to perform a regeneration of the nanoadsorbents, and reuse them to capture again Pb^{2+} ions up to five cycles. The regeneration has been achieved through the recovery of the heavy metal ions by complexation of Pb with EDTA solution.

Even if the Pb^{2+} capture decreased after the first cycle to the fifth cycle (from 85.6% to 34.4%), the EDTA mediated regeneration of the NPs was always very efficient up to 80% of recovered Pb (II).
Concerning the other metal ions investigated, Cd (II) and Cu (II) captures reached 10% and 36% respectively, indicating that the interaction between these two metals and NPs is significantly lower than that with Pb (II).
We optimized a dynamic circuit to treat higher amount of polluted water, increasing the volume up to 1 L. Preliminary experiments showed the possibility to collect more than 90% of NPs in one hour, with a Pb^{2+} uptake up to 21%; optimization of the fluid flux rate and/or the design of the circuit could be key factors to improve the heavy metal capture.

Within photocatalysis, a simple sol-gel process approach was developed for the preparation of Fe_3O_4 - TiO_2 nanopowders. Different Fe_3O_4/TiO_2 molar ratios have been studied to test the photocatalytic activity in the degradation of Methylene Blue and Ofloxacin antibiotic, an emerging water pollutant, in the UV–visible light range.
Fe_3O_4 NPs can improve the photocatalytic activity of titania because they act, as germination seeds, for the crystallization of TiO_2 NPs in the anatase structure at a temperature lower than that reported in the literature. The combination of higher crystallinity grade and surface area provides an enhancement in the photocatalytic activity for sample B: the efficiency of our NPs in the MB and OFL degradation is even higher than the P25 commercial titania powders. Indeed, the reached percentage degradation, with the same exposure time, is 15% greater compared to commercial P25 TiO_2.

To evaluate the influence of other types of seeds, different NPs, Cobalt and Nickel ferrites and Lu_2O_3 NPs, have been employed. As occurred for magnetite, small amount of NPs (NPs/TiO_2 1:1000) have been added during the synthesis of TiO_2.
The presence of this small amount of ferrite nanoparticles in the hydrothermal reactor allows to obtain crystalline titanium dioxide, as the nanoparticle can act again as nucleation seeds. The nucleation starts onto the ferrite nanoparticle surface, forming thus a crystalline anatase seed which in turn will act itself as a new nucleation seed for the continuation of the TiO_2 crystallization. We have demonstrated that the nucleation proceeds in the same way for every NPs seed.
The diffraction patterns, the surface area, the thermal behavior and the photocatalytic activity of each sample results to be the same for every kind of nanoparticle used as nucleation seed. Furthermore, it is demonstrated that it is not necessary to use a ferrite structured nanoparticle, as the same results can be achieved even with the lutetium oxide which doesn't have neither a ferrite structure nor magnetic properties.

5 Appendix A – ^{1}H and ^{13}C spectra of all new compounds

^{1}H-NMR and ^{13}C-NMR of compound 7

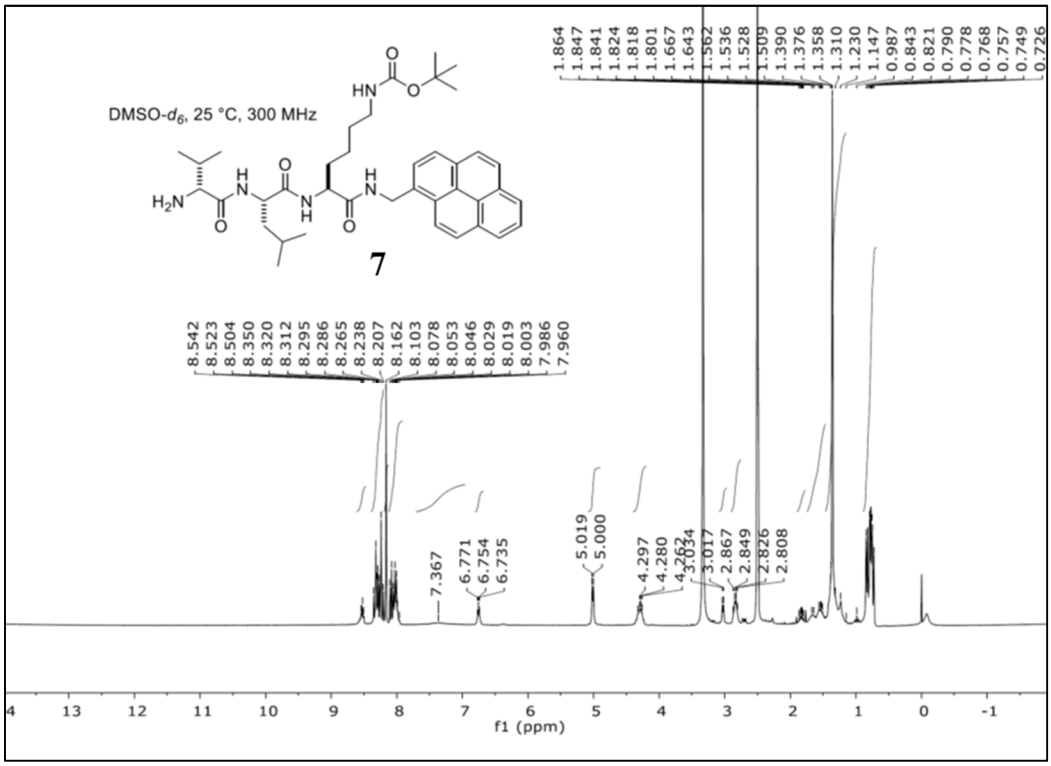

Figure A-1. ^{1}H-NMR compound **7**.

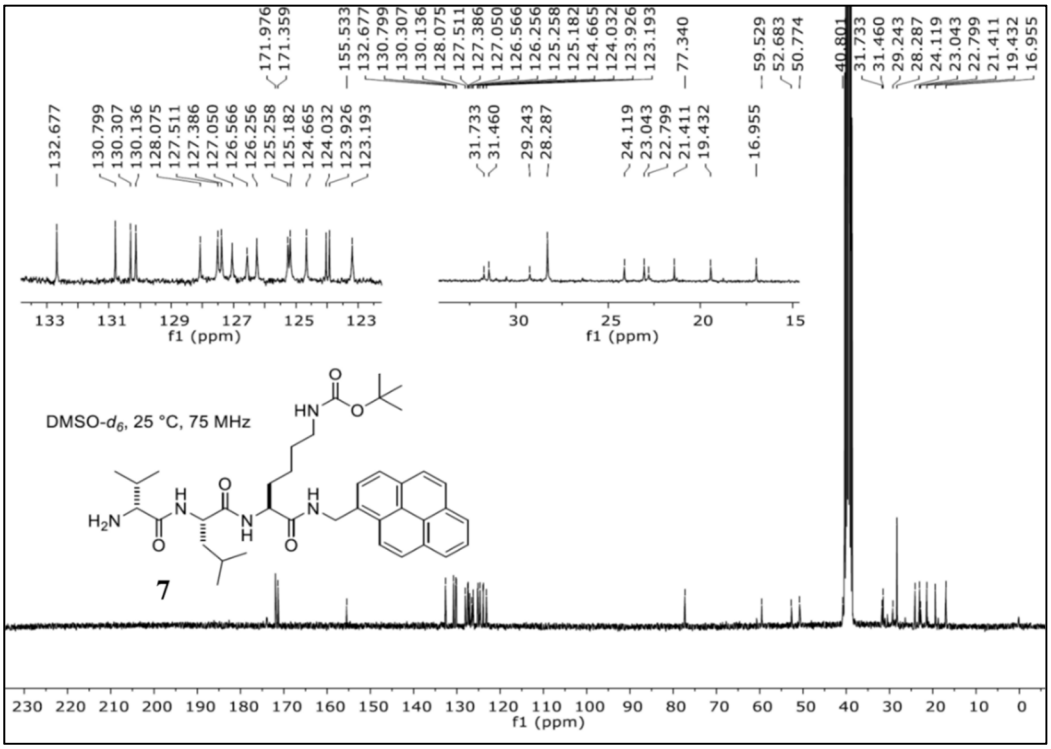

Figure A-2. ^{13}C-NMR compound **7**.

***tert*-Butyl ((*S*)-5-((*S*)-2-((*R*)-2-amino-3-methylbutanamido)-4-methylpentanamido)-6-oxo-6-((pyren-1-methyl)amino)hexyl)carbamate 7**. A suspension of 1-pyrenemethylamine hydrochloride (197 mg, 0.737 mmol) in dry DMF (25 mL, 0.03 M) was treated with diisopropylmethylamine (642 µL, 3.68 mmol), peptide **5** (400 mg, 0.737 mmol) and HATU (280 mg, 0.737 mmol) at RT under N_2 atmosphere. After stirring at RT for 18 h, the mixture was partitioned between EtOAc (40 mL) and brine (40 mL). Although the desired product was rather insoluble in both phases, it tends to disperse in the organic phase, and thus separation was anyway possible. The phases were separated and the aqueous phase was re-extracted twice with EtOAc (2 × 20 mL). The combined organic phases were washed with brine (3 ×) and concentrated to dryness. The residue (yellow solid) was used in the next step without further purification. It was suspended in dry and degassed THF (14 mL, 0.05 M) and treated with $Pd(PPh_3)_4$ (85 mg, 10 mol%) and phenylsilane (910 µL, 7.37 mmol) at 0 °C under an Ar atmosphere. After stirring at rt for 4 h, the dark mixture was concentrated and purified by flash column chromatography on silica gel eluting with 5% MeOH in DCM to give **7** (272 mg, off-white solid, 55% from **5**). M.p. = 200–201 °C. R_f = 0.59 (DCM/MeOH 9:1; UV and HBr followed by ninhydrin). $[\alpha]_D^{24}$ = −10.2 (*c* = 1.0, MeOH). ^{1}HNMR (300 MHz, DMSO-*d*$_6$, 25 °C): δ 8.52 (t, $^3J_{H,H}$ = 5.6 Hz, 1 H, N*H*-CH_2-pyrene), 8.39–8.20 (m, 5 H, CH pyrene), 8.16 (s, 2 H, CH pyrene), 8.13–7.91 (m, 4 H, NH Leu + NH Lys + CH pyrene), 6.75 (t, $^3J_{H,H}$ = 5.4 Hz, 1 H, NH Boc), 5.01 (d, $^3J_{H,H}$ = 5.7 Hz, 2 H, NH-C*H*$_2$-pyrene), 4.40–4.19 (m, 2 H, α-CH Leu + α-CH Lys), 3.03 (d, $^3J_{H,H}$ = 5.0 Hz, 1 H, α-CH Val), 2.90–2.75 (m, 2 H, α-CH_2 Lys), 1.89–1.77 (m, 1 H, β-CH Val), 1.74–1.47 (m, 3 H, β-CH_2 Leu + γ-CH Leu), 1.46–1.15 (m, 15 H, *t*Bu + β-CH_2 Lys + γ-CH_2 Lys + δ-CH_2 Lys), 0.88–0.68 (m, 12 H, 4×CH_3 Val and Leu). ^{13}C NMR (75 MHz, $CDCl_3$, 25 °C): δ 172.0 (2 × C=O amide), 171.4 (C=O amide), 155.5 (C=O Boc), 132.7 (C quat. pyrene), 130.8 (C quat. pyrene), 130.3 (C quat. pyrene), 130.1 (C quat. pyrene), 128.1 (C quat. pyrene), 127.5 (CH pyrene), 127.4 (CH pyrene), 127.0 (CH pyrene), 126.6 (CH pyrene), 126.3 (CH pyrene), 125.3 (CH pyrene), 125.2 (CH pyrene), 124.7 (CH pyrene), 124.0 (C quat. pyrene), 123.9 (C quat. pyrene), 123.2 (CH pyrene), 77.3 (C quat. *t*Bu), 59.5 (α-CH Val), 52.7 (α-CH Lys), 50.8 (α-CH Leu), 40.8 (β-CH_2 Leu), ~39.5 (ε-CH_2 Lys + NH-*C*H_2-pyrene buried by DMSO), 31.7 (β-CH_2 Lys), 31.5 (β-CH Val), 29.2 (CH_2 Leu), 28.3 (*t*Bu CH_3), 24.1 (γ-CH Leu), 23.0 (CH_3), 22.8 (CH_2 Leu), 21.4 (CH_3), 19.4 (CH_3), 16.9 (CH_3). I.R.: ῡ 3275 (w), 3043 (w), 2957 (w), 2930 (w), 2870 (w), 1678 (m), 1627 (s), 1530 (s), 1468 (m), 1390 (m), 1365 (m), 1276 (m), 1250 (m), 1168 (m), 1101 (w), 1064 (w), 1009 (w), 962 (w), 892 (w), 840 (s), 819 (m), 751 (m) cm^{-1}. HRMS (ESI+) m/z [M + H^+]: calcd. for $C_{39}H_{54}N_5O_5$ 672.4125; found 672.4128.

^{1}H-NMR and ^{13}C-NMR of compound 9

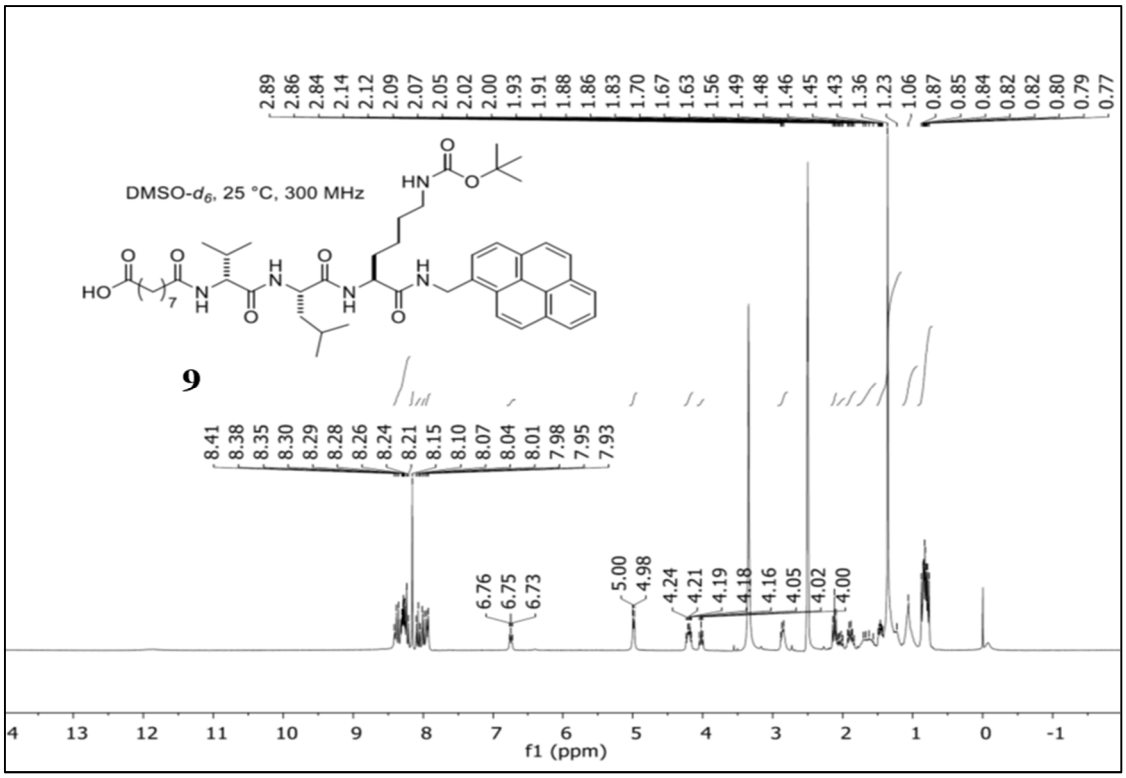

Figure A-3. ^{1}H-NMR compound **9**.

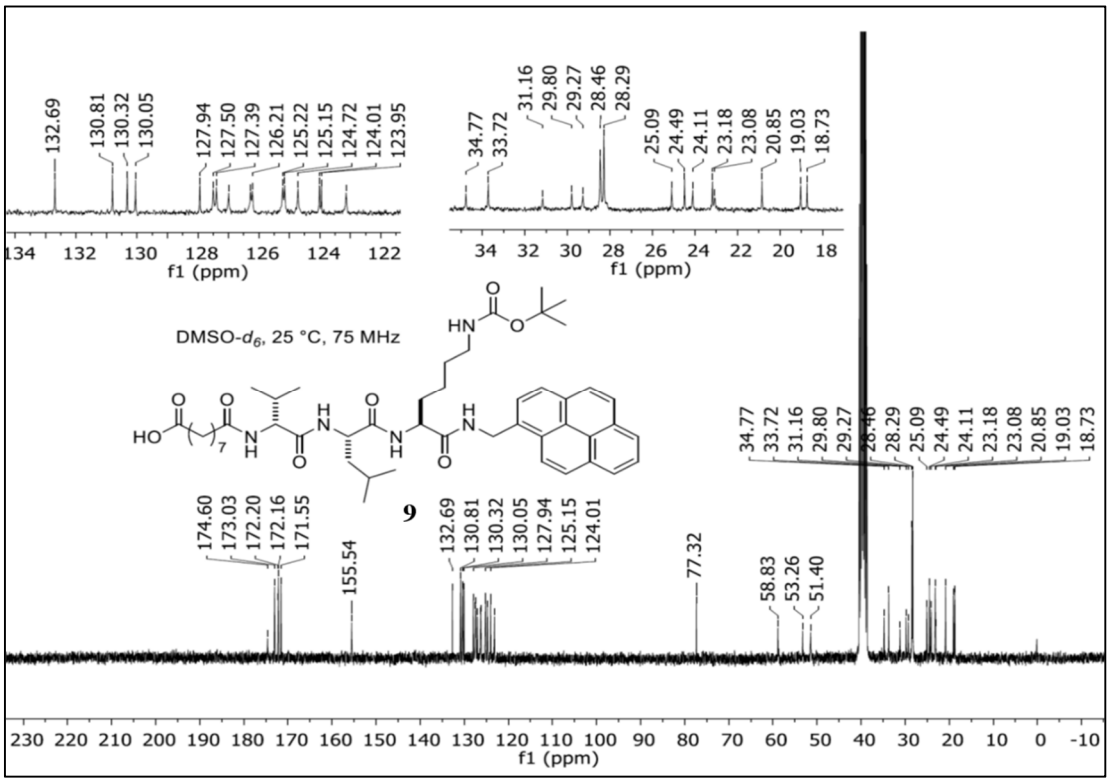

Figure A-4. ^{13}C-NMR compound **9**.

(10*S*,13*S*,16*R*)-13-Isobutyl-16-isopropyl-2,2-dimethyl-4,12,15,18-tetraoxo-10-((pyren-1-methyl)carbamoyl)-3-oxa-5,11,14,17-tetraazahexacosan-26-oic acid 9. A solution of **7** (99 mg, 0.147 mmol) in dry DMF (4 mL, 0.04 M) was treated with *N*,*N*-diisopropylethylamine (128 µL, 0.735 mmol), monomethyl azelate (31 mg, 0.154 mmol) and HATU (1-[*bis*(dimethylamino)methylene]-1*H*-1,2,3-triazolo[4,5-b]pyridinium 3-oxid hexafluorophosphate) (56 mg, 0.154 mmol) at rt under N_2 atmosphere. After stirring at RT for 3 h, the mixture was portioned between EtOAc (20 mL) and brine (20 mL). Although the desired product was rather insoluble in both phases, it tends to disperse in the organic phase, and thus separation was anyway possible. The aqueous phase was extracted with EtOAc (2 × 20 mL) and the combined organic phases were washed with brine (3 ×), and directly concentrated to dryness. The residue (yellow solid) was used in the next step without further purification. It was taken up in DMF (4 mL, 0.04 M) and treated with 1M NaOH (aqueous solution, 300 µL, 0.300 mmol) at rt. After stirring for 5 h, the mixture was partitioned between EtOAc (20 mL) and $(NH_4)H_2PO_4$ 5% aqueous solution (20 mL) 0.1 N HCl was added until pH 4. Although the desired product was rather insoluble in both phases, it tends to disperse in the organic phase, and thus separation was anyway possible. The aqueous phase was extracted with EtOAc (3 × 10 mL) and the combined organic phases were washed with brine (3 ×) and directly concentrated to dryness. The residue (yellow solid) was triturated with Et_2O to give **9** (106 mg, white solid, 85% from **7**). M.p.: 238 °C with decomposition. R_f = 0.24 (DCM/MeOH 95:5; UV and CAM). $[\alpha]_D^{24}$ = -10.7 (c = 0.49, EtOH). ^{1}H NMR (300 MHz, DMSO-*d*$_6$, 25 °C) δ = 8.44–8.20 (m, 7 H, N*H*-CH_2-pyrene + NH Val + CH pyrene), 8.15 (s, 2 H, CH pyrene), 8.07 (t, $^3J_{H,H}$ = 7.6 Hz, 1 H, CH pyrene), 8.00 (d, $^3J_{H,H}$ = 7.9 Hz, 1 H, CH pyrene), 7.94 (d, $^3J_{H,H}$ = 7.7 Hz, 2 H, NH Leu + NH Lys), 6.75 (t, $^3J_{H,H}$ = 5.6 Hz, 1 H, NH Boc), 4.99 (d, $^3J_{H,H}$ = 5.7 Hz, 2 H, CH_2-pyrene), 4.26–4.13 (m, 2 H, α-CH Leu + α-CH Lys), 4.02 (t, $^3J_{H,H}$ = 7.3 Hz, 1 H, α-CH Val), 2.92–2.80 (m, 2 H, ε-CH_2 Lys), 2.12 (t, $^3J_{H,H}$ =7.4 Hz, 2 H, C*H*$_2$$CO_2H$), 2.08–1.97 (m, 1 H), 1.96–1.82 (m, 2 H,), 1.80–1.52 (m, 3 H), 1.52–1.42 (m, 2 H), 1.36 (s, 9 H, *t*Bu), 1.42–1.15 (m, 8 H), 1.15–0.95 (m, 6 H), 0.94–0.67 (m, 12 H, 4×CH_3 Val and Leu). ^{13}C NMR (75 MHz, DMSO-*d*$_6$, 25 °C) δ = 174.6 (C=O), 173.0 (C=O), 172.2 (C=O), 172.2 (C=O), 171.5 (C=O), 155.5 (C=O Boc), 132.7 (C quat. pyrene), 130.8 (C quat. pyrene), 130.3 (C quat. pyrene), 130.1 (C quat. pyrene), 127.9 (C quat. pyrene), 127.5 (CH pyrene), 127.4 (CH pyrene), 127.0 (CH pyrene), 126.3 (CH pyrene), 126.2 (CH pyrene), 125.2 (CH pyrene), 125.2 (CH pyrene), 124.7 (CH pyrene), 124.0 (C quat. pyrene), 123.9 (C quat. pyrene), 123.1 (CH pyrene), 77.3 (C quat. *t*Bu), 58.8 (α-CH Val), 53.3 (α-CH Lys or α-CH Leu), 51.4 (α-CH Lys or α-CH Leu), ~39.52 (β-CH_2 Leu + ε-CH_2 Lys + CH_2-pyrene buried by DMSO), 34.8 (CH_2), 33.7 (*C*H_2CO_2H), 31.2 (CH_2), 29.8 (CH), 29.3(CH_2), 28.5 (3×CH_2), 28.3 (*t*Bu CH_3), 25.1(CH_2), 24.5 (CH_2), 24.1 (CH_2), 23.2 (CH_3), 23.1 (CH), 20.8 (CH_3), 19.0 (CH_3), 18.7 (CH_3). I.R.: ῡ 3272 (m), 3049 (w), 2930 (w), 2869 (w), 1680 (m), 1626 (s), 1532 (s), 1457 (m), 1390 (m), 1366 (m), 1277 (m), 1249 (m), 1226 (m), 1168 (m), 1102 (w), 1011 (w), 961 (w), 914 (w), 841 (m), 820 (w), 752 (m), 704 (m), 680 (m), 654 (m), 619 (m) cm^{-1}. HRMS (ESI+) m/z [M + H^+]: calcd. for $C_{48}H_{68}N_5O_8$ 842.5068; found 842.5074.

6 Appendix B - Characterization techniques

6.1 Scanning Electron Microscope (SEM)

Scanning electron microscope (SEM) is a fundamental instrument for the characterization of samples by direct observation of the structure and morphology. The radiation used to scan the sample is an electron beam that allows to reach spatial resolution much higher than that achievable with visible light. In this instrument, the acceleration voltage is lower than the one used for Transmission Electron Microscopy, TEM (20 keV instead of 200 keV) thus the maximum spatial resolution achievable is around 1.5 nm. The fundamental difference between the two instruments is the origin of the recorded signal; in the case of TEM, the electron beam passes through the sample and the image is created by the different deviation of the electron by the electron density of the sample. In the SEM, the detector is placed on the same side of the electron source thus only electrons arising from the sample are detected.

In the case of SEM, different signals can be detected obtaining different information about the sample. The interaction between the beam and the sample gives rise to two main categories of electrons coming out from the surface of the sample: backscattered electrons (BSE) and secondary electrons (SE), as pictured in Figure a.

BSE signal arise from elastic scattering with the electron cloud of the sample; this kind of electrons have a relatively high energy, higher than 50% of the primary beam energy. BSE are useful to obtain high compositional contrast since the backscattering coefficient is strongly affected by the atomic number of the sample.

SE arise from a complete different phenomenon. When high-energy electrons hit a sample, inelastic scattering can happen and electrons of the specimen can be ejected during the process. These electrons originally bonded to the samples (weakly bounded conduction e- and/or outer shell valence e-) once ejected are referred as the secondary electrons. The energy distribution of the secondary electrons is a narrow peak at very low energy around 2-5 eV with 90% of them with energy lower than 10 eV. Considering their low energy, SE can escape from the sample just if they are formed close to the surface thus the signal will be strongly related to the morphology of the sample.

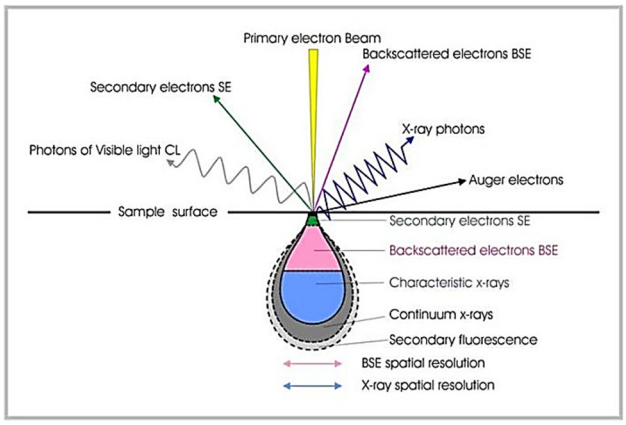

Figure B-1. Scheme of the signals deriving from the interaction between electron beam and sample.

In SEM instruments, the electron beam is provided by thermionic or field emission sources. For many of the samples synthesized through this thesis, the analyses were performed with a FE-SEM (Field Emission SEM) where a field emission gun is adopted. This electron source presents several advantages with respect to the thermoionic one, mainly related to better characteristics and higher stability of the produced beam. Once produced, the beam passes in the optical column (maintained under vacuum) where it is manipulated and finally focused on the sample thanks to electromagnetic lenses. Since the interaction between the beam and the sample brings to different signals, more specific detectors are required. In Figure B-2, a schematic section of the main parts of a SEM is reported.

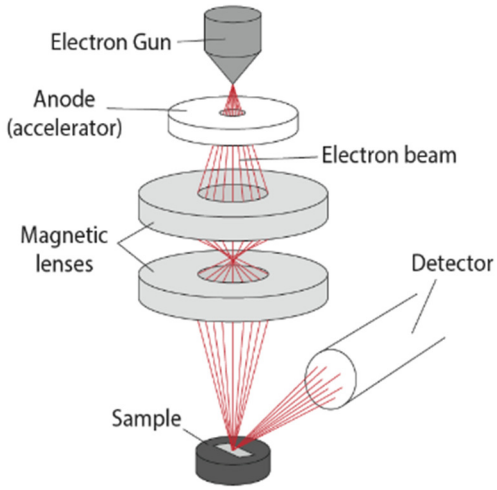

Figure B-2. Scheme of SEM from gun to sample.

High energy BSE are detected mainly by solid-state detector usually placed around the exit of the optical column. Low energy SE can be detected in different ways. The more common detector is the Everhart-Thornley detector, which is placed directly in the sample chamber. This detector generates the signal by means of a scintillator combined with a photomultiplier. Usually, it is combined with a Faraday cage placed around the scintillator whose potential regulates the fraction of electrons that will be detected. Even if this kind of detector is the most commonly used, it is affected by different problems. For example, contribution arising from BSE emitted in the solid angle of the detector is difficult to remove and furthermore SE generated by the interaction between BSE and the walls of the chamber can be detected as well.

A better SE signal can be collected by means of the In-Lens detector. In this case the detector is placed directly inside the optical column, thus the SE arising from the sample have to be forced in that direction before being revealed. This is commonly done by means of snorkeling lenses, *i.e.* electromagnetic lenses reaching the surface sample and forcing the path of the low energy SE. The use of this detector allows to obtain better images since it not affected by signals not related to the sample and moreover the signal is not related to the position of the detector with respect to the sample. This kind of detector has been used for most of the collected images. It is noteworthy to underline that the use of In-Lens detector needs a very low working distance, i.e. distance between the exit of the optical column and the sample. This is a limitation since it does not allow to use simultaneously the In-Lens detection and the EDX analysis.

Sample preparation: FE-SEM analysis has been performed on a large number of samples since it allows to directly appreciate the morphology and the dimension of the particles. The sample is prepared dispersing the powder in an appropriate solvent and sonicating the dispersion with ultrasonic horn. The concentration has to be low enough to ensure a good dispersion but high enough. Once prepared the dispersion, few drops (depending on the concentration) are deposited on the support. For screening purpose, almost every support can be used even if a smooth conducting surface has to be preferred. For high resolution images, we deposited the sample over TEM grid, i.e. copper grid where an amorphous carbon layer guarantees an extremely low noise support for the particles.

6.2 Scanning Transmission Electron Microscopy (STEM)

The Electronic Scanning and Transmission Microscope (STEM) is a valuable tool for characterizing nanostructures. It can be used in different image capture modes and also provides information on the elementary composition and the electronic structure of the material being examined.
This type of electron microscope has been used for characterizing samples prepared at NTNU (Norway) during my visiting research period.
The STEM microscope is based on the same principle of scanning electron microscopy (SEM); it uses a focused electron beam that is scanned on the sample, while the desired signals are collected to form an image. One of the main differences with the SEM microscope is the preparation of the sample, which must be very thin (<100 nm) so that it can take advantage of the transmission mode.
This requirement is fundamental in analyses performed with the Electronic Transmission Microscope (TEM) and it's achieved depositing the sample on special copper coated substrates (thin grid) of carbon (as already described for FE-SEM).
This prerogative along with its versatility makes the STEM microscope a quick means for the characterization of nanostructures. As in SEM, secondary (SE) or back-scattered (BSE) electrons can be used for imaging; but higher intensity signals for better spatial resolution are provided by transmitted electrons.

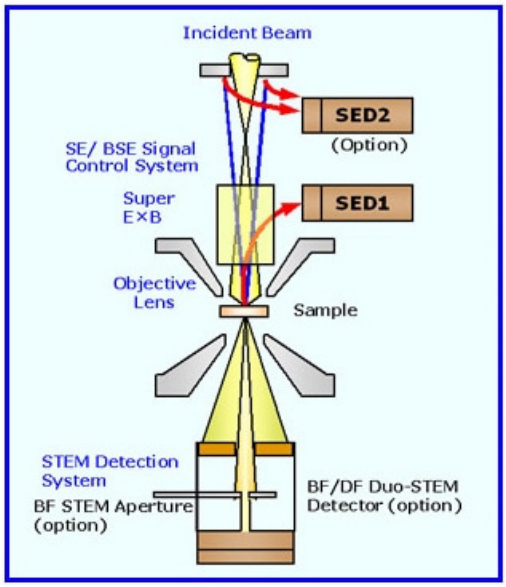

Figure B-3. Scheme of a STEM microscope.

The detectors commonly used include a light field detector (Bright Field, BF) intercepting the transmitted beam and a dark field detector (Dark Field, DF) surrounding the transmitted beam to collect scattered electrons. As can be seen from Figure B-3, the incident beam is collimated as in a TEM up to the sample.

Bright field detector

It is the most common mode of operation and represents a simple 2D projection of the sample. This small detector on the axis with the electron beam includes beam transmission through the sample so the sample appears dark and the light sample holder, hence the name bright field. The origin of the image contrast is due to the diffraction of Bragg (green circles in Figure B-4); in itself it would not produce an image but by reducing the intensity of the primary beam in areas that are properly oriented to have diffraction, it determines the local intensity of the image. This type of contrast is called "diffraction contrast". Because the contrast depends on the angle with which the beam affects the sample, the sample holder in the TEM as in the STEM allows rotating the sample to select the diffractions, and then highlight the details that interest.

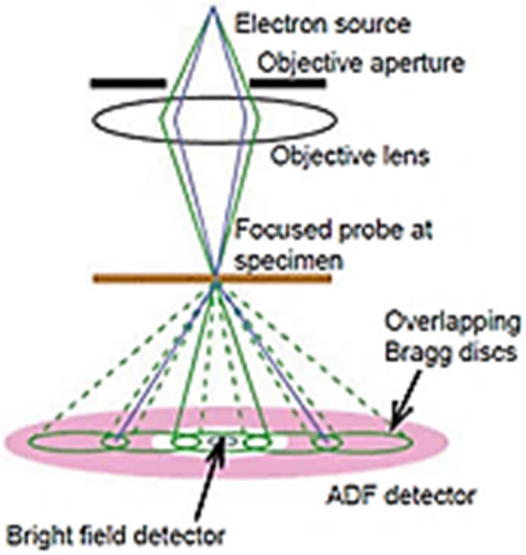

Figure B-4. Scheme of bright field detector.

Thanks to reciprocity theory, the BF-STEM system with convergent lighting and a small axis detector is similar to a high-resolution BF-TEM system with a small point source and a rather large detector. A disadvantage of both methods is that they are affected by contrast inversions and difficulties associated with the interpretation of a consistent signal.

Dark field detector

The dark field detector excludes the beam transmitted by showing the light sample and the dark support.
The inside angle of this detector can be changed by modifying the "camera length" with post-sample lenses to collect electron transmitted leaving the sample at relatively high angles to the optical axis (Figure B-5).

Samples can exhibit diffraction contrast, so the electron beam is discharged by Bragg, which in the case of a crystalline sample dissipates electrons in discrete positions in the posterior focal plane. By inserting openings in the rear focal plane, i.e. the lens aperture, the desired reflections of Bragg can be selected (or excluded), so only parts of the sample will be projected onto the imaging apparatus. The use of an annular detector to collect only electron scattered at higher angles (> 80 mrad), often referred to as High Angle Annular Dark Field (HAADF), results in a loss of consistency of the detected signal, thus improving resolution.
The Annular Dark Field (ADF) detectors produce an atomic, or Z-contrast, sensitivity image that follows the Zα power law, where α is between 1 and 2 depending on the angular field of electrons collected and related to the Debye-Waller factor.

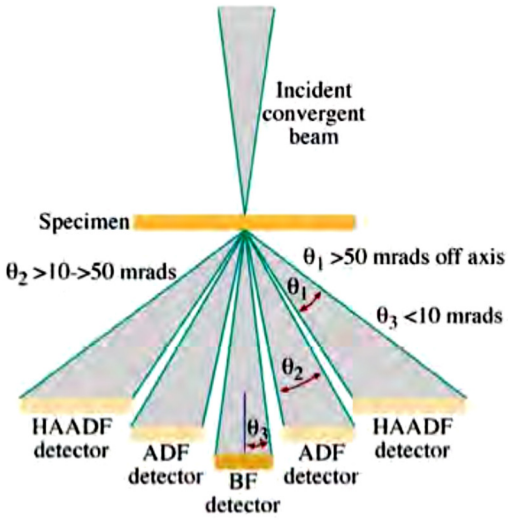

Figure B-5. Electrons scattering angles and related used detectors.

Analyses have been performed with Hitachi S-5500 STEM microscope using both detectors.

6.3 X-Ray Diffraction analyses

X-ray diffraction is a characterization method based on the elastic scattering of X-rays from materials with atomic or molecular long-range order. This phenomenon appears when a structure with long-range organization (crystals) interacts with a radiation whose wavelength lies in the same order of magnitude of the distance between the scattering elements. This is exactly the situation we have when X-rays (10^{-3} nm < λ <1 nm) are used to probe crystalline structures.

The radiation focused on crystalline samples interacts with the atoms and their electrons; this interaction creates new spherical waves characterized by the same wavelength of the starting radiation. Spherical waves arising from different atoms can interact constructively or not, depending on the difference in the optical path. In this way, depending on distance between scattering atoms, it is possible to observe high intensity for the diffracted radiation just in particular directions. The easiest way to describe the diffraction phenomenon is given by the Bragg equation where the effect is described as the X-ray reflection on the lattice planes, Figure f.

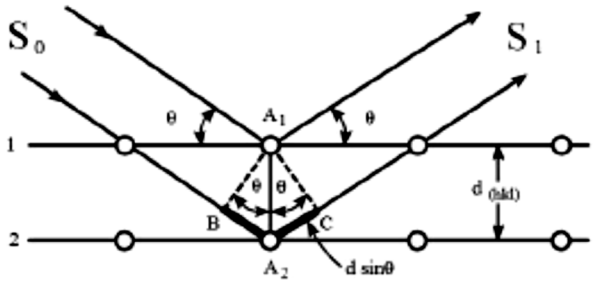

Figure B-6. X-ray diffraction from crystalline planes.

In the framework of this model, there is constructive interference just if the path of the radiations differs of an integer multiple of the wavelength, hence:

$$2d_{hkl} \sin\theta = n\lambda$$

where d_{hkl} is the distance between the planes, *hkl* are the Miller indexes characterizing the considered planes and θ is the angle of incidence. From this formula, it is possible to correlate the angle at which we observe intense diffraction peaks to the distance between the planes that gave rise to that particular reflection. Collecting the information from every peak, we are finally able to disclose the crystal structure and thus the chemical nature of the sample.

Considering the Bragg law, it is clear that, fixing the wavelength of the radiation and the orientation of the crystal with respect to the X-ray source, just a limited number of crystalline planes will satisfy the Bragg equation thus giving observable diffraction peaks. In order to solve this problem and to collect every possible diffraction peak, many different systems have been developed, depending on the nature of the sample under investigation (for example, single crystals or powders).

In this thesis, X-ray diffraction patterns have been collected from powder samples using a θ-2θ Bragg-Brentano diffractometer whose geometry is depicted in Figure g. In this case, the powders are placed in a sample holder positioned at the center of a goniometric circle, which rotates around the axis perpendicular to the direction of the beam. This rotation is combined with the movement of both the

X-ray source and the detector; in particular, at each θ rotation of the source, the detector moves of an angle 2θ.

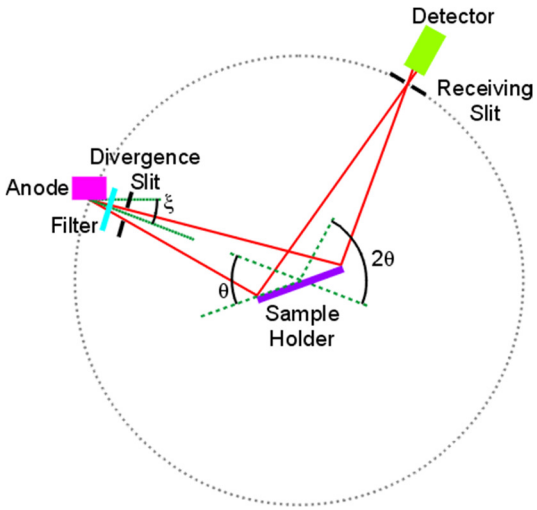

Figure B-6. Scheme of Bragg-Brentano diffractometer.

In our work, we mainly analyzed powder samples. For routine analysis, the XRD patterns have been collected by means of Bragg-Brentano diffractometer. In particular, the analyses performed at the University of Genoa have been made on an automatic diffractometer X'Pert with Cu Kα radiation (λ= 1.54056 nm). The patterns have been collected in the 2θ range 20°–100° with a step range of 0.02°. We prepared the samples placing the powders on a support and fixing it thanks to a Vaseline/hexane mixture. The same procedure has been adopted for the analyses performed at the NTNU laboratory, where the diffraction patterns were collected using a Bruker D8 Advance diffractometer (Cu Kα radiation) in the 2θ range 15°–75°.

6.4 Superconducting Quantum Interference Device (SQUID)

Magnetic analyses have been extensively performed to achieve important information about the samples. In fact, the magnetic behavior is strongly related to the chemical and morphological characteristics of the sample. In the case of NPs, dimensions can dramatically affect the magnetic properties, moving from a classic ferromagnetic (FM) behavior at the bulk state to the so-called superparamagnetic (SPM) state below a certain critical diameter. Usually, the information is obtained through the analysis of the magnetization as a function of the applied external field (hysteresis cycle) and as a function of the temperature (ZFC-FC curves).
The measurements were performed in a DC Superconducting Quantum Interference Device (SQUID). The central part is formed by two superconductors separated by thin insulating layers to form two parallel Josephson junctions. The device may be configured as a magnetometer to detect incredibly small magnetic fields. The Josephson junctions, crucial to the operation of the SQUID, are shown in Figure B-7.

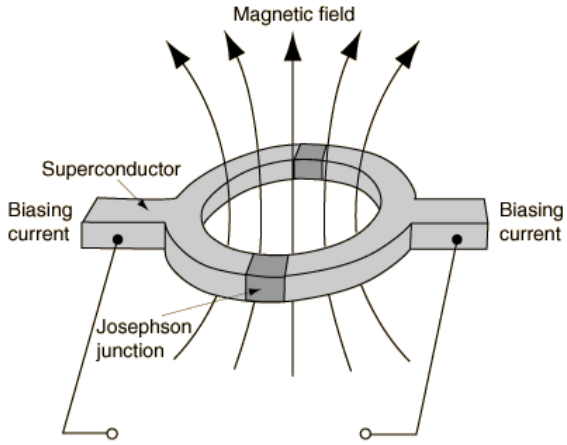

Figure B-7. Scheme of Josephson junctions in SQUID superconducting ring.

If a current flow in the ring, the wave function of the Cooper pairs will be affected by the presence of a magnetic flux through the ring by changing the wave function of the electrons. This phase change is due to the presence of an additional current in the ring, created by the external magnetic field coming from the sample. Experimentally, the magnetic properties of the sample are recorded by the change in the voltage of the ring caused by the appearance of the additional current generated by the magnetic flux.
All the components of the SQUID magnetometer are placed in liquid He, thus maintained at a temperature close to 4 K. During the measurement, the sample is constantly moved up and down close to the SQUID ring and the magnetic flux is integrated on the time.

The magnetization measured as a function of the external applied field has been investigated in the $\mu_0 H$ range -5 Tesla ÷ +5 Tesla. As a result of this measurement, saturation magnetization, coercive field and the remanence of the sample can be obtained. If the analyzed sample is a nanoscale material, dimensional information could be achieved. In case of SPM samples, the magnetization does not present hysteresis since the low energy barrier between the minimum states does not allow to retain a preferential orientation.
The energy barrier involved in this process is related to the chemico-physical properties of the materials and to its dimension; therefore, reaching information about the energy barrier, we can obtain

indication about the dimension of the system. This kind of information can be obtained from the investigation of the temperature dependence of the magnetization, which is usually obtained through the zero-field cooled – field cooled curves (ZFC-FC).
The experiment consists in two separate measurements where the magnetization is collected during the increasing of the temperature. For the ZFC curve, the sample is cooled to the liquid He temperature (without external magnetic fields) in order to completely block the magnetic moment, within each NP, along its lower energy direction (*i.e.* the easy axis direction). Once reached the minimum temperature, a small DC field (from 25 to 1000 Oe) is imposed to the sample and the temperature is slowly increased. In this situation, the increasing temperature slowly allows the magnetic moments to overcome the energy barrier searching for the minimum energy orientation.
At the same time, the presence of the external field promotes one direction with respect the other therefore encouraging the alignment of the moment in a certain direction. This effect can be observed macroscopically through an increasing of the magnetization of the sample. This trend continues until a certain temperature after that the small perturbation brought by the external field is overcome by the thermal energy that is now high enough to equally distribute the moment in random directions. This second part of the experiment is characterized by a decreasing of the magnetization of the system. The ZFC of SPM samples is therefore characterized by a maximum of the curve whose temperature is defined as blocking temperature (TB), i.e. the temperature below which the thermal energy is not sufficient to overcome the energy barrier between the two minima for the magnetic moment.
The second part of the experiment involves the measurement of the field cooled (FC) curve. In this case, the sample is cooled already in presence of the small external magnetic field down to the minimum temperature. The presence of the field in the cooling procedure will bring all the moments to be aligned once reached the lower temperature thus observing the highest value for the magnetization. During the heating ramp, the magnetization decreases monotonously due to the effect of the increasing thermal energy. At a characteristic temperature, the two curves overlap, identifying a separation temperature. The comparison between TB and the temperature of separation of the two curves gives an idea of the dimensional distribution of the sample; in the ideal case where all the particles have the same dimension, the two temperatures would be exactly the same.

Sample preparation

We performed the static magnetic measurements by means of a DC-superconducting quantum interference device (SQUID) magnetometer (MPMS magnetic properties measurement system, Quantum Design). The room temperature magnetic hysteresis cycle was measured with a magnetic field ($\mu_0 H$) in the range −5 to +5 T. The thermal dependence of the magnetization (H = 25 Oe, T = 5–300 K range) was obtained with the zero-field cooling-field cooling (ZFC-FC) procedure. All the analyses have been performed on powder samples fixing a small amount (~10 mg) in a plastic holder.

6.5 Thermogravimetric Analysis (TGA)

Thermogravimetric Analysis (TGA) is a well-established method for thermal characterization of materials.
The method has been optimized and automated and it became one of the key methods for the thermal characterization of solid and liquid materials.

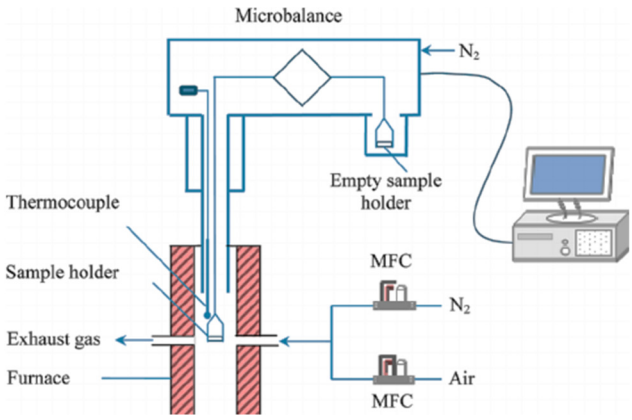

Figure B-8. Main components of a thermogravimetric analyzer.

In general, TGA is a technique in which the mass of a substance is monitored as a function of temperature or time as the sample is subjected to a controlled temperature program in a controlled atmosphere. The components of a thermogravimetric analyzer are relatively straightforward. It requires a high-resolution balance system, a furnace, a controller and some sort of a sample holder system as shown in Figure i. The pan containing the sample resides in a furnace and it is heated or cooled during the experiment. The measurement can be performed in inert atmosphere or in presence of reactive gas, giving the opportunity to observe many different phenomena. For example, such a system can be adopted to analyze the evaporation, decomposition or corrosion of a wide range of different materials such as polymers, pharmaceuticals, inorganics or metals.
Even if the analysis is not particularly demanding from an experimental point of view, many factors can affect the results. Instrumental parameters such as heating rate geometry of the pan and the furnace as well as sample-related parameters as mass, particles size and sample history, have to be carefully considered before the interpretation and the comparison between data sets. Furthermore, an accurate calibration of the balance has to be performed in order to avoid undesired effects (for example of the temperature) on the measured mass.

Sample Preparation
In the framework of this thesis, we used TGA to analyze the thermal behavior of NPs in a a Labsys EVO Setaram instrument. Approximately 5 mg of sample was weighted in an open alumina crucible and heated from 50 °C to 1000 °C in He flux (20 mL/min) with a heating rate equal to 10 °C/min.

6.6 Inductively Coupled Plasma–Atomic Emission Spectrometer (ICP-AES)

In an inductively coupled plasma-atomic emission spectrometer the aqueous sample is pumped and atomized with argon gas into the hot plasma. The sample is excited, emitting light wavelengths characteristic of its elements. A mirror reflects the light through the entrance slit of the spectrometer onto a grating that separates the element wavelengths onto photomultiplier detectors.

The relaxation of the excited electrons as they return to the ground state is accompanied by the emission of photons of light with an energy characteristic of the element. Because the sample contains a mixture of elements, a spectrum of light wavelengths is emitted simultaneously. The spectrometer uses a grating to disperse the light, separating the particular element emissions and directing each to a dedicated photomultiplier tube detector. A computer converts the electronic signal from the photomultiplier tubes into concentrations.

The analyzed samples were all in the form of aqueous solution and pneumatic nebulization was used to introduce the solutions into the instrument. The primary aerosol thus forms, with droplets size varying from some μm to about 100 μm. The so-formed aerosol still has excessive dimensions to be subjected to analysis: it is therefore entered into the misting chamber (the one used in the present work is a cyclonic nebulization chamber) within which droplets are forced into a swirling motion that breaks it further. Thus, the tertiary aerosol is obtained, for which the liquid only corresponds to about 5% of the aspirated sample.

The resulting aerosol is sent to the ICP torch by means of a connecting tube. The sample introduction system for this technique unfortunately allows only between 1 and 5% of the sample solution to be introduced.

The source is an inductively coupled plasma that, for this technique, constitutes both the atomization and excitation system of the sample. The optic used in this work was axial and there was a nickel cone to eliminate interferences.

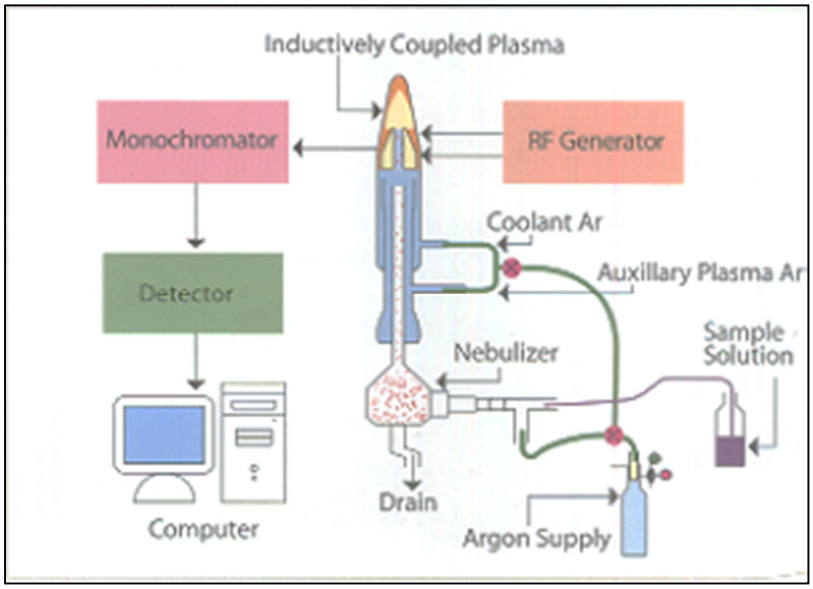

Figure B-9. Scheme of the instrumentation for ICP-AES technique.

The elements and the relative wavelengths are shown in the following table (wavelengths are reported in nm):

	Fe	**Pb**	**Ag**	**Cu**	**Cd**
λ_1	234.350	220.353	328.068	324.754	214.439
λ_2	240.489		338.289	327.395	226.502
λ_3	259.837				228.802

The detection limit is defined as the smallest concentration for which the analytical signal can be distinguished from the instrumental background. The theoretical instrumental detection limit for the analyzes is around 0.0003 ppm. The experimental detection limits obtained for the various analytes in the working conditions are hereafter listed: Fe 0.039 ppm, Pb 0.009 ppm, Cu 0.010 ppm, Ag 0.008 ppm and Cd 0.004 ppm. The instrumental precision of this technique is very high: the most significant contribution to instrumental noise is due to the sampling system. In addition, an internal standard (lutetium) has been used for all the analyzes.

Sample Preparation: In the framework of this thesis, we used ICP-AES to analyze solutions deriving from capture and recovery of metal ions by NPs in a ICP-AES VISTA PRO Varian (Springvale, Australia).

List of Publications

"Design and optimization of lipid-modified poly-(amidoamine) dendrimer coated iron oxide nanoparticles as probes for biomedical applications" A. Boni, G. Bardi, A. Bertero, V. Cappello, M. Emdin, A. Flori, M. Gemmi, C. Innocenti, L. Menichetti, C. Sangregorio, S. Villa and V. Piazza, RSC *Nanoscale*, 7, 7307, **2015**

"Different sol–gel preparations of iron-doped TiO_2 nanoparticles: characterization, photocatalytic activity and cytotoxicity" V. Caratto, F. Locardi, S. Alberti, S. Villa, E. Sanguineti, A. Martinelli, T. Balbi, L. Canesi, M. Ferretti, *J. Sol-Gel Sci. Technol.*, 1-8, **2016**

"Enhancement of TiO_2 NPs Activity by Fe_3O_4 Nano-Seeds for Removal of Organic Pollutants in Water" S. Villa, V. Caratto, F. Locardi, S. Alberti, M. Sturini, A. Speltini, F. Maraschi, F. Canepa and M. Ferretti, *Materials* **2016**, 9, 771

"Functionalization of Fe_3O_4 NPs by Silanization: Use of Amine (APTES) and Thiol (MPTMS) Silanes and Their Physical Characterization" S. Villa, P. Riani, F. Locardi and F. Canepa. *Materials* **2016**, 9, 826

"Photocatalytic Fe-doped n-TiO_2: from synthesis to utilization of in vitro cell models for screening human and environmental nanosafety", T. Balbi, V. Caratto, R. Fabbri, G. Camisassi, S. Villa and M. Ferretti. *Resource-Efficient Technologies 0 0 0,* **2017***, 1–8*

"Delivery Nanoplatforms Based on Sorafenib and Superparamagnetic Iron Oxide Nanoparticles for Magnetically Targeted Therapy of Hepatocellular Carcinoma" N. Depalo, R. M. Iacobazzi, G. Valente, I. Arduino, S. Villa, F. Canepa, V. Laquintana, E. Fanizza, M. Striccoli, A. Cutrignelli, A. Lopedota, P. Porcelli, A. Azzariti, M. Franco, M. L. Curri and N. Denora. *Nano Research* **2017**, 10 (7): 2431–2448

"Thiol functionalized magnetic nanoparticles for static and dynamic removal of Pb (II) ions from waters" S. Villa, P. Riani, F. Soggia, E. Magi and F. Canepa. Submitted to *International Journal of Environmental Science and Technology* (June 2017)

"Systematic study on TiO_2 crystallization via hydrothermal synthesis in the presence of different ferrite nanoparticles as nucleation seeds" S. Alberti, V. Caratto, S. Villa, G. Singh, A. Martinelli, M. Ferretti and F. Canepa. Accepted *Journal of Nanoscience and Nanotechnology* (September 2017)

"Structural effect of copper and nitrogen doping in TiO_2 for photocatalytic activity evaluation" A. Martinelli, S. Alberti, V. Caratto, F. Locardi, G. Pampararo, S. Villa, M. Ferretti. Submitted to *Journal of Solid State Chemistry* (October 2017)

"Enzymatically Promoted Release of Organic Molecules Linked to Magnetic Nanoparticles" C. Lambruschini, S. Villa, L. Banfi, F. Morana, F. Silvetti, P. Riani, R. Riva, A. Relini, F. Canepa. Submitted to *Beilstein Journal of Nanotechnology* (October 2017).

"Ligand-exchange in thiol-functionalized gold nanoparticles investigated through thermogravimetric and evolved gases analyses" F. Locardi, E. Canepa, S. Villa, I. Nelli, M. Ferretti, F. Canepa. Submitted to *Journal of analytical and applied pyrolysis* (November 2017).

Communications at conferences

Oral communications:

- XLIII Congresso Nazionale della Divisione di Chimica Inorganica della Società Chimica Italiana, Camerino 9-12 September 2015, "Capture of heavy metals metals by thiol functionalized magnetic nanoparticles using a system of permanent magnets" Silvia Villa, Paola Riani, Emanuele Magi, Fabio Canepa
- Nanomedicine, Viterbo 21-23 September 2016. "Promising applications of magnetic multifunctional nanoparticles in biomedicine" S. Villa, C. Lambruschini, L. Banfi, P. Riani, F. Canepa, A. Relini, F. Morana, F. Silvetti and R. Riva
- 5th International Conference of Nanoscience and Materials Science. "Biocompatible multifunctional magnetic nanoparticles for possible applications in nanomedicine" S. Villa, L. Banfi, F. Canepa, C. Lambruschini, F. Morana, A. Relini, P. Riani, R. Riva, F. Silvetti. Dubai 16-18 October 2017
- World Congress on Nano Science and Nano Technology. "Biocompatible magnetic nanoparticles for possible applications in nanomedicine" S. Villa, L. Banfi, F. Canepa, C. Lambruschini, F. Morana, A. Relini, P. Riani, R. Riva, F. Silvetti. Dubai 16-17 October 2017

Poster Communications:

- "Structural and magnetic characterization of Co-carbides particles" S. Villa, P. Riani, F. Canepa CALPHAD XLIV, Loano 31 May – 5 June 2015
- "Synthesis and characterization of Co-carbides particles" P. Riani, S. Villa, F. Canepa. XLIII Congresso Nazionale della Divisione di Chimica Inorganica della Società Chimica Italiana, 9-12 September 2015, Camerino
- "Superparamagnetic Iron Oxide Nanocrystal and Sorafenib loaded PEG-terminated Micelles for Targeted Hepatic Carcinoma Therapy" N. Denora, N. Depalo, G. Valente, F. Canepa, S. Villa, V. Laquintana, E. Fanizza, M. Striccoli, M. L. Curri, A. Cutrignelli, A. Lopedota, M. Franco, presented among the project Nanomed, III Meeting, 23-24 April 2015, Bologna
- "Superparamagnetic Nanoparticles and Sorafenib containing phospholipid micelles for targeted hepatic carcinoma therapy" BioMet15, XV Workshop on PharmacoBloMetallics 23-24 October 2015, Bari
- "Magnetic Nanoparticles for biosensors, catalysts and high density permanent magnets" S. Villa, P. Riani, S. Fiorito, F. Canepa. NanotechITALY, Bologna 25-27 November 2015
- "SPIONs/Sorafenib/micelles for magnetic drug delivery" S. Villa, F. Canepa, N. Denora, N. Depalo, School of Nanomedicine, Bari 2-4 December 2015
- "The effect of the precursor on the synthesis and magnetic properties of Co and Co carbides NPs" S. Villa, P. Riani et F. Canepa, 20th International Conference on Solid Compounds of Transition Elements" SCTE-2016, Zaragoza, 11-15 April 2016

- "The effect of the precursor on the synthesis and magnetic properties of Co and Co carbides NPs" S. Villa, P. Riani et F. Canepa, Journées Franco-Italiennes de Chimie, Avignone, 25-26 April 2016
- "Synthesis, characterization and photocatalytic activity of Fe_3O_4–TiO_2 nanopowders" S. Villa, V. Caratto, F. Locardi, F. Canepa et M. Ferretti. Journées Franco-Italiennes de Chimie, Avignone, 25-26 April 2016
- "Multifunctional fluorescent magnetic nanoparticles for potential biomedical applications" S. Villa, C. Lambruschini, R. Riva, L. Banfi, P. Riani, A. Relini and F. Canepa, Journées Franco-Italiennes de Chimie, Avignone, 25-26 April 2016
- "Design and Synthesis of Multifunctional Fluorescent Magnetic Nanoparticles for Promising Biomedical Applications" C. Lambruschini, S. Villa, L. Banfi, F. Canepa, F. Morana, A. Relini, P. Riani, R. Riva and F. Silvetti. XII Congresso del Gruppo Interdivisionale di Chimica Organometallica della Società Chimica Italiana Genova,
  5 - 8 June 2016
- "New synthesis of Fe_3O_4-TiO_2 nanopowders for removal of organic pollutants in water" S. Villa, V. Caratto, F. Locardi, S.Alberti, M. Sturini , A. Speltini, F. Maraschi, F. Canepa et M. Ferretti. XVI CONGRESSO NAZIONALE DI CHIMICA DELL'AMBIENTE E DEI BENI CULTURALI Lecce, 26-29 June 2016
- "Investigation of functionalized nanoparticles through DTA/TGA – GC/MS coupling" F. Locardi, I. Nelli, S. Villa, F. Canepa, V. Caratto, M. Ferretti, G. A. Costa. AICAT 2016 XXXVIII National Congress on Calorimetry, Thermal Analysis and Applied Thermodynamics, Ischia 25-28 September 2016
- "Capture and recovery of heavy metals through functionalized magnetic NPs" S. Villa, P. Riani, E. Magi, F. Canepa. Nano@NTNU Symposium 2016, Trondheim17-18 November 2016
- "Core/shell bi-magnetic nanoparticles: synthesis and magnetic properties" S. Villa, D. Peddis, G. Singh, F. Canepa. 24th International Symposium on Metastable, Amorphous and Nanostructured Materials – ISMANAM 2017, Donostia-San Sebastian, Spain 18-23 June 2017
- "Synthesis and magnetic properties of multi-shell bi-magnetic nanoparticles" S. Villa, D. Peddis, G. Singh, F. Canepa. 5th Italian Conference on Magnetism – Magnet 2017, Assisi, 13-15 September 2017
- "Functionalized nanoparticles investigated through thermal and evolved gas analyses" F. Locardi, I. Nelli, F. Palazon, V. Caratto, S. Villa, G. A. Costa, F. Canepa, M. Ferretti. 13th Mediterranean Conference on Calorimetry and Thermal Analysis - Medicta 2017, Loano, 24-27 September 2017
- "Magnetically Targeted Delivery of Sorafenib to Liver Using Solid Lipid Nanoparticles for treatment of Hepatocellular Carcinoma" N. Depalo, F. Vischio, I. Arduino, S. Villa, F. Canepa, E. Fanizza, B. Chul Lee, V. Laquintana, A. Lopedota, A. Cutrignelli, M. Principia Scavo, M. Striccoli, A. Agostiano, M. L. Curri, N. Denora. Applied Nanotechnology and Nanoscience International Conference – ANNIC 2017, Rome, 18-20 October 2017

J Sol-Gel Sci Technol
DOI 10.1007/s10971-016-4057-5

ORIGINAL PAPER: SOL-GEL AND HYBRID MATERIALS FOR CATALYTIC, PHOTOELECTROCHEMICAL AND SENSOR APPLICATIONS

Different sol–gel preparations of iron-doped TiO_2 nanoparticles: characterization, photocatalytic activity and cytotoxicity

Valentina Caratto[1] · Federico Locardi[2] · Stefano Alberti[2] · Silvia Villa[2] · Elisa Sanguineti[1] · Alberto Martinelli[3] · Teresa Balbi[1] · Laura Canesi[1] · Maurizio Ferretti[2]

Received: 21 January 2016 / Accepted: 26 April 2016

Abstract Fe-doped TiO_2 nanoparticles were prepared by sol–gel method using titanium tetraisopropoxide as the precursor of titania, 2-propanol as solvent, iron(III) chloride as dopant source through calcination at 350 °C. Three different types of samples were synthesized. Samples were characterized by means of X-ray powder diffraction, diffuse reflectance spectroscopy, scanning electron microscopy, Brunauer–Emmett–Teller analysis. All the samples showed the typical structure of anatase plus an amount of brookite ranging from 25 to 35 wt%. The features of the particles, i.e., surface area and aggregation state, were influenced by the reagents ratio: Generally increasing the solvent volume with respect to the titanium precursors induced the formation of nanoparticles with high surface area and low aggregation. Photocatalytic activity of Fe-doped TiO_2 nanopowders was evaluated through methylene blue degradation experiments conducted under simulated solar light irradiation. The cytotoxic potential of the three samples was evaluated in human umbilical vein endothelial cells.

Graphical Abstract

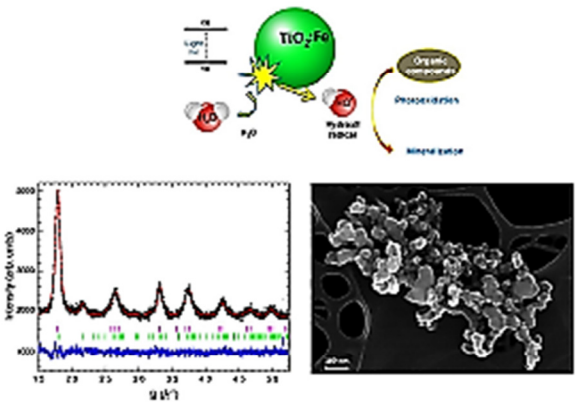

Keywords Iron-doped TiO_2 · Photocatalysis · Sol–gel synthesis · Methylene blue · Nanoparticles · Cytotoxicity

materials

MDPI

Article

Enhancement of TiO_2 NPs Activity by Fe_3O_4 Nano-Seeds for Removal of Organic Pollutants in Water

Silvia Villa [1], Valentina Caratto [1,*], Federico Locardi [1], Stefano Alberti [1], Michela Sturini [2], Andrea Speltini [2], Federica Maraschi [2], Fabio Canepa [1] and Maurizio Ferretti [1]

[1] Department of Chemistry and Industrial Chemistry, University of Genoa, Genoa 16146, Italy; silvia.villa@chimica.unige.it (S.V.); federico.locardi@unige.it (F.L.); stefanofilippo.alberti@gmail.com (S.A.); fabio.canepa@unige.it (F.C.); ferretti@chimica.unige.it (M.F.)

[2] Department of Chemistry, University of Pavia, Pavia 27100, Italy; michela.sturini@unipv.it (M.S.); andrea.speltini@unipv.it (A.S.); federica.maraschi@unipv.it (F.M.)

* Correspondence: caratto@chimica.unige.it

Academic Editor: Andrea P. Reverberi
Received: 28 July 2016; Accepted: 5 September 2016; Published: 10 September 2016

Abstract: The enhancement of the photocatalytic activity of TiO_2 nanoparticles (NPs), synthesized in the presence of a very small amount of magnetite (Fe_3O_4) nanoparticles, is here presented and discussed. From X-ray diffraction (XRD) and differential scanning calorimetry (DSC) analyses, the crystallinity of TiO_2 nanoparticles (NPs) seems to be affected by Fe_3O_4, acting as nano-seeds to improve the tetragonal TiO_2 anatase structure with respect to the amorphous one. Photocatalytic activity data, i.e., the degradation of methylene blue and the Ofloxacin fluoroquinolone emerging pollutant, give evidence that the increased crystalline structure of the NPs, even if correlated to a reduced surface to mass ratio (with respect to commercial TiO_2 NPs), enhances the performance of this type of catalyst. The achievement of a relatively well-defined crystal structure at low temperatures (T_{max} = 150 °C), preventing the sintering of the TiO_2 NPs and, thus, preserving the high density of active sites, seems to be the keystone to understand the obtained results.

Keywords: titania; photocatalysis; methylene blue; Ofloxacin; fluoroquinolone

materials

MDPI

Article

Functionalization of Fe_3O_4 NPs by Silanization: Use of Amine (APTES) and Thiol (MPTMS) Silanes and Their Physical Characterization

Silvia Villa [1], Paola Riani [1,*], Federico Locardi [1] and Fabio Canepa [2]

[1] Dipartimento di Chimica e Chimica Industriale, Università degli Studi di Genova, Via Dodecaneso 31, 16146 Genova, Italy; silvia.villa@chimica.unige.it (S.V.); federico.locardi@unige.it (F.L.)

[2] Dipartimento di Chimica e Chimica Industriale, Università degli Studi di Genova and CNR-SPIN Genova Unit, Via Dodecaneso 31, 16146 Genova, Italy; fabio.canepa@unige.it

* Correspondence: paola.riani@unige.it; Tel.: +39-010-3536174

Academic Editor: Andrea P. Reverberi

Received: 29 July 2016; Accepted: 2 October 2016; Published: 12 October 2016

Abstract: In this paper the results concerning the synthesis of magnetite (Fe_3O_4) nanoparticles (NPs), their functionalization using silane derivatives, such as (3-Aminopropyl)triethoxysilane (APTES) and (3-mercaptopropyl)trimethoxysilane (MPTMS), and their exhaustive morphological and physical characterization by field emission scanning electron microscopy (FE-SEM) with energy dispersion X-ray spectrometer (EDX) analysis, AC magnetic susceptibility, UV-VIS and IR spectroscopy, and thermogravimetric (TGA) analyses are reported. Two different paths were adopted to achieve the desired functionalization: (1) the direct reaction between the functionalized organo-silane molecule and the surface of the magnetite nanoparticle; and (2) the use of an intermediate silica coating. Finally, the occurrence of both the functionalization with amino and thiol groups has been demonstrated by the reaction with ninhydrin and the capture of Au NPs, respectively.

Keywords: magnetite nanoparticles; silica shell; AC magnetic susceptibility; functionalized organo silane molecules

Nano Research
DOI 10.1007/s12274-017-1444-3
Research Article
ISSN 1998-0124
CN 11-5974/O4

Sorafenib delivery nanoplatform based on superparamagnetic iron oxide nanoparticles magnetically targets hepatocellular carcinoma

Nicoletta Depalo[1], Rosa Maria Iacobazzi[2], Gianpiero Valente[3], Ilaria Arduino[4], Silvia Villa[5], Fabio Canepa[5], Valentino Laquintana[4], Elisabetta Fanizza[3], Marinella Striccoli[1], Annalisa Cutrignelli[4], Angela Lopedota[4], Letizia Porcelli[2], Amalia Azzariti[2], Massimo Franco[4], Maria Lucia Curri[1], and Nunzio Denora[4] (✉)

[1] *Istituto per i Processi Chimico-Fisici-CNR UOS Bari, Via Orabona 4, 70125 Bari, Italy*
[2] *Istituto Tumori IRCCS Giovanni Paolo II, viale O. Flacco 65, 70124 Bari, Italy*
[3] *Dipartimento di Chimica, Università degli Studi di Bari Aldo Moro, Via Orabona 4, 70125 Bari, Italy*
[4] *Dipartimento di Farmacia-Scienze del Farmaco, Università degli Studi di Bari Aldo Moro, Via Orabona 4, 70125 Bari, Italy*
[5] *Dipartimento di Chimica e Chimica Industriale, Università di Genova, Via Dodecaneso 31, 16146 Genova, Italy*

Received: 15 September 2016
Revised: 27 December 2016
Accepted: 29 December 2016

KEYWORDS

superparamagnetic iron oxide nanoparticles, PEG-modified phospholipid micelles, drug delivery, magnetic targeting, hepatocellular carcinoma, sorafenib

ABSTRACT

Currently, sorafenib is the only systemic therapy capable of increasing overall survival of hepatocellular carcinoma patients. Unfortunately, its side effects, particularly its overall toxicity, limit the therapeutic response that can be achieved. Superparamagnetic iron oxide nanoparticles (SPIONs) are very attractive for drug delivery because they can be targeted to specific sites in the body through application of a magnetic field, thus improving intratumoral accumulation and reducing adverse effects. Here, nanoformulations based on polyethylene glycol modified phospholipid micelles, loaded with both SPIONs and sorafenib, were successfully prepared and thoroughly investigated by complementary techniques. This nanovector system provided effective drug delivery, had an average hydrodynamic diameter of about 125 nm, had good stability in aqueous medium, and allowed controlled drug loading. Magnetic analysis allowed accurate determination of the amount of SPIONs embedded in each micelle. An *in vitro* system was designed to test whether the SPION micelles can be efficiently held using a magnetic field under typical flow conditions found in the human liver. Human hepatocellular carcinoma (HepG2) cells were selected as an *in vitro* system to evaluate tumor cell targeting efficacy of the superparamagnetic micelles loaded with sorafenib. These experiments demonstrated that this delivery platform is able to enhance sorafenib's antitumor effectiveness by magnetic targeting. The magnetic nanovectors described here represent promising candidates for targeting specific hepatic tumor sites, where selective release of sorafenib can improve its efficacy and safety profile.

Resource-Efficient Technologies 000 (2017) 1–8

Contents lists available at Science Direct

Resource-Efficient Technologies

Journal homepage: www.elsevier.com/locate/reffit

Research paper

Photocatalytic Fe-doped n-TiO_2: From synthesis to utilization of *in vitro* cell models for screening human and environmental nanosafety

Teresa Balbi [a], Valentina Caratto [b], Rita Fabbri [a], Giulia Camisassi [a], Silvia Villa [b], Maurizio Ferretti [b], Laura Canesi [a,*]

[a] Department of Earth, Environmental and Life Sciences-DISTAV, University of Genoa, Corso Europa 26, 16132 Genoa, Italy
[b] Department of Chemistry and Industrial Chemistry-DCCI, University of Genoa, Via Dodecaneso 31, 16146 Genoa, Italy

ARTICLE INFO

Article history:
Received 26 September 2016
Revised 21 March 2017
Accepted 31 March 2017
Available online xxx

Keywords:
Doped n-TiO_2
Human epithelial cells
Mussel hemocytes
Exposure medium
Cytotoxicity

ABSTRACT

The utilization of different types nanomaterials (NMs) in environmental remediation and wastewater treatment requires information on the potential harmful effects on human and environmental health. In this light, the utilization of human cell models together with cells from lower organisms, representative of different environmental compartments, could represent a valuable tool for the *in vitro* screening of the potential toxicity of different NMs used in nanoremediation. Among NMs, n-TiO_2, because of its peculiar optical and chemical properties, is widely applied for photosensitized UV oxidation of organic pollutants. Moreover, development in design of metal- and non metal- doped TiO_2 with extended photocatalytic activity in the visible region represents the subject of ongoing research.

In this work, the cytotoxic effects of three different types of recently synthetized Fe-doped n-TiO_2 were compared in two cell models widely utilized for screening cellular toxicity of NMs in humans and aquatic organisms, human vascular endothelial cells (HECV) and immune cells (hemocytes) of the marine invertebrate, the mussel *Mytilus* spp, respectively. Parallel studies were carried out using N-doped n-TiO_2. The results indicate both distinct and common behavior (agglomeration state) in different media (human cell culture medium and mussel hemolymph serum) and biological effects (cytotoxicity, nitric oxide production) of different types of doped- n-TiO_2 in different cell models. Although *in vitro* studies represent a first step in the toxicological assessment of NMs, studies comparing their effects on human and aquatic invertebrate cells that take into account the effects of different exposure media represent an useful tool for evaluating potential cytotoxicity of those NMs, like TiO_2-based photocatalytic NMs, widely applied in environmental remediation, and whose potential risks are poorly understood.

References

(1) Wolf, E. L.; Medikonda, M. *Understanding the Nanotechnology Revolution*; 2012.

(2) Latorre, M.; Rinaldi, C. Applications of Magnetic Nanoparticles in Medicine: Magnetic Fluid Hyperthermia. *P. R. Health Sci. J.* **2009**, *28*, 227–238.

(3) Poland, C. A.; Duffin, R.; Kinloch, I.; Maynard, A.; Wallace, W. A. H.; Seaton, A.; Stone, V.; Brown, S.; MacNee, W.; Donaldson, K. Carbon Nanotubes Introduced into the Abdominal Cavity of Mice Show Asbestos-like Pathogenicity in a Pilot Study. *Nat. Nanotechnol.* **2008**, *3*, 423–428.

(4) Salata, O. Applications of Nanoparticles in Biology and Medicine. *J. Nanobiotechnology* **2004**, *2*, 3.

(5) Parveen, S.; Misra, R.; Sahoo, S. K. Nanoparticles: A Boon to Drug Delivery, Therapeutics, Diagnostics and Imaging. *Nanomedicine: Nanotechnology, Biology, and Medicine*, 2012, *8*, 147–166.

(6) Wu, W.; Wu, Z.; Yu, T.; Jiang, C.; Kim, W.-S. Recent Progress on Magnetic Iron Oxide Nanoparticles: Synthesis, Surface Functional Strategies and Biomedical Applications. *Sci. Technol. Adv. Mater.* **2015**, *16*, 23501.

(7) Mohammed, L.; Gomaa, H. G.; Ragab, D.; Zhu, J. Magnetic Nanoparticles for Environmental and Biomedical Applications: A Review. *Particuology* **2017**, *30*, 1–14.

(8) Gubin, S. P. *Magnetic Nanoparticles*; 2009.

(9) Issa, B.; Obaidat, I. M.; Albiss, B. A.; Haik, Y. Magnetic Nanoparticles: Surface Effects and Properties Related to Biomedicine Applications. *Int. J. Mol. Sci.* **2013**, *14*, 21266–21305.

(10) Arruebo, M.; Fernández-pacheco, R.; Ibarra, M. R.; Santamaría, J. Magnetic Nanoparticles Controlled Release of Drugs from Nanostructured Functional Materials. *Rev. Lit. Arts Am.* **2007**, *2*, 22–32.

(11) Widder, K. J.; Senyei, A. E.; Scarpelli, D. G. Magnetic Microspheres: A Model System for Site Specific Drug Delivery in Vivo. *Exp. Biol. Med.* **1978**, *158*, 141–146.

(12) Mosbach, K.; Schröder, U. Preparation and Application of Magnetic Polymers for Targeting of Drugs. *FEBS Lett.* **1979**, *102*, 112–116.

(13) Rodzinski, A.; Guduru, R.; Liang, P.; Hadjikhani, A.; Stewart, T.; Stimphil, E.; Runowicz, C.; Cote, R.; Altman, N.; Datar, R.; *et al.* Targeted and Controlled Anticancer Drug Delivery and Release with Magnetoelectric Nanoparticles. *Sci. Rep.* **2016**, *6*, 20867.

(14) Ulbrich, K.; Holá, K.; Šubr, V.; Bakandritsos, A.; Tuček, J.; Zbořil, R. Targeted Drug Delivery with Polymers and Magnetic Nanoparticles: Covalent and Noncovalent Approaches, Release Control, and Clinical Studies. *Chem. Rev.* **2016**, *116*, 5338–5431.

(15) Alexiou, C.; Arnold, W.; Klein, R. J.; Parak, F. G.; Hulin, P.; Bergemann, C.; Erhardt, W.; Wagenpfeil, S.; Lu, A. S. Locoregional Cancer Treatment with Magnetic Drug Targeting Locoregional Cancer Treatment with Magnetic Drug Targeting 1. **2000**, 6641–6648.

(16) Pankhurst, Q. A.; Connolly, J.; Jones, S. K.; Dobson, J. Applications of Magnetic Nanoparticles in Biomedicine. *J. Phys. D. Appl. Phys.* **2003**, *36*.

(17) Yang, H. Y.; Jang, M.-S.; Gao, G. H.; Lee, J. H.; Lee, D. S. pH-Responsive Biodegradable

Polymeric Micelles with Anchors to Interface Magnetic Nanoparticles for MR Imaging in Detection of Cerebral Ischemic Area. *Nanoscale* **2016**, *8*, 12588–12598.

(18) Singh, A.; Sahoo, S. K. Magnetic Nanoparticles: A Novel Platform for Cancer Theranostics. *Drug Discov. Today* **2014**, *19*, 474–481.

(19) Meers, P. Enzyme-Activated Targeting of Liposomes. *Advanced Drug Delivery Reviews*, 2001, *53*, 265–272.

(20) Maier, H. K.; Ulrich, F.; Nestler, D.; Niehoff, H.; Wust, P.; Thiesen, B.; Orawa, H.; Budach, V.; Jordan, A.; Maier-Hauff, K.; *et al.* Efficacy and Safety of Intratumoral Thermotherapy Using Magnetic Iron-Oxide Nanoparticles Combined with External Beam Radiotherapy on Patients with Recurrent Glioblastoma Multiforme. *J. neuro.oncology* **2011**, *103*, 317–324.

(21) Liu, X.; Shan, G.; Yu, J.; Yang, W.; Ren, Z.; Wang, X.; Xie, X.; Chen, X.; Liu, X.; Shan, G.; *et al.* Laser Heating of Metallic Nanoparticles for Photothermal Ablation Applications Laser Heating of Metallic Nanoparticles for Photothermal Ablation Applications. **2017**, *25308*.

(22) Vallejo-Fernandez, G.; Whear, O.; Roca, A. G.; Hussain, S.; Timmis, J.; Patel, V.; O'Grady, K. Mechanisms of Hyperthermia in Magnetic Nanoparticles. *J. Phys. D. Appl. Phys.* **2013**, *46*, 312001.

(23) Abenojar, E. C.; Wickramasinghe, S.; Bas-Concepcion, J.; Samia, A. C. S. Structural Effects on the Magnetic Hyperthermia Properties of Iron Oxide Nanoparticles. *Prog. Nat. Sci. Mater. Int.* **2016**, *26*, 440–448.

(24) GILCHRIST, R. K.; MEDAL, R.; SHOREY, W. D.; HANSELMAN, R. C.; PARROTT, J. C.; TAYLOR, C. B. Selective Inductive Heating of Lymph Nodes. *Ann. Surg.* **1957**, *146*, 596–606.

(25) Thiesen, B.; Jordan, A. Clinical Applications of Magnetic Nanoparticles for Hyperthermia. *Int. J. Hyperthermia* **2008**, *24*, 467–474.

(26) Maier-Hauff, K.; Rothe, R.; Scholz, R.; Gneveckow, U.; Wust, P.; Thiesen, B.; Feussner, A.; Deimling, A.; Waldoefner, N.; Felix, R.; *et al.* Intracranial Thermotherapy Using Magnetic Nanoparticles Combined with External Beam Radiotherapy: Results of a Feasibility Study on Patients with Glioblastoma Multiforme. *J. Neurooncol.* **2007**, *81*, 53–60.

(27) Ali, I. New Generation Adsorbents for Water Treatment. *Chemical Reviews*, 2012, *112*, 5073–5091.

(28) Roto, R.; Yusran, Y.; Kuncaka, A. Magnetic Adsorbent of Fe3O4@SiO2 Core-Shell Nanoparticles Modified with Thiol Group for Chloroauric Ion Adsorption. *Appl. Surf. Sci.* **2016**, *377*, 30–36.

(29) Farmany, A.; Mortazavi, S. S.; Mahdavi, H. Ultrasond-Assisted Synthesis of Fe3O4/SiO2 Core/shell with Enhanced Adsorption Capacity for Diazinon Removal. *J. Magn. Magn. Mater.* **2016**, *416*, 75–80.

(30) Ansari, S.; Bagheripour, E.; Moghadassi, A.; Hosseini, S. M. Fabrication of Mixed Matrix Poly(phenylene Ether-Ether Sulfone)-Based Nanofiltration Membrane Modified by Fe3O4 Nanoparticles for Water Desalination. *J. Polym. Eng.* **2017**, *37*.

(31) AL-Hobaib, A. S.; AL-Sheetan, K. M.; El Mir, L. Effect of Iron Oxide Nanoparticles on the Performance of Polyamide Membrane for Ground Water Purification. *Mater. Sci. Semicond. Process.* **2015**, *42*, MSSPD1500774.

(32) Gómez-Pastora, J.; Bringas, E.; Ortiz, I. Recent Progress and Future Challenges on the Use

of High Performance Magnetic Nano-Adsorbents in Environmental Applications. *Chemical Engineering Journal*, 2014, *256*, 187–204.

(33) Ahmed, M. A.; Ali, S. M.; El-Dek, S. I.; Galal, A. Magnetite–hematite Nanoparticles Prepared by Green Methods for Heavy Metal Ions Removal from Water. *Mater. Sci. Eng. B* **2013**, *178*, 744–751.

(34) Yong-Mei, H.; Man, C.; Zhong-Bo, H. Effective Removal of Cu (II) Ions from Aqueous Solution by Amino-Functionalized Magnetic Nanoparticles. *J. Hazard. Mater.* **2010**, *184*, 392–399.

(35) Kyzas, G. Z.; Deliyanni, E. A. Mercury(II) Removal with Modified Magnetic Chitosan Adsorbents. *Molecules* **2013**, *18*, 6193–6214.

(36) Badruddoza, A. Z. M.; Shawon, Z. B. Z.; Rahman, M. T.; Hao, K. W.; Hidajat, K.; Uddin, M. S. Ionically Modified Magnetic Nanomaterials for Arsenic and Chromium Removal from Water. *Chem. Eng. J.* **2013**, *225*, 607–615.

(37) Gunatilake, S. K. Methods of Removing Heavy Metals from Industrial Wastewater. *J. Multidiscip. Eng. Sci. Stud.* **2015**, *1*, 12–18.

(38) Dizge, N.; Keskinler, B.; Barlas, H. Sorption of Ni(II) Ions from Aqueous Solution by Lewatit Cation-Exchange Resin. *J. Hazard. Mater.* **2009**, *167*, 915–926.

(39) Streams, A. W. Hollow Fiber Solvent Extraction Removal of Toxic Heavy Metals from. *Analysis* **1993**, 1186–1195.

(40) Mollah, M. Y.; Schennach, R.; Parga, J. R.; Cocke, D. L. Electrocoagulation (EC)--Science and Applications. *J. Hazard. Mater.* **2001**, *84*, 29–41.

(41) Petrov, S.; Nenov, V. Removal and Recovery of Copper from Wastewater by a Complexation-Ultrafiltration Process. *Desalination* **2004**, *162*, 201–209.

(42) Kurniawan, T. A.; Chan, G. Y. S.; Lo, W. H.; Babel, S. Physico-Chemical Treatment Techniques for Wastewater Laden with Heavy Metals. *Chem. Eng. J.* **2006**, *118*, 83–98.

(43) Rajasulochana, P.; Preethy, V. Comparison on Efficiency of Various Techniques in Treatment of Waste and Sewage Water – A Comprehensive Review. *Resour. Technol.* **2016**, *2*, 175–184.

(44) Saif, S.; Tahir, A.; Chen, Y. Green Synthesis of Iron Nanoparticles and Their Environmental Applications and Implications. *Nanomaterials* **2016**, *6*, 209.

(45) Chowdhury, S. R.; Yanful, E. K. Arsenic and Chromium Removal by Mixed Magnetite-Maghemite Nanoparticles and the Effect of Phosphate on Removal. *J. Environ. Manage.* **2010**, *91*, 2238–2247.

(46) Lin, S.; Lu, D.; Liu, Z. Removal of Arsenic Contaminants with Magnetic ??-Fe2O3 Nanoparticles. *Chem. Eng. J.* **2012**, *211–212*, 46–52.

(47) Shen, Y. F.; Tang, J.; Nie, Z. H.; Wang, Y. D.; Ren, Y.; Zuo, L. Preparation and Application of Magnetic Fe3O4 Nanoparticles for Wastewater Purification. *Sep. Purif. Technol.* **2009**, *68*, 312–319.

(48) Nassar, N. N. Rapid Removal and Recovery of Pb(II) from Wastewater by Magnetic Nanoadsorbents. *J. Hazard. Mater.* **2010**, *184*, 538–546.

(49) Tang, Y.; Liang, S.; Wang, J.; Yu, S.; Wang, Y. Amino-Functionalized Core-Shell Magnetic

Mesoporous Composite Microspheres for Pb(II) and Cd(II) Removal. *J. Environ. Sci. (China)* **2013**, *25*, 830–837.

(50) Zhang, J.; Zhai, S.; Li, S.; Xiao, Z.; Song, Y.; An, Q.; Tian, G. Pb(II) Removal of Fe3O4@SiO2-NH2 Core-Shell Nanomaterials Prepared via a Controllable Sol-Gel Process. *Chem. Eng. J.* **2013**, *215–216*, 461–471.

(51) Chung, J.; Chun, J.; Lee, J.; Lee, S. H.; Lee, Y. J.; Hong, S. W. Sorption of Pb(II) and Cu(II) onto Multi-Amine Grafted Mesoporous Silica Embedded with Nano-Magnetite: Effects of Steric Factors. *J. Hazard. Mater.* **2012**, *239–240*, 183–191.

(52) Song, B. Y.; Eom, Y.; Lee, T. G. Removal and Recovery of Mercury from Aqueous Solution Using Magnetic Silica Nanocomposites. *Appl. Surf. Sci.* **2011**, *257*, 4754–4759.

(53) Hakami, O.; Zhang, Y.; Banks, C. J. Thiol-Functionalised Mesoporous Silica-Coated Magnetite Nanoparticles for High Efficiency Removal and Recovery of Hg from Water. *Water Res.* **2012**, *46*, 3913–3922.

(54) Safarik, I.; Horska, K.; Pospiskova, K.; Safarikova, M. Magnetic Techniques for the Detection and Determination of Xenobiotics and Cells in Water. *Anal. Bioanal. Chem.* **2012**, *404*, 1257–1273.

(55) Nanocrystals, M. F. O.; Yavuz, C. T.; Mayo, J. T.; Yu, W. W.; Prakash, A.; Falkner, J. C.; Yean, S.; Cong, L.; Shipley, H. J.; Kan, A.; *et al.* Low-Field Magnetic Separation of. *Science (80-.).* **2006**, *314*, 964–967.

(56) Pamme, N. Magnetism and Microfluidics. *Lab Chip* **2006**, *6*, 24–38.

(57) Mohan, D.; Pittman, C. U. Arsenic Removal from Water/wastewater Using Adsorbents-A Critical Review. *J. Hazard. Mater.* **2007**, *142*, 1–53.

(58) Zhang, Y. R.; Wang, S. Q.; Shen, S. L.; Zhao, B. X. A Novel Water Treatment Magnetic Nanomaterial for Removal of Anionic and Cationic Dyes under Severe Condition. *Chem. Eng. J.* **2013**, *233*, 258–264.

(59) Baruah, S.; Jaisai, M.; Dutta, J. Development of a Visible Light Active Photocatalytic Portable Water Purification Unit Using ZnO Nanorods. *Catal. Sci. Technol.* **2012**, *2*, 918.

(60) Mahlambi, M. M.; Ngila, C. J.; Mamba, B. B. Recent Developments in Environmental Photocatalytic Degradation of Organic Pollutants: The Case of Titanium Dioxide Nanoparticles-A Review. *J. Nanomater.* **2015**, *2015*.

(61) Makhal, A.; Sarkar, S.; Bora, T.; Baruah, S.; Dutta, J.; Raychaudhuri, a K.; Pal, S. K. Dynamics of Light Harvesting in ZnO Nanoparticles. *Nanotechnology* **2010**, *21*, 265703.

(62) Elsalamony, R. A.; Mahmoud, S. A. Preparation of Nanostructured Ruthenium Doped Titania for the Photocatalytic Degradation of 2-Chlorophenol under Visible Light. *Arab. J. Chem.* **2017**, *10*, 194–205.

(63) Gaya, U. I.; Abdullah, A. H. Heterogeneous Photocatalytic Degradation of Organic Contaminants over Titanium Dioxide: A Review of Fundamentals, Progress and Problems. *J. Photochem. Photobiol. C Photochem. Rev.* **2008**, *9*, 1–12.

(64) Ren, Y.; Hardwick, L. J.; Bruce, P. G. Lithium Intercalation into Mesoporous Anatase with an Ordered 3D Pore Structure. *Angew. Chemie - Int. Ed.* **2010**, *49*, 2570–2574.

(65) Friedler, E.; Gilboa, Y. Performance of UV Disinfection and the Microbial Quality of Greywater Effluent along a Reuse System for Toilet Flushing. *Sci. Total Environ.* **2010**, *408*,

2109–2117.

(66) Hoffmann, M. R.; Martin, S. T.; Choi, W.; Bahnemann, D. W. Environmental Applications of Semiconductor Photocatalysis. *Chem. Rev.* **1995**, *95*, 69–96.

(67) Cayre, O. J.; Chagneux, N.; Biggs, S. Stimulus Responsive Core-Shell Nanoparticles: Synthesis and Applications of Polymer Based Aqueous Systems. *Soft Matter* **2011**, *7*, 2211–2234.

(68) Chatterjee, K.; Sarkar, S.; Jagajjanani Rao, K.; Paria, S. Core/shell Nanoparticles in Biomedical Applications. *Adv Colloid Interface Sci* **2014**, *209*, 8–39.

(69) Nogués, J.; Sort, J.; Langlais, V.; Skumryev, V.; Suriñach, S.; Muñoz, J. S.; Baró, M. D. Exchange Bias in Nanostructures. *Physics Reports*, 2005, *422*, 65–117.

(70) Lopez-Ortega, A.; Tobia, D.; Winkler, E.; Golosovsky, I. V.; Salazar-Alvarez, G.; Estrade, S.; Estrader, M.; Sort, J.; González, M. A.; Suriñach, S.; *et al.* Size-Dependent Passivation Shell and Magnetic Properties in Antiferromagnetic/ferrimagnetic Core/shell MnO Nanoparticles. *J. Am. Chem. Soc.* **2010**, *132*, 9398–9407.

(71) Kiwi, M. Exchange Bias Theory. *J. Magn. Magn. Mater.* **2001**, *234*, 584–595.

(72) Nogués, J.; Schuller, I. K. Exchange Bias. **1999**, *192*.

(73) Meiklejohn, W. H.; Bean, C. P. New Magnetic Anisotropy. *Phys. Rev.* **1956**, *102*, 1413–1414.

(74) Lima, E.; Winkler, E. L.; Tobia, D.; Troiani, H. E.; Zysler, R. D.; Agostinelli, E.; Fiorani, D. Bimagnetic CoO core/CoFe 2O 4 Shell Nanoparticles: Synthesis and Magnetic Properties. *Chem. Mater.* **2012**, *24*, 512–516.

(75) Winkler, E. L.; Lima, E.; Tobia, D.; Saleta, M. E.; Troiani, H. E.; Agostinelli, E.; Fiorani, D.; Zysler, R. D. Origin of Magnetic Anisotropy in ZnO/CoFe2O4 and CoO/CoFe2O4 Core/shell Nanoparticle Systems. *Appl. Phys. Lett.* **2012**, *101*.

(76) Liu, W.; Zhong, W.; Du, Y. W. Magnetic Nanoparticles with Core/Shell Structures. *J Nanosci Nanotechnol* **2008**, *8*, 2781–2792.

(77) Soares, J. M.; Galdino, V. B.; Machado, F. L. A. Exchange-Bias and Exchange-Spring Coupling in Magnetic Core-Shell Nanoparticles. *J. Magn. Magn. Mater.* **2014**, *350*, 69–72.

(78) Moon, S. H.; Noh, S. H.; Lee, J. H.; Shin, T. H.; Lim, Y.; Cheon, J. Ultrathin Interface Regime of Core-Shell Magnetic Nanoparticles for Effective Magnetism Tailoring. *Nano Lett.* **2017**, *17*, 800–804.

(79) Ma, Z.; Shao, G.; Fan, Y.; Wang, G.; Song, J.; Shen, D. Construction of Hierarchical α-MnO2 Nanowires@Ultrathin δ-MnO2 Nanosheets Core-Shell Nanostructure with Excellent Cycling Stability for High-Power Asymmetric Supercapacitor Electrodes. *ACS Appl. Mater. Interfaces* **2016**, *8*, 9050–9058.

(80) López-Ortega, A.; Estrader, M.; Salazar-Alvarez, G.; Roca, A. G.; Nogués, J. Applications of Exchange Coupled Bi-Magnetic Hard / Soft and Soft / Hard Magnetic Core / Shell Nanoparticles. *Phys. Rep.* **2014**, 1–44.

(81) Colombo, M.; Carregal-Romero, S.; Casula, M. F.; Gutiérrez, L.; Morales, M. P.; Bohm, I. B.; Heverhagen, J. T.; Prosperi, D.; Parak, W. J. Biological Applications of Magnetic Nanoparticles. *Chem. Soc. Rev.* **2012**, *41*, 4306–4334.

(82) Yoo, D.; Lee, J. H.; Shin, T. H.; Cheon, J. Theranostic Magnetic Nanoparticles. *Acc. Chem. Res.* **2011**, *44*, 863–874.

(83) Noh, S. H.; Na, W.; Jang, J. T.; Lee, J. H.; Lee, E. J.; Moon, S. H.; Lim, Y.; Shin, J. S.; Cheon, J. Nanoscale Magnetism Control via Surface and Exchange Anisotropy for Optimized Ferrimagnetic Hysteresis. *Nano Lett.* **2012**, *12*, 3716–3721.

(84) Lee, J.-H.; Jang, J.; Choi, J.; Moon, S. H.; Noh, S.; Kim, J.; Kim, J.-G.; Kim, I.-S.; Park, K. I.; Cheon, J. Exchange-Coupled Magnetic Nanoparticles for Efficient Heat Induction. *Nat. Nanotechnol.* **2011**, *6*, 418–422.

(85) Carl, P. L.; Chakravarty, P. K.; Katzenellenbogen, J. A.; Weber, M. J. Protease-Activated "Prodrugs" for Cancer Chemotherapy. *Proc. Natl. Acad. Sci. U. S. A.* **1980**, *77*, 2224–2228.

(86) Yang, Y.; Aw, J.; Chen, K.; Liu, F.; Padmanabhan, P.; Hou, Y.; Cheng, Z.; Xing, B. Enzyme-Responsive Multifunctional Magnetic Nanoparticles for Tumor Intracellular Drug Delivery and Imaging. *Chem. - An Asian J.* **2011**, *6*, 1381–1389.

(87) Banfi, L.; Basso, A.; Bevilacqua, E.; Gandolfo, V.; Giannini, G.; Guanti, G.; Musso, L.; Paravidino, M.; Riva, R. Synthesis and DNA-Cleaving Activity of Lactenediynes Conjugated with DNA-Complexing Moieties. *Bioorganic Med. Chem.* **2008**, *16*, 3501–3518.

(88) Reaction, S. Schotten-Baumann Reaction. **1886**, 2536–2539.

(89) Massart, R. Preparation of Aqueous Magnetic Liquids in Alkaline and Acidic Media. *IEEE Trans. Magn.* **1981**, *17*, 1247–1248.

(90) Ware, R. By the Following Function of the Optical Densities : Values of kF Calculated from ~ F / TF Are Listed in O-O Transition . This Is Denoted as kFff , I . E .,. **1980**, *51*, 61–68.

(91) Apolipoprotein, E.; Bains, G. K.; Kim, S. H.; Sorin, E. J.; Narayanaswami, V. NIH Public Access. **2013**, *51*, 6207–6219.

(92) Shouheng Sun, Hao Zeng, David B. Robinson, Simone Raoux, Philip M. Rice, Shan X. Wang, and G. L. Controlled Synthesis of MFe 2 O 4 (M = Mn , Fe , Co , Ni and Zn) Nanoparticles. *J.Am.Chem.Soc.* **2004**, *126*, 273–279.

(93) Shenker, H. Magnetic Anisotropy of Cobalt Ferrite (<math Display="inline"> <mrow> <msub> <mrow> <mi mathvariant="normal">Co</mi> </mrow> <mrow> <mn>1.01</mn> </mrow> </msub> </mrow> </math> <math Display="inline"> <mrow> <msub> <mrow> <mi mathvariant="normal">Fe</mi. *Phys. Rev.* **1957**, *107*, 1246–1249.

(94) Golubenko, Z. V.; Kamzin, a. S.; Ol'khovik, L. P.; Khvorov, M. M.; Sizova, Z. I.; Shabatin, V. P. Stoner-Wohlfarth-Type Behavior of a Close-Packed Array of High-Anisotropy Hexaferrite Nanoparticles. *Phys. Solid State* **2002**, *44*, 1698–1702.

(95) Oveisi, F.; Nikazar, M.; Razzaghi, M. H.; Mirrahimi, M. A.-S.; Jafarzadeh, M. T. Effective Removal of Mercury from Aqueous Solution Using Thiol-Functionalized Magnetic Nanoparticles. *Environ. Nanotechnology, Monit. Manag.* **2017**, *7*, 130–138.

(96) Parham, H.; Zargar, B.; Shiralipour, R. Fast and Efficient Removal of Mercury from Water Samples Using Magnetic Iron Oxide Nanoparticles Modified with 2-Mercaptobenzothiazole. *J. Hazard. Mater.* **2012**, *205–206*, 94–100.

(97) Van Doorslaer, X.; Dewulf, J.; Van Langenhove, H.; Demeestere, K. Fluoroquinolone Antibiotics: An Emerging Class of Environmental Micropollutants. *Sci. Total Environ.* **2014**, *500–501*, 250–269.

(98) Caratto, V.; Aliakbarian, B.; Casazza, A. A.; Setti, L.; Bernini, C.; Perego, P.; Ferretti, M. Inactivation of Escherichia Coli on Anatase and Rutile Nanoparticles Using UV and Fluorescent Light. *Mater. Res. Bull.* **2013**, *48*, 2095–2101.

(99) Villa, S.; Caratto, V.; Locardi, F.; Alberti, S.; Sturini, M.; Speltini, A.; Maraschi, F.; Canepa, F.; Ferretti, M. Enhancement of TiO2 NPs Activity by Fe3O4 Nano-Seeds for Removal of Organic Pollutants in Water. *Materials (Basel).* **2016**, *9*, 771.

(100) Su, C.; Hong, B.-Y.; Tseng, C.-M. Sol–gel Preparation and Photocatalysis of Titanium Dioxide. *Catal. Today* **2004**, *96*, 119–126.